Michael Dohr, BSc

# Temperature induced effects of dioctyl-benzothieno-benzothiophene thin films

## MASTER THESIS

For obtaining the academic degree
Diplom-Ingenieur

Master Programme of
Technical Physics

**Graz University of Technology**

Supervisor:

Ao.Univ.-Prof. Dipl.-Ing. Dr.techn. Roland Resel
Institute of Solid State Physics
Graz University of Technologies

Graz, March, 2012

# EIDESSTATTLICHE ERKLÄRUNG

Ich erkläre an Eides statt, dass ich die vorliegende Arbeit selbstständig verfasst, andere als die angegebenen Quellen/Hilfsmittel nicht benutzt, und die den benutzten Quellen wörtlich und inhaltlich entnommene Stellen als solche kenntlich gemacht habe.

Graz, am ……………………………                    …………………………………………………..
                                                                                (Unterschrift)

# STATUTORY DECLARATION

I declare that I have authored this thesis independently, that I have not used other than the declared sources / resources, and that I have explicitly marked all material which has been quoted either literally or by content from the used sources.

……………………………                    …………………………………………………..
        date                                                            (signature)

# Acknowledgment

First of all I would like to thank my supervisor Roland Resel for providing the possibility to accomplish my master thesis in his group. Special thanks for making it possible to perform experiments at the synchrotron in Hamburg and to spend time at the Universite Libre de Bruxelles (ULB) in Brussels, Belgium. It was a pleasure to give a talk at the meeting on surface induced crystallographic structures on 18th of April 2012 there.

Furthermore, I'd like to thank Oliver Werzer for introducing me into the interesting field of organic molecules by guiding me through the whole process from film fabrication to the experiments and data analysis. He always took his time to discuss theoretical details and experimental results during the first few months of my work.

Of course I like to thank the people from our group Markus Neuschitzer, Tatjana Djuric, Alexander Pichler and Christoph Lercher for helpful discussions. Special thanks to Armin Moser for his professional input regarding data analysis of reciprocal spacemaps and his support during the beamtime at the HASYLAB beamline W1. Big thanks to Alfred Neuhold who introduced me into the art of x-ray reflectivity fitting. Also, I'd like to thank Ingo Salzmann for his support at HASYLAB and for his comments on the results.

Additionally, I would like to thank Prof. M. Sferrazza, Prof. Yves Geerts and his group at the ULB for synthesizing the material and giving me the chance to perform temperature dependent optical microscopy. Special thanks to Jean-Baptiste Arlin for teaching me how to live in Brussels, introducing me to their laboratory as well as technical support. With respect to atomic force microscopy, I'd like to thank Prof. Christian Teichert and Quan Shen from the Montan University in Leoben.

Last but not least my final thanks go to Manuela Theuermann, who supported and encouraged me through the last years of my studies at the Graz University of Technology and to my parents for their support in every moment of my life.

# Abstract

With respect to the ongoing challenge in finding suitable materials in the field of organic electronics, a lot of attention has been paid on dialkyl-benzothieno-benzothiophenes ($C_n$-BTBT's) recently. Next to the extraordinary high organic field effect transistor mobility of more than $1\frac{cm^2}{Vs}$, it shows good processability for film fabrication by solution processing and seems to be stable at ambient atmosphere. Thus, BTBT-derivates have become one of the most promising candidates as an active layer material in organic devices. It is well known, that structural perfectness in terms of layer homogeneity and molecular packing are the key elements for device performance. Several groups investigated the availability of liquid crystalline materials for solution processing. It was found that by exploiting the smectic phase for film fabrication, enhanced device performances up to $3\frac{cm^2}{Vs}$ could be achieved.

According to those results, the primary goal of this study is to investigate the structural properties of dioctyl-benzothieno-benzothiophene thin films as a function of temperature in terms of crystallographic properties and morphology. Films have been prepared by spin coating from tetrahydrofuran solutions on thermally oxidised silicon oxide wafers. By variation of the concentration of the solutions, different thicknesses starting from a monolayer up to 100 nm thick films have been produced. Investigation of the temperature-behaviour was done by partially resolved microscopic methods (atomic force and optical microscopy) as well as integral characterisation methods (grazing incidence x-ray scattering and x-ray reflectivity).

Uniform crystallisation of the thin films in the known single crystal structure is found. The crystallites are formed by up-right standing molecules which transfer into a smectic A phase at a certain, thickness-dependent transition temperature. Both, ultra thin films (monolayer) as well as multilayer films show pronounced dewetting during heating by the formation of huge crystalline islands with a lateral size in the $\mu m$ range. Close to the liquid crystalline state, a defined monolayer is formed besides crystalline domains. In the liquid crystalline state the thickness of this layer increases as a function of temperature. Quantized layer thickness in steps of monolayer thickness are observed, a phenomenon known as smectic layering. At 105°C a monolayer (thickness 2.9 nm), at 108°C a bilayer and at 115°C a triple layer is developed. It was found that all structures could be stabilized by rapid cooling down to room temperature.

# Kurzfassung

Im technologisch bedeutungsvollen Bereich der organischen Elektronik beseteht seit Kurzem reges Interesse an Dialkyl-benzothieno-benzothiophen ($C_n$-BTBT) Derivaten. Neben den außerordentlich hohen erreichbaren Device-Charakteristiken, welche BTBT für den Einsatz in organischen Feldeffekt-Transistoren qualifizieren, zeichnet sich BTBT unter anderem durch hohe Stabilität aus. Ein weiterer großer Vorteil liegt in der alkylkettenbedingten Löslichkeit, welche Filmherstellung auf Basis lösungsbasierter Prozeduren erlaubt. Aufgrund dieser Eigenschaften scheint dieses Molekül einer der aussichtsreichsten Kandidaten für den Einsatz als aktive Schicht in organischen Bauelementen zu sein. Durch Ausnützen der flüssigkristallinen Phase konnte die erreichbare Mobilität der hergestellten Feldeffekttransistoren um einen Faktor drei erhöht werden. Dies ist grundlegend auf die strukturelle Perfektion sowie Homogenität in den hergestellten Schichten zurückzuführen.

Auf Basis dieser Ergebnisse beschäftigt sich diese Arbeit damit, die strukturellen Eigenschaften des Systems mit Bezug auf Kristallografie sowie Morphologie als Funktion der Temperatur zu klären. C8-BTBT-Dünnschichten wurden durch Spin-Coating von Tetrahydrofuran-Lösungen auf thermisch oxidierten Siliziumoxid-Wafern hergestellt. Durch Variation der Lösungskonzentration wurden Schichtdicken von 3 nm (Monolayer) bis hin zu 100 nm verwirklicht. Die temperaturabhängigen Untersuchungen wurden mit Mitteln der optischen- und Rasterkraft-Mikroskopie, sowie den integralen röntgendiffraktionsbasierten Charakterisierungmethoden *grazing incidence diffraction* und *x-ray-reflectivity* durchgeführt.

Die Ergebnisse werden nach Schichtdicke separiert präsentiert. Die Packungsstruktur sämtlicher fabrizierten Dünnschichten ist jener der zugehörigen Einkristalllösung ident. Sie besteht aus aufrechtstehenden Molekülen in Herringbone-Anordnung, welche sich bei einer schichtdickenabhängigen Übergangstemperatur auflöst und in eine flüssigkristalline smektische A Phase übergeht. Sowohl der Monolayer als auch die 100 nm dicke Schicht zeigen ausgeprägtes Entnetzungsverhalten im Temperaturbereich von Raumtemperatur bis hin zur Phasenübergangstemperatur, welches zur Formation von bis zu einigen $\mu m$ großen Kristalliten führt. In der Nähe des Phasenübergangs kommt es zur Ausbildung einer gleichmäßigen Schicht auf der Oberfläche. Für den 100 nm Film erfolgt ein quantisiertes Schichtwachstum, welches im Bereich von 105°C zur Ausbildung eines Monolayers, bei 108°C eines 2-Schichtsystems sowie bei 115°C zur Erstellung eines definierten 3-Schichtsystems auf der Oberfläche führt. Diese im flüssigkristallinen Zustand erstellten Schichten können durch rasches Abkühlen eingefroren und zu einer bei Raumtemperatur stabilen Struktur überführt werden.

# Contents

# 1. General Introduction

In this chapter we will give a brief introduction into some fundamental basics that are mandatory in order to understand the physics behind dioctyl-bentzothieno-benzothiophene (C8-BTBT). Starting with some general information about small molecules and liquid crystallinity, a detailed description of C8-BTBT, its properties and packing structure will be given before getting to the temperature induced effects observed in chapter 5 and 6.

## 1.1. Small molecules

Since the end of the last century, the field of electronic devices has made the step away from amorphous, rigid and expensive silicon based thin film transistors (TFT's) to flexible, cheap, easy-to-produce and more energy efficient devices based on organic materials.

The ability to change electronic as well as structural properties of the molecules by the means of chemical substitution has become the key advantage of organic compounds compared with their inorganic precursors. When it comes to find suitable materials, it is all about their possible application as an active layer organic field-effect transistors (OFETs), organic light-emitting diodes (OLEDs) or organic photovoltaic cells (OPVCs). Hereby, the most important factors are field-effect-transistor characteristics i.e. device performance, cost-effective fabrication and stability in ambient atmosphere. For a long time, this area of suitable organic materials was dominated by extensively studied and thus well known conjugated polymers like Poly(3-hexylthiophen-2,5-diyl)-P3HT used for organic solar cells (Huynh, 2002), (Erb et al., 2005). Giving another example, we should note Poly[(9,9-dioctylfluorenyl-2,7-diyl)-co-bithiophene]-F8T2. Next to high device performance, the flexibility of those systems enabled direct printing of functional electronic materials for low-cost fabrication of integrated circuits (Sirringhaus, 2000). Right now, a lot of attention is paid on the development of flexible organic light emitting diodes (OLEDs) (Gustafsson et al., 1992).

In order to continue further improvement of device characteristics, like the mobility $\mu_{FET}$, polymers tend to get to their limit due to the statistical distribution of molecular size as well as structural defects acting as charge carrier traps within the semiconducting channel (Ebata et al., 2007). In this regard, molecular materials are advantageous in terms of their well-defined structure, ease of purification and controllable properties.

Thus, although polymer do have advantages like their film forming ability, the focus has now changed into the direction of small molecules. Over the years, a shed-load of organic compounds has been synthesized. It turns out, that only a few of them are able to accomplish all: To generate $\mu_{FET}$ values comparable to those of polymers or inorganic devices, to be stable in ambient conditions and to exhibit film forming properties.

Before getting to C8-BTBT, which will be introduced in detail in sec. 1.3, we will now focus on some selected and popular organic molecules:
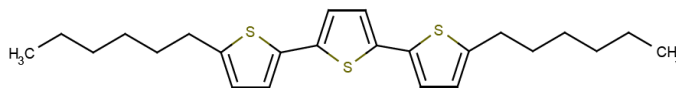
**Pentacene**
The most heavily investigated and prominent example for organic molecules in the field of electronic devices is pentacene. Because of the high reproducibility of thin films by the means of vacuum deposition and very high charge carrier mobilities of holes (comparable to amorphous silicon) it has become a benchmark material in the field of electronic devices. As can be seen in fig. 1.1(a), it simply consists of five conjugated phenyl-rings. As most organic molecules, pentacene shows polymorphism in the presence of a surface or interface (Mattheus et al., 2001). As an effect, the crystalline phase of the thin film can vary and due to the fact, that the molecular packing is a main parameter for device performance, understanding the parameters leading to the different phases was some kind of the main topics studied over the last years and is still of great interest.A detailed analysis of the structural and energetic properties can be found in Salzmann (2008).

**Dihexyl-terthiophene (DH3T)**
DH3T shows a broad variety of both, temperature dependent liquid crystalline phases as well as polymorphism in the presence of an interface or surface (Wedl et al., 2012). Thus, it suits perfectly to investigate the influence of the liquid crystalline phases on thin film phase. The chemical structure can be seen in fig. 1.1(b). It consists of two di-hexyl side chains pointing into the direction of the molecular long axis and three tiophene-rings in the core. These rings are bridged by carbon single bonds which introduces a lot of rotational freedom and therefore explains the appearance of numerous different phases.
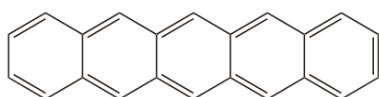


(a) Pentacene ($C_{22}H_{14}$)        (b) DH3T ($C_{24}H_{32}S_3$)

**Figure 1.1.:** Chemical structure of a) pentacene and b) dihexyl-terthiophene (DH3T)
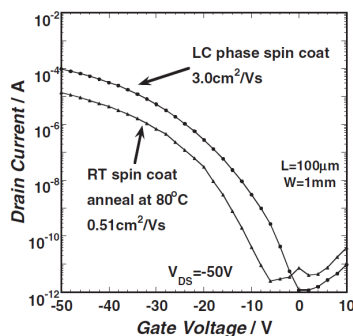
## 1.2. Liquid Crystals

Liquid crystals (LC) or liquid crystalline materials have made their way from a scientific oddity to great scientific and, mainly because of their utilization in LC displays, technological importance. Recently, a lot of attention has been paid on the application of liquid crystals in organic electronics. This is due to the huge variety of structural and physical properties (Demus, 1999) that can be exploited to produce very defined layers of certain materials. In addition, liquid crystalline materials often show high solubility which in return allows solution based processing.

Giving some examples:

- Their self-organizing behaviour is e.g. used to produce self-organized thin films for high-efficiency organic photovoltaics out of discotic LC's (Schmidt-Mende, 2001).

- Iino and Hanna (2006) have shown the availability of liquid crystallinity in solution processing for polycrystalline thin films.

- Finally, Ebata et al. (2007) investigated the influence of the liquid crystalline phase on the device performance of BTBT in OFET's

For organic electronics, the increased mobility of the molecules on the surface in the LC phase is usually used to produce homogeneous, uniform and stressless films (Lengyel et al., 2006). As already mentioned in the abstract, this is especially true for C8-BTBT, where it has been proved, that fabrication in the smectic A (SmA) phase is capable to push up device performance by a factor of three (see fig. 1.2). Therefore, this chapter contains some fundamental information and theoretical background of liquid crystallinity with respect to the smectic phase of BTBT - derivates.

| Condition of film fabrication | Mobility [$cm^2$ $V^{-1}$ $s^{-1}$] | Reference |
|---|---|---|
| Spin-coated at room temperature and additional thermal anneal at 80 ºC | 0.28–0.98 0.28–0.86 | This work; Ref. [8] |
| Spin-coated in liquid crystal phase | 1.0–3.0 | This work |
| Vacuum deposition on treated $SiO_2$ | 0.85–2.7 | Ref. [16] |

(a) Transfer characteristics of $C_{10}$-BTBT FETs

(b) FET mobilities of $C_{10}$-BTBT films

**Figure 1.2.:** Comparison of $C_{10}$-BTBT thin films fabricated under various conditions with respect to a) transfer characteristics and b) OFET mobility according to Iino and Hanna (2006)

## 1.2.1. Characterisation

Liquid crystals describe a state of matter at the interface between the highly, three dimensionally ordered crystalline state and isotropic liquid. Since discovered in 1888, a huge variety of different liquid crystalline states, called mesophases, has been found. Thus, characterisation of LC's has become a science for itself.

Based on the origin of the occurrence of those mesophases, LC's are divided into two groups:

1. **Thermotropic LC's**: The degree of ordering depends on the temperature. In general, there is a broad variety of possible subphases between the isotropic and the crystalline state of the LC (see fig. 1.3).

2. **Lyotropic LC's**: Additional ordering is induced into the isotropic phase by addition of a solvent. The level of orientational and positional order usually depends on the ratio of concentrations.

As thermotropics are the most common type of LC's and C8-BTBT indeed is a calamatic thermotropic material, we will focus on the characterization and nomenclature of this type according to the International Union of Pure and Applied Chemistry (IUPAC,(Baron and Stepto, 2002)) only. A detailed description about lyotropic LC's can e.g. be found in Dietrich (1998).

As stated above, there is a broad range of possible subphases dependent on the level of orientational and positional order. A schematic drawing is given in fig. 1.3, where the possible subphases of calamatic LC's are listed according to their degree of ordering.
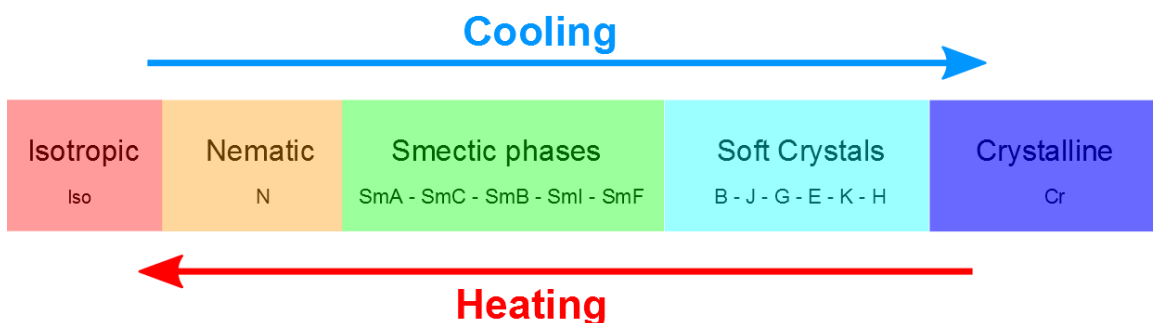


**Figure 1.3.:** Overview of possible mesophases of calamatic thermotropic liquid crystals including their nomenclature according to Baron and Stepto (2002).

Of course, no single molecule exhibits all of those phases but in common, they are following this sequence. To give an example, C8-BTBT follows an Iso-SmA-Cr sequence on cooling and vice versa. Next to this, it must be noted that further phases like chiral smectics, twist grain boundary phases or blue phases and even all phases from discotic liquid crystals are not listed. Nomenclature and description of those phases can, among others, be found in Dierking (2004).

To give a brief introduction into these mesophases, we will start a hypothetical cooling procedure from the isotropic melt and describe the phases and its properties.

1. **Nematic phase:** Represents the phase with the lowest level of ordering. It consists of long range orientational order of the long molecular axis in a certain direction, the so called director **n**, which presents the average direction of the long axis and is equal to the optical axis of the system. In fig. 3.7(a) a schematic drawing of the nematic phase, including the direction of **n**, can be seen. There is no, or only very short range positional order at all, i.e. the molecules centers of mass exhibit a random distribution.

2. **Smectic phases:** Lowering the temperature, we get to the regime of smectic phases. Next to the orientational order from the nematics, additional positional ordering is introduced to the centers of mass. This positional order is usually long-ranged in one dimension whilst a variety of different smectic phases can be defined according to the degree of in-plane ordering:

   - SmA,SmC: These phases can be thought as 2-dimensional liquids. Both exhibit a layered structure and appear liquid like within the layers itself. The difference actually is the molecular ordering relative to the layer normal. In the SmA state, the director is perpendicular to the layer normal whilst in the SmC phase, the director is tilted away with a certain angle $\Theta$ (usually between 25°- 35°). Due to the fact that the director defines the optical axis, they can be distinguished quite easily by the means of polarizing light microscopy. A schematic drawing of the SmA phase can be seen in fig. 3.7(b).

   - SmB,SmI,SmF: The next step in our sequence of ordering is built by long range orientational, plus defined but still short range positional order within the smectic layers, so called "bond-orientational order" (Dierking, 2004). The molecules are arranged in hexagonal patterns in plane. Depending if they are tilted or not, it can be further distinguished between SmB (untilted), SmI (tilted to apex) and SmH (tilted to side).

3. **Soft Crystal phases:** Further cooling finally brings us to the range of so called soft crystals. The main difference to the smectics is that positional order is very defined and long-ranged in all dimensions and therefore resistant against defects. Especially K and H, with an monoclinic distribution of the centers of mass, are very close to the final crystalline structure.

As stated above C8-BTBT exhibits only one mesophase, namely a smectic A phase. Thus, the following chapter will provide theoretical description about this phase.

## 1.2.2. Theoretical approach of the Smectic A phase

The microscopic definition of nematics and the related low ordered SmA phase is based on the introduction of a so called order parameter.

Since orientational order is introduced with the nematic phase, we will start our theoretical description with nematics. Due to the quadrupole-type symmetry of uniaxial nematics, order is characterized by a second rank symmetric traceless tensor $Q_{\alpha\beta}$ (Dietrich, 1998),(Dierking, 2004).

$$Q_{\alpha\beta} = S(n_\alpha n_\beta - \frac{1}{3}\delta_{\alpha\beta}) \tag{1.1}$$

where $n_{\alpha,\beta}$ specifies the preferred orientation of the director $\mathbf{n}$. The scalar parameter $S$ describes the degree of ordering:

$$S = \langle \frac{3\cos^2\theta_i - 1}{2} \rangle \tag{1.2}$$

The brackets $\langle .. \rangle$ denote the statistical average (see fig. 3.7(a)). For isotropic liquid, where the director distribution $S\langle n_\alpha n_\beta \rangle = 1/3$, $Q_{\alpha\beta}$ becomes zero, which is equal to complete disorder.

As described above, the only difference between nematic and SmA is long range positional order along the long axis (see fig. 3.7(b)). Therefore, we can use (1.2) to describe orientational order and introduce a second term $\cos(\frac{2\pi}{d}z_i)$ to consider positional order (McMillan, 1971) giving:

$$\sigma = \langle \frac{3\cos^2\theta_i - 1}{2} \cos(\frac{2\pi}{d}z_i) \rangle \tag{1.3}$$

where $\sigma$ denotes the smectic order parameter, $z_i$ the centers of mass positions and $d$ the periodicity, i.e. the smectic layer spacing $d_{SmA}$.
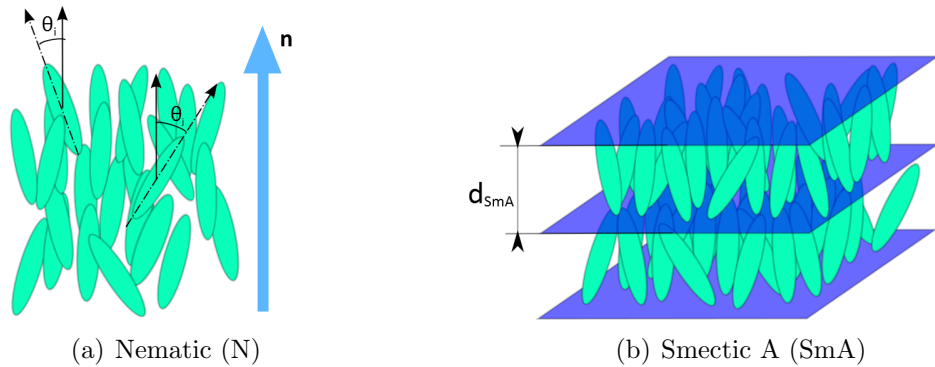


(a) Nematic (N)  (b) Smectic A (SmA)

**Figure 1.4.:** Schematic drawing of a) the nematic phase including the director $\mathbf{n}$ and b) the SmA phase including positional order along the molecular long axis.

## 1.3. dialkyl-benzothieno-benzothiophene, $C_n$-BTBT

Recently, there has been a high interest in *"dialkyl-benzothieno-benzothiophene"*. As for most novel organic materials, this is due to their possible application as an active layer in organic devices like TFT's or OLED's. The interest is reflected by quite a number of recent publications in well known journals Takafumi Izawa (2008),Liu et al. (2010),Iino and Hanna (2006). Next to the TFT-characteristics (mobility $\mu$, On-Off-ratio $\frac{I_{ON}}{I_{OFF}}$ and threshold voltage $V_{th}$), it is of great interest to find materials suitable for films that can simply be produced by the means of solution processes like spin-coating, drop-casting or ink-jet procedures (see sec. 2). As both criteria are fulfilled by BTBT, it turns out to be a good candidate for soluble molecular semi-conductors. The chemical structure can be seen in fig. 1.5(a). The molecule core consists of two merged *thiophene*-, and two *phenyl*-rings. To gain solubility, two solubilizing di-alkyl side chains are introduced in the long-axis direction of the core. For C8-BTBT they consist of 8 carbon atoms and 17 hydrogen atoms each. It was shown by (Ebata



| $n$ | solubility[a] (g L$^{-1}$) | d-spacing (Å) | $\mu_{FET}$[b] (cm$^2$ V$^{-1}$ s$^{-1}$) | $I_{on}/I_{off}$[b] | $V_{th}$[b] (V) |
|---|---|---|---|---|---|
| 5 | >60 | 22.8 | 0.16−0.43 | $10^8$ | −21 |
| 6 | 70 | 24.5 | 0.36−0.45 | $10^8$ | −25 |
| 7 | 70 | 27.1 | 0.52−0.84 | $10^7$ | −29 |
| 8 | 80 | 29.0 | 0.46−1.80 | $10^7$ | −17 |
| 9 | 90 | 31.6 | 0.23−0.61 | $10^8$ | −21 |
| 10 | 24 | 33.3 | 0.28−0.86 | $10^8$ | −23 |
| 11 | 13 | 35.9 | 0.73−1.76 | $10^7$ | −20 |
| 12 | 8.6 | 37.5 | 0.44−1.71 | $10^8$ | −20 |
| 13 | 5.0 | 40.2 | 1.20−2.75 | $10^7$ | −27 |
| 14 | 2.3 | 41.8 | 0.19−0.72 | $10^8$ | −18 |

[a] Concentration of saturated solution in chloroform at room temperature.
[b] Typical device characteristics obtained from more than 10 devices.
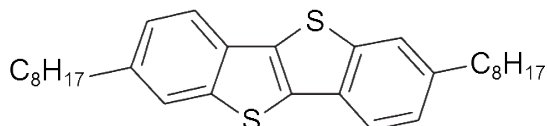
(a) ($C_{30}H_{40}S_2$)                    (b) FET-characteristics

**Figure 1.5.:** a) Chemical structure of C8-BTBT and b) FET-characteris of $C_n$-BTBT devices on Si/SiO$_2$-substrates according to Iino and Hanna (2006)
.

et al., 2007) that the alkyl-chain length is an important parameter for $\mu_{FET}$-values as it has a high impact on the intermolecular interaction of the BTBT-core layers. This leads to the statement: The longer the alkyl chains, the higher the reachable device performance. On the other hand, the solubility and therefore the possibility to produce films by solution based methods decreases once the alkyl chains exceeds a certain length (see table 1.5(b)).

This concludes, that *dioctyl*-BTBT seems to be one of the most promising candidates out of the $C_n$-BTBT-series.

### 1.3.1. DSC

Differential scanning calorimetry (DSC) has been performed by the group of Y. Geerts from the Universite libre de Bruxelles (ULB) in Brussels. Fig 1.6 shows the three

phases obtained by BTBT for the bulk material. As can be seen, a transition from crystalline to the liquid crystalline phase occurs in the range of 110°C. The phase turns out to be smectic A (see chapter 1.2 and 6.4). A $2^{nd}$ transition occurs at 125°C, where the material finally becomes isotropic. The cooling curve indicates the same transitions, including a temperature shift that results from the cooling rate applied.
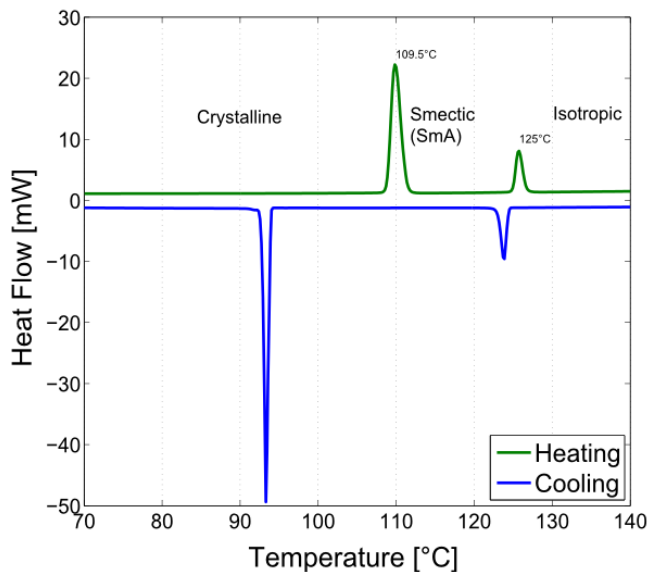


| Phase | $Temperature/°C$ |
|---|---|
| *Crystalline* | $< 108,9$ |
| *Smectic (SmA)* | $108,9 - 125$ |
| *Isotropic* | $> 125$ |

**Figure 1.6.:** DSC of *BTBT*(left) and dedicated temperature ranges of the different phases(right).

## 1.3.2. Packing structure

It is well known that charge transport is highly dependent on the overlap of molecular orbits of adjacent molecules. Thus, to understand charge transport within the semiconducting layer, it is mandatory to know the crystalline structure of the thin films.

In order to reveal molecular ordering of the solid state, single crystal x-ray structure analysis has been performed on a series of $C_n$-BTBT by the group of Takafumi Izawa (2008). Fig. 1.7**a** reveals a monoclinic crystal structure (space group P21/a) with a tilt angle of the unit cell of $\beta = 92,443°$. The molecular ordering of the aromatic core appears to be a herringbone-like structure which is very common for this kind of molecules. Furthermore, out of plane x-ray measurements of spin coated thin films indicated an interlayer-distance matching the c-axis of the single crystal unit cell. Due to these results and the in-plane structure, it is concluded that the structure of the thin film equals the bulk single crystal structure. As mentioned before, strong intermolecular overlap is considered to be a main factor when it comes to realise high performance FET-device. Therefore, the high values gained by C8-BTBT is directly related to the herringbone packing which enables 2D carrier transport and is further

enhanced by a network of intermolecular interactions through short sulfur-sulfur contacts (Ebata et al., 2007).
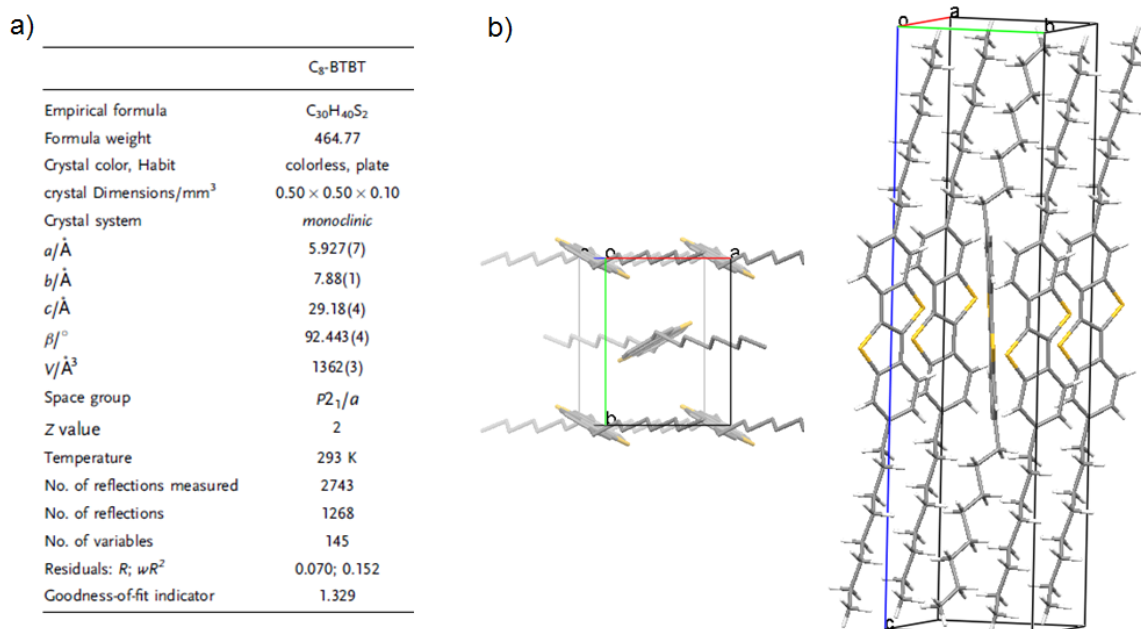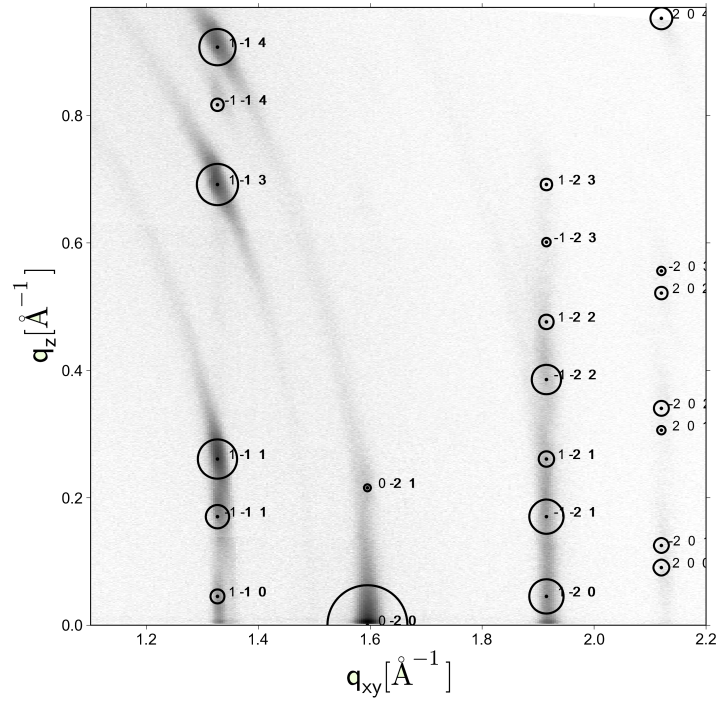


| | $C_8$-BTBT |
|---|---|
| Empirical formula | $C_{30}H_{40}S_2$ |
| Formula weight | 464.77 |
| Crystal color, Habit | colorless, plate |
| crystal Dimensions/mm³ | $0.50 \times 0.50 \times 0.10$ |
| Crystal system | monoclinic |
| $a/\text{Å}$ | 5.927(7) |
| $b/\text{Å}$ | 7.88(1) |
| $c/\text{Å}$ | 29.18(4) |
| $\beta/°$ | 92.443(4) |
| $V/\text{Å}^3$ | 1362(3) |
| Space group | $P2_1/a$ |
| Z value | 2 |
| Temperature | 293 K |
| No. of reflections measured | 2743 |
| No. of reflections | 1268 |
| No. of variables | 145 |
| Residuals: $R$; $wR^2$ | 0.070; 0.152 |
| Goodness-of-fit indicator | 1.329 |

**Figure 1.7.:** a) Single crystal solution and b)packing structure of BTBT(left) according to Takafumi Izawa (2008). Hydrogen atoms have been omitted for illustration purposes.

For verification, thin films have been produced (see sec. 2) in order to compare thin - film structure with the packing structure of the single crystal solution. Grazing incidence x-ray diffraction (GIXD) measurements have been performed on films with different thickness and compared with the single-crystal unit cell. The results can be seen in fig 1.8. There is a very high level of agreement regarding the position of the peaks for both, the thick and the thin film. Additionally, the structure file has been used to compare the intensities of the diffraction spots with the calculated intensities(circles). As those intensities do fit very well too, it is very likely, that the thin film structure is equal to the bulk crystal structure stated above.

To investigate polymorphism, GIXD measurements have been performed on films with thickness varying from $d = 3 - 200nm$, as well as temperature dependent measurements covering the whole range from room temperature up to the isotropic phase. Surprisingly it turns out that $C_n$-BTBT films are actually isostructural, as no other phase than the monoclinic structure was found. This is in contrast to most other small molecules, which tend show polymorphism, especially in presence of a surface or interface (Mattheus et al., 2001),(Wedl et al., 2012).

(a) Thick film ($100nm$)
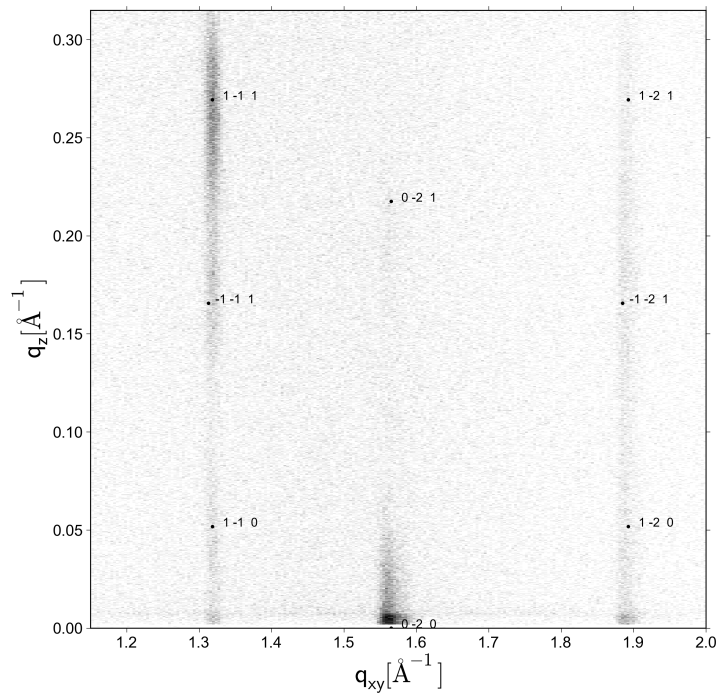


(b) Thin film (monlayer, $3nm$)

**Figure 1.8.:** Reciprocal spacemaps of the a)thick and b)thin C8-BTBT-film indexed with the single crystal unit-cell of fig.1.7.

# 2. Film preparation

Thin film fabrication has become one of the major topics when in it comes to industrial production of electronic devices like OFET's, OLED's or organic solar cells on large scale.

As a result, processability of promising semiconducting materials gains high interest and is highly important when it comes to exploring new materials. Cost extensive and time consuming techniques like vacuum evaporation are replaced by simple, low cost and solution-based methods of film fabrication like:

- Drop-Casting (see chapter 2.3)

- Spin-Coating (see chapter 2.3)

- Ink-Jet printing.

Among others, it was shown by Iino and Hanna (2006) that there are plenty of liquid-crystalline materials, including *C8-BTBT*, available for solution processing of poly-crystalline thin films.

## 2.1. Wafer treatment

Thin films have been produced on Si-wafers with a 150 nm thermally grown $SiO_2$-layer on top. The wafers have been retrieved from Siegert Consulting e.K. (Aachen, Germany). The roughness has been determined by x-ray reflectivity to be in the range of 0.5 nm.

Prior to film fabrication, the wafers have been prepared by performing following cleaning steps:

1. cleaning and purging with acetone.

2. cleaning and purging with isopropyl alcohol.

3. ultrasonic bath in acetone for 20 minutes.

4. purging with isopropyl alcohol.

The purity of the substrates was verified by optical microscopy and, if necessary, the steps mentioned above were repeated. The total surface energy of the cleaned wafers has been estimated to be $\sigma$=49.58 $\frac{mN}{m}$. In order to keep reproducibility, wafer treatment has not been altered at any time as it is well known that the condition of the substrate can have a high impact on the thin-film structure and morphology.

## 2.2. Solution preparation

To vary film thickness, a broad range of tetrahydrofuran (THF) solutions with different molecular concentrations has been produced. The boiling point of THF is 65.81°C and therefore far below the liquid crystalline phase of C8-BTBT. Additionally, the vapour pressure is rather high (173 mbar at 20°C). Thus, evaporation under ambient conditions is very fast and the influence of the solvent should be neglectible shortly after fabrication, especially when reaching the phase transition temperature of 110°C. Next to this, B.Wedl investigated thin film production with different solvents and obtained very good results using THF as solvent for *DH3T*, a small molecule comparable to our material (Wedl et al., 2012).

Due to the fact that the spin-coating parameters were kept constant for all samples (see sec. 2.3), the molecular concentration in the solution was used to adjust the thickness of the thin films we produced. Different solutions and related film thickness can be seen in table 2.1. The film thickness was determined by the means of x-ray reflectivity (see sec. 3.1.2).

| Solution | $c \frac{mg}{ml}$ | *Information* |
|---|---|---|
| L1 | 1.36 | $\sim 5$ Layer |
| L2 | 0.85 | $\sim 4$ Layer |
| L3 | | *produced for thin-down purposes* |
| L4 | 5.43 | $\sim 15 - 18$ Layer |
| L5 | 3.25 | $\sim 10 - 12$ Layer |
| L6 | 0.41 | $\sim 3 - 4$ Layer |
| L7 | 0.27 | $\sim 1 - 2$ Layer |
| L8 | 2.10 | $\sim 6 - 7$ Layer |
| L9 | 0.33 | $\sim 2 - 3$ Layer, monolayer after fabrication |
| L10 | 1.10 | $\sim 4 - 5$ Layer, Intermediate film |
| L11 | 0.19 | $\sim 1$ Layer, monolayer after fabrication |
| L12 | 10.1 | $\sim 25 - 30$ Layer, Thick-film |
| L13 | 0.09 | fabricated for submonolayer investigations |
| L14 | 0.28 | $\sim 1$ Layer, Thin film |
| L15 | 0.27 | Thin film |
| L16 | 1.11 | Intermediate film |
| L17 | 10.43 | Thick film |

**Table 2.1.:** Prepared solutions of C8-BTBT in THF for thin film fabrication including the nominal layer thickness observed by x-ray reflectivity after dewetting (see chapter 5.2)
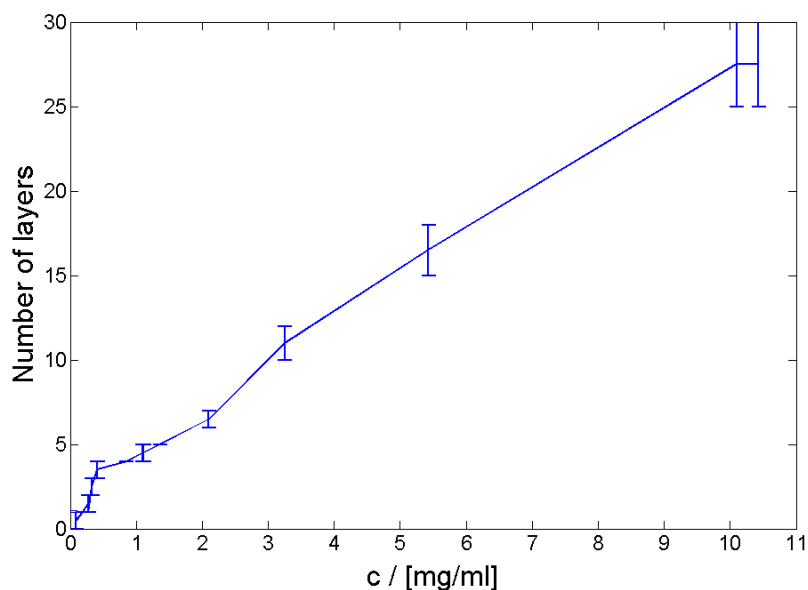
**Figure 2.1.:** Layer thickness versus concentration of the C8-BTBT in THF solution.

Detailed investigations have been performed on the following samples:

- Thick-film: Spin coated from the solutions L12 and L17 ($\approx 10.3\frac{mg}{ml}$). After spin-coating, a film thickness in the range of 100 nm representing a film consisting of $\sim 30$ layers was obtained. Results can be seen in chapter 6.

- Thin-film: Spin coated from the solutions L14 and L15 ($\approx 0.35\frac{mg}{ml}$). The film thickness obtained after spin coating was in the range of 3 nm, representing a monolayer. Results can be seen in chapter 5.

- Intermediate film: Spin coated from the solutions L10 and L16. The film thickness obtained after spin coating was in the range of 15 nm representing a film consisting of $\sim 4 - 5$ layers.

## 2.3. Spin-Coating/Drop-Casting

### 2.3.1. Drop-Casting

Drop-Casting is the most simple method of creating solution based thin films. A drop of the solution is placed on the substrate and left until the solvent is completely vaporised (see fig. 2.2). Due to local fluctuations and limited or missing control of parameters like the vaporisation rate, the film is very undefined in terms of uniformity, thickness and usually obtains high roughness. As a result, films produced by drop-
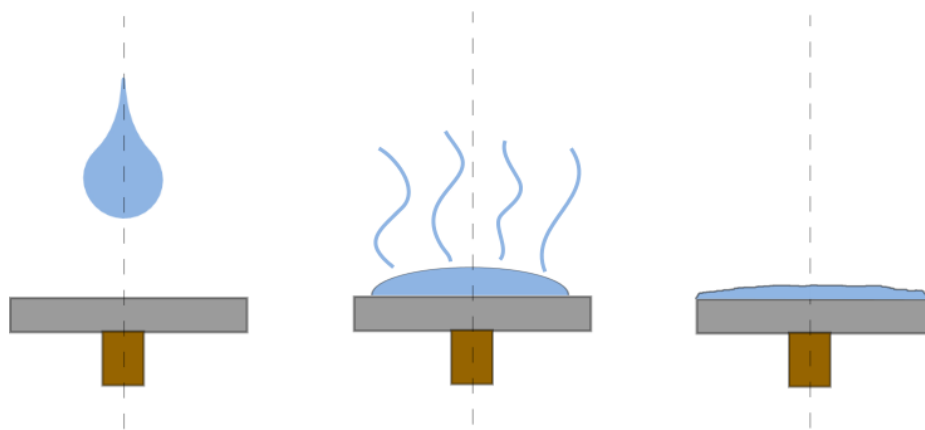


**Figure 2.2.:** Schematic representation of the drop-casting process. The film is gained by placing and evaporation of a drop of the solution

casting can only be used for qualitative analysis. Drop-casted C8-BTBT-films have been prepared to investigate the bulk structure of the material. Results of the drop-casted film-structure can be seen in fig. 1.8(b).

### 2.3.2. Spin-coating

The most common solution method to create uniform thin films is spin-coating. Fig 2.3(b) illustrates the two mechanisms responsible for film thinning. Initially, the outflow of the drop due to centrifugal forces dominates. Once excessive material is spun off the substrate and the radial flow decreases, solvent evaporation becomes the dominating effect. Fig. 2.3(a) illustrates the steps of the spin-coating process:

1. Solution deposition: A drop of the covering solution is placed on the substrate.

2. Spinning of the substrate: The wafer is accelerated and rotated at a constant level for a specific time. Due to the rotational forces an outflow of the fluid material occurs, leading to a defined layer dependent on both, the final speed of rotation and the time the sample is rotated.

3. Solvent evaporation: Evaporation takes places once the drop is placed on the substrate and happens simultaneously to step 2. The evaporation rate is highly dependent on the vapour pressure of the solvent.

For our films, 120 $\mu l$ of the solutions from table 2.1 has been placed on the substrate, followed by spin-coating in a flow box using a spin speed of 1000 rpm for 9 sec and 1500 rpm for another 30 seconds.
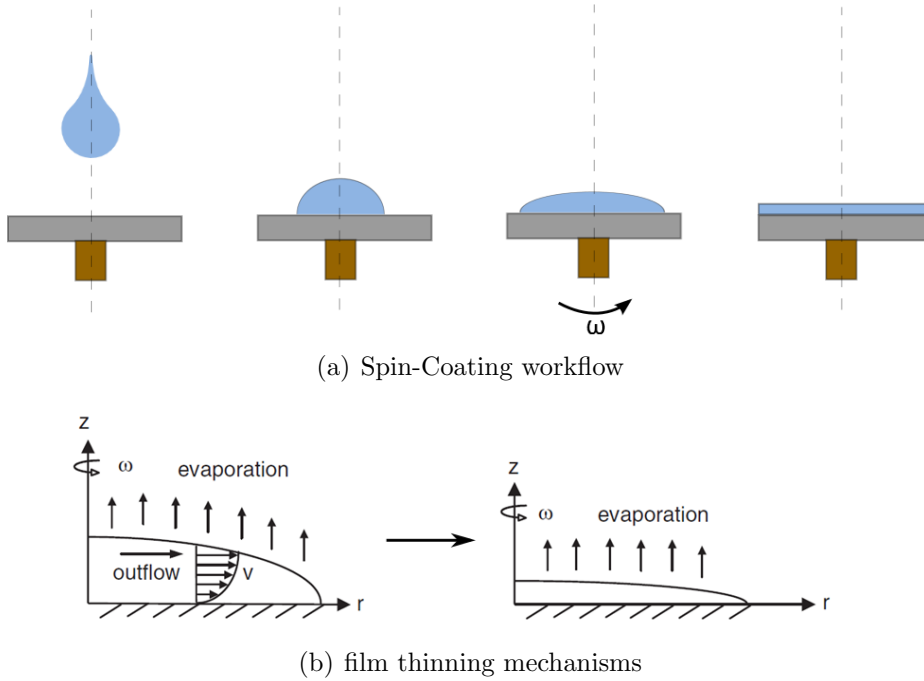


(a) Spin-Coating workflow



(b) film thinning mechanisms

**Figure 2.3.:** Schematic representation of a) the spin-coating steps and b) the evaporation and outflow of the solvent on the substrate according to (Yimsiri and Mackley, 2006)

# 3. Experimental Methods

Within the next two chapters, we will introduce two methods of x-ray analysis that operate in the so called small-angle regime of total reflection. These are x-ray reflectivity (XRR) and grazing incidence x-ray diffraction (GIXD) experiments, two major x-ray mechanisms for thin film investigations.

Next to this, we will give a brief introduction into atomic force microscopy as well as polarizing light microscopy. Those experiments have been carried out in order to confirm the results gained by XRD methods.

## 3.1. Optical properties of X-rays - Snell's law, Fresnel equations and the critical angle

In order to understand the working principle of x-ray investigation methods operating at small incident angles, we will first give a short introduction into the optical properties of x-rays before we get to a detailed description about XRR and GIXD in chapter 3.1.1 and 3.1.2.

As well as all other kinds of electromagnetic waves, x-rays experience an influence of the surrounding environment when penetrating through materials. Refraction takes place, once a wave crosses the interface between two media. This is due to the change of the optical density, described by the refractive index $\mathbf{n}$. The wave propagation itself is often described by the well know Helmholtz equation:

$$\Delta \mathbf{E}(\mathbf{r}) + k^2 n^2(\mathbf{r}) \mathbf{E}(\mathbf{r}) = 0 \tag{3.1}$$

where $\lambda$ stands for the wavelength and $k = \frac{2\pi}{\lambda}$ denotes the modulus of the wavevector $\mathbf{k}$. The refractive index is defined as the ratio between the speed of light in vacuum and the phase speed within a medium $\frac{c_0}{c_m}$. Thus, $\mathbf{n}$ depends on the interaction between the electromagnetic wave and the electronic state within the molecule or atom.

Snell's law provides a simple geometrical description of the directional change of the propagating wave:

$$\frac{\cos \alpha_1}{\cos \alpha_2} = \frac{n_1}{n_2} \tag{3.2}$$

According to Tolan (1998), the refractive index can be written as

$$n(\mathbf{r}) = 1 - \delta(\mathbf{r}) + i\beta(\mathbf{r}) \tag{3.3}$$

where

$$\delta = \frac{\lambda^2}{2\pi} r_e \rho_e \qquad (3.4)$$

denotes the refractive index, depending on the electron density($\rho_e$), the wavelength($\lambda$) and the classical electron radius ($r_e = 2,8179 * 10^{-15} m$).

$$\beta = \frac{\lambda}{4\pi} \mu_x \qquad (3.5)$$

describes the absorption term depended on $\lambda$ and the linear absorption coefficient $\mu_x$. Usually, $\delta$ is of order $10^{-6}$ whilst $\beta$ is two magnitudes smaller, i.e. of order $10^{-8}$. Hence, **n** is unity for air and vacuum and becomes slightly smaller than one for a medium. The fact of the refractive index being always smaller than 1 ($n < 1$) brings us to an important property of x-rays, the critical angle of total reflection $\alpha_c$. Total external reflection occurs once the incident angle ($\alpha_i$) is smaller than $\alpha_c$. In this region, all incoming radiation is reflected and does not penetrate through the medium any longer. It can be simply derived from the law of Snellius and gives:

$$\alpha_c = \sqrt{2\delta} = \lambda \sqrt{\frac{r_e \rho_e}{\pi}} \qquad (3.6)$$

As mentioned, $\delta$ is rather small and therefore, $\alpha_c$ is usually quite small too. E.g. Using $CuK_\alpha$ radiation ($\lambda = 0.154179$ nm), the critical angle for silicon is $\alpha_{c-Si} = 0.223°$ or $\alpha_{c-C8BTBT} = 0.156°$ for C8-BTBT.

**The evanescent wave**

Fig. 3.1(a) shows how an incident electromagnetic wave $\mathbf{k_i}$ gets splitted into an reflected $\mathbf{k_r}$ and a transmitted component $\mathbf{k_t}$. The transmitted wave can be rewritten to

$$\mathbf{E_t} = t\mathbf{E_i} \exp i(\mathbf{k_t r} - \omega\tau) \qquad (3.7)$$

where t denotes the transmission coefficient. Using Snell's law (3.2) we find, that the x-component $k_{t,x}$ is equal to $k_{i,x}$ whilst for the z-component we get

$$k_{t,z} = k\sqrt{n^2 - 1 + \sin \alpha_i{}^2} \qquad (3.8)$$

Using (3.3), the transmitted wave finally becomes

$$\boldsymbol{E}_t(\boldsymbol{r}) \propto t e^{i(k\cos(\alpha_i)x + Re\{k_{t,z}\}z)} e^{-Im\{k_{t,z}\}z} \qquad (3.9)$$

For small angles and neglecting absorption, we get a simple criteria ($\alpha_c^2 = 2\delta$)

$$k_{t,z} \approx k\sqrt{\alpha_i^2 - \alpha_c^2} \qquad (3.10)$$

This reveals the dependency of the z-component on the incident angle. For $\alpha_i < \alpha_c$, $k_{t,z}$ is purely imaginary and as an effect eq. (3.9) describes a wave travelling parallel

to the surface in x-direction. In z-direction this wave is is exponentially damped, the so called **evanescent wave**.

Fig. 3.1(b) shows the dependence of the absolute value of transmission on the incident angle $\alpha_i$ for different materials, i.e. different combinations of the refractive index $\delta$ and absorption $\beta$. The most important feature is the maximum of $\mid t \mid$ once the incident angle $\alpha_i$ equals the critical angle $\alpha_c$. As can be seen in fig. 3.1(b), the incident, reflected and transmitted wave get coupled coherently, leading to an increase of the transmitted amplitude by a factor of two at $\frac{\alpha_i}{\alpha_c} = 1$ (Dosch, 1992), (Vineyard, 1982). For pentacene, zero absorption ($\beta \sim 0$) leads to a very sharp peak whilst for silicon or gold, increased absorption leads to a palm off.
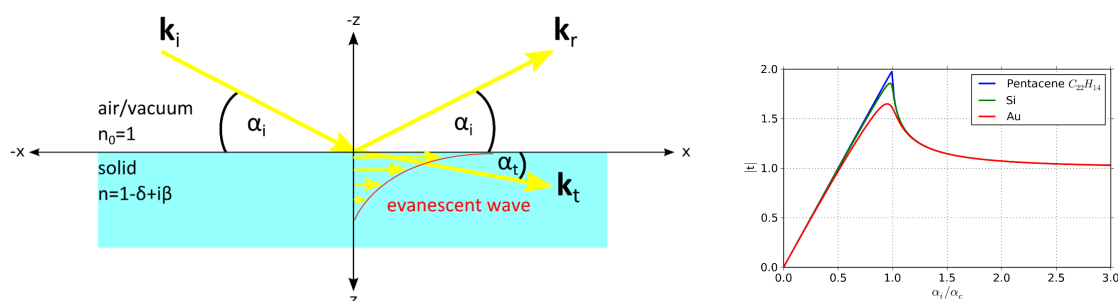


(a) Schematic representation of the evanescent wave

(b) Transmission function of different media

**Figure 3.1.:** a) Splitting of an incident wave into a transmitted an reflected component. The evanescent wave gets formed below the critical angle $\alpha_c$. It travels parallel to the surface with exponential decay along the z-direction. b) Absolute value of the transmission function indicating the dependence of the transmitted intensity on the incident angle (Neuschitzer, 2012).

In order to calculate the reflectivity and transmission of a single vacuum/medium interface, we consider the incoming wave $\mathbf{k_i}$ hitting a surface at a grazing angle $\alpha_i$ (see fig. 3.1(a). The tangential component[1] has to be continuous at the surface. Thus, we can derive the amplitudes of the transmitted and reflected wave as a function of the incident angle by simple geometric deliberations:

$$r = \frac{k_{i,z} - k_{t,z}}{k_{i,z} + k_{t,z}} \rightarrow R_F = \mid r \mid^2 \tag{3.11}$$

$$t = \frac{2k_{i,z}}{k_{i,z} + k_{t,z}} \rightarrow T_F = \mid t \mid^2 \tag{3.12}$$

These formulas are the well know Fresnel-equations. $R_F$ and $T_F$ denote the intensities of reflected and transmitted wave. Obviously, these are the quantities obtained in an experiment.
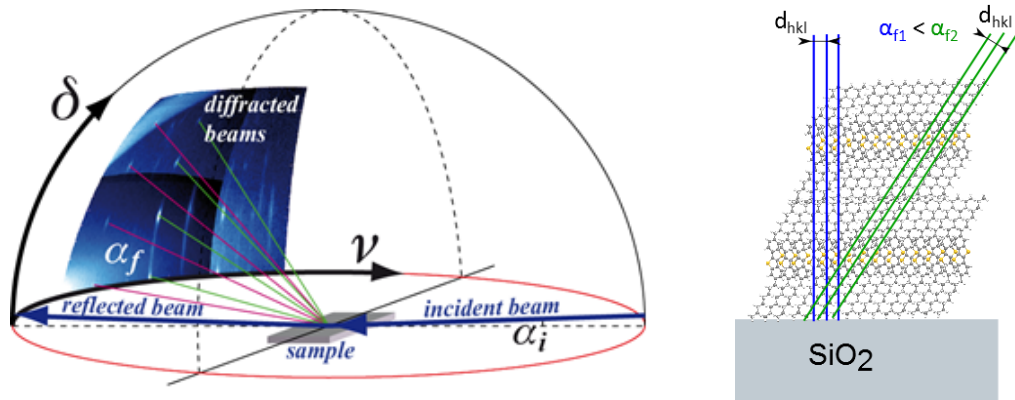
---

[1]This is the x-component for linearly polarized light with the y-vector perpendicular to the scattering plane

Based on these optical properties of x-rays, we will now proceed with an introduction into the methods grazing incidence diffraction and x-ray reflectivity.

### 3.1.1. Grazing incidence x-ray diffraction (GIXD)

Grazing-incidence diffraction is a scattering geometry, that makes us of both, the Bragg condition for x-ray diffraction as well as the conditions for x-ray total external reflection from crystal surfaces. It is based on the detection of diffraction from lattice-planes(hkl) of the so called *evanescent* wave (see sec. 3.1). This wave travels along the surface in a parallel way and therefore the scattering vector **q** lies in-plane, which leads to scattering of lattice planes that are located perpendicular to the surface. Due to the small incident angle, the penetration depth is rather small and thus, GIXD is well suited to obtain lateral crystallographic information from thin -textured films.

Fig. 3.2(a) gives a schematic representation of a GIXD experiment. The diffracted spots are usually captured by a 1D or 2D detector that is moved around the sample. By increasing the final angle $\alpha_f$ it is furthermore possible to capture out-of-plane periodicities as depicted in fig. 3.2(b). All together, this method allows to capture parts of the reciprocal spacemap in terms of tuples ($q_{xy}$ and $q_z$) in a single experiment.



(a) Schematic drawing of a GID-experiment. The detector is moved around the sample ($v$-anlge). $\delta$ denotes the direction of the final angle $\alpha_f$ of the detector.

(b) Accessibility of different lattice planes with distinct interlayer distances $d_{hkl}$

**Figure 3.2.:** a)Schematic drawing of a GIXD-experiment. For a number of lattice planes, the diffraction conditions are fullfilled leading to diffraction spots in the reciprocal space map according to Salzmann (2008) b) Accessibility of out-of-plane periodicities by increasing the detector angle $\alpha_f$.

One of the major advantages is indeed the surface sensitivity. Due to the small incident angle, usually below 0.5°, most of the incoming wave gets reflected whilst only parts are able to penetrate through the material. The penetration depth can be adopted by mounting the incident angle and is close to 0 below the critical angle. To give a

number, the penetration depth is below 1 nm for $\alpha_i < \alpha_c$ while it exceeds 100 $\mu$ m in specular conditions (A. Gibaud, 2000). Next to this, scattering from the substrate is suppressed which in return leads to an enhanced signal-noise ratio.

However, there is a big disadvantage. Due to the very small active material ($\propto$ to the penetration depth), the scattering volume is very small and thus, the diffracted intensity is very low. Usually synchrotron sources are mandatory for GIXD experiments.

## 3.1.2. X-ray reflectivity

The second important XRD-method for thin-film investigations is x-ray reflectivity (XRR). Due to the low incident angle, this is a surface-sensitive analytical technique like GIXD presented in the last chapter.

The basic idea behind XRR is to use small incident angles, usually between 0.1° and 10°. This leads to reflection of the x-rays from a flat surface, thin film or multilayer stack according to (3.11). The reflected beam is then detected in specular conditions $\alpha_i = \alpha_f$.

Fig.3.3 shows the XRR-scheme. As can be seen, the incident beam splits up into a reflected component and a transmitted part that penetrates through the media and gets reflected at all interfaces down to the substrate. As an effect, the beam detected in specular conditions on the secondary side contains information of

- Film thickness ($\mathbf{d_1}$,$\mathbf{d_2}$)

- Electron densities of the different media ($\rho_{e\mathbf{s}}$,$\rho_{e\mathbf{1}}$,$\rho_{e\mathbf{2}}$)

- Surface ($\sigma_{\mathbf{3}}$) and interface roughness ($\sigma_{\mathbf{1}}$,$\sigma_{\mathbf{2}}$)

as depicted in fig.3.4. Due to this huge amount of information gained in XRR measurements, data analysis is rather complex. A short introduction into the most common methods of data evaluation, namely Parrat's formalism will be given in at the end of this chapter.
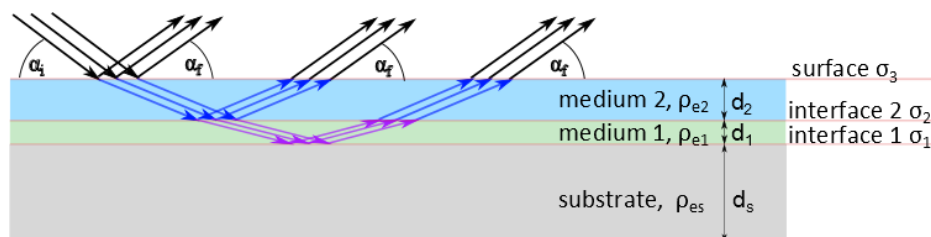


**Figure 3.3.:** Schematic of a XRR-experiment indicating the transmission and reflection of the incident beam at the different interfaces.

(a) Film Thickness     (b) Electron density     (c) Surface/interfce roughness
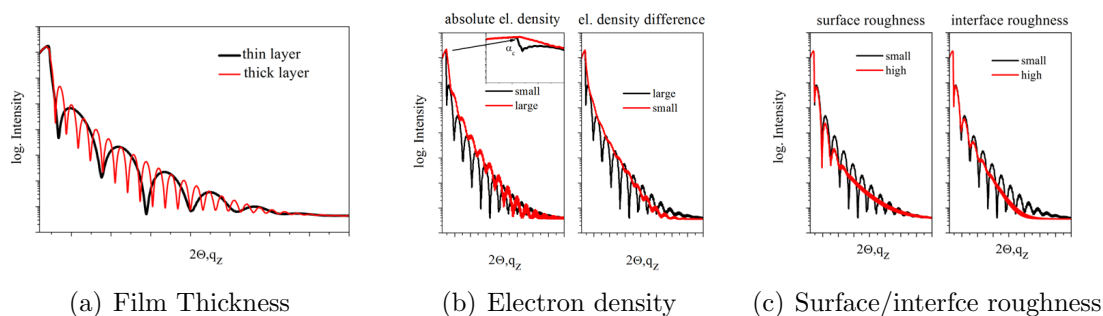
**Figure 3.4.:** X-ray reflectivity curves showing the influence of a) different film thickness b) electron densities and c) roughness on the resulting XRR- curve (Neuhold, 2012).

The basic mathematical relation to describe reflectivity from sharp interfaces without roughness is given by

$$R_F = \frac{q_c^4}{16q^4} \tag{3.13}$$

and can be derived from Fresnel's formulas. Here, $q_c$ denotes the critical wave vector that is directly related to the critical angle $\alpha_c$ by

$$q_c = \frac{4\pi \sin \alpha_c}{\lambda} \approx 3.75 * 10^{-2}\sqrt{\rho_e} \tag{3.14}$$

and thus is a direct measure for the electron density within the sample [2]. $q_c$ somehow separates the reflectivity curve into three regimes:

1. $q < q_c$: Regime of total external reflection, R=1.

2. $q = q_c$: Steep decrease of R

3. $q > 3q_c$: Typical $R \propto \frac{1}{q^4}$

Due to this immense drop-off with $q^{-4}$, x-ray reflectivity curves are usually plotted in logarithmic scale as can be seen in fig.3.4 (Tolan, 1998),(Als-Nielsen and McMorrow, 2001),(Beiglboeck, 2009).

However, in reality, there are several features, like roughness or inhomogeneous layers leading to a deviation from the Fresnel-reflectivity. We will proceed with two common methods that allow to analyize density profiles of multilayer stack as well as the roughness of the surfaces and interfaces that contribute to the reflectivity signal.

**Parrat's formalism**

Lyman G. Parrat introduced a technique to derive the reflectivity of a multilayer-stack (Parratt, 1954). Over the years, it has been extended to a wide range of solid and

---

[2]The approximation was calculated with $CuK_\alpha$ radiation

liquid interfaces and became one of the basic routines used in XRR-software packages like X'Pert Reflectiviy from Panalytical or GenX (Björck and Andersson, 2007).

To understand the recursive formalism of Parrat, we will start with the reflectivity from a single homogeneous layer on a semi-infinite substrate. The situation is nearly equal to sec. 3.1 where we derived the Fresnel-equations to calculate the reflected and transmitted intensity. The only difference is that now the beam is able to pass further interfaces i.e. to penetrate into the substrate or underlying media. All possibilities of refraction and transmission in a single layer system can be seen in fig. 3.5a.

These are:

1. Reflection on the vacuum/medium interface leading to a reflected wave with amplitude $r_{01}$.

2. Transmission at the vacuum/medium interface leading to $t_{01}$. This wave gets reflected at the medium/substrate interface giving $r_{12}$ and finally transmission at the vacuum/medium interface $t_{10}$. In order to add this wave to $r_{01}$ we need to add a phase-factor that compensates the path difference. It can be easily derived by geometrical considerations and is equal to $e^{iqd}$.

3. Transmission at the vacuum/medium interface $t_{01}$, reflection at the medium/substrate interface $r_{12}$, reflection at the vacuum/medium interface $r_{01}$ and at the medium/substrate interface $r_{12}$ and a final transmission at the vacuum/medium interface $t_{10}$. Due to the multiple reflections, the phase factor to is $(e^{iqd})^2$ in this case.

Summing up, we get

$$r_{total} = r_{01} + t_{01}t_{10}r_{12}(e^{iqd})^2 + t_{01}t_{10}r_{10}r_{12}(e^{iqd})^4 + ... \tag{3.15}$$

$$r_{total} = r_{01} + t_{01}t_{10}r_{12}(e^{iqd})^2 \sum_{n=0}^{\infty}(r_{10}r_{12}(e^{iqd})^2)^n \tag{3.16}$$

Using the definition of a geometric series we can rewrite this formula to the more compact form

$$r_{total} = r_{01} + t_{01}t_{10}r_{12}(e^{iqd})^2 \frac{1}{1 - r_{10}r_{12}(e^{iqd})^2} \tag{3.17}$$

By using the Fresnel equation (3.11), we can rewrite (3.17) and finally get a rather simple expression for the reflection from a single layer

$$r_{slab} = \frac{r_{01} + r_{12}(e^{iqd})^2}{1 + r_{01}r_{12}(e^{iqd})^2} \tag{3.18}$$

An example of a single layer can be seen in fig. 3.4a or fig.5.8(a) where the $q^{-4}$ is overlapped by oscillations from a single layer, called Kiessig-fringes (Kiessig, 1931).
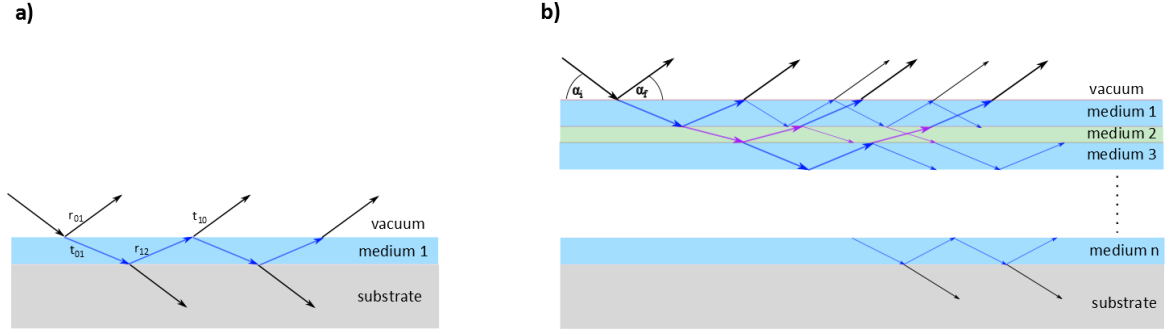
**Figure 3.5.:** Schematic drawing of reflection and transmission in a) a single-layer system and b) multiple reflections in a multilayer system

Those fringes are actually where information about layer thickness and electron density is stored and can be extracted.

Basically, this procedure of including multiple reflections and transmission can be enhanced to work for multiple layer systems as well. As mentioned, a more simple formalism was introduced by Parrat in 1954. His approach allows to calculate the reflectivity of multilayer-system with distinct electron densities in a recursive way.

Fig. 3.5b shows a multilayer stack with multiple reflections and transmissions down to the substrate[3]. As stated in sec. 3.1, the x-component of the transmitted wave-vectors is conserved and therefore equal for all layers $1 \rightarrow N$. The formalism starts at the medium n/substrate interface where the substrate is considered to be infinite and thus does no multiple reflections can occur. This is actually equal to the derivation of the Fresnel - reflectivity eq. 3.11 giving

$$r'_{n,substrate} = \frac{k_n - k_{substrate}}{k_n + k_{substrate}} \tag{3.19}$$

This is actually where the recursive approach starts. For the n-1st layer we can use eq. (3.18) and get

$$r_{n-1,n} = \frac{r'_{n-1,n} + r_{n,substrate}e^{id_n q_n}}{1 + r'_{n-1,n}r_{n,substrate}e^{id_n q_n}} \tag{3.20}$$

where $d_n$ denotes the thickness of the $n^{th}$ layer and $e^{iq_n d_n}$ considers the phase difference. This process is than repeated up to the vacuum/medium 1 interface where finally we end up with a formula representing the reflectivity $r_{0,1}$ which gives the total reflected intensity $R_{total} = \mid r_{0,1} \mid^2$ (Als-Nielsen and McMorrow, 2001).

---

[3]Due to the infinite substrate, there are no reflections from underneath the substrate to be considered for the first layer

Overall it must be noted that all XRR-curves in this work have been fitted with Parrat's formalism. Although it is the most common and a rather powerful method, very good knowledge of the investigated film structure is mandatory in order to get good results.

For the complex structures of C8-BTBT thin films, the arrangement of the molecules i.e. the crystal structure has to be known in order to fit e.g. a dewetted surface or formation of crystallites on a partially dewetted surface.

## 3.2. Atomic force microscopy

Invented in 1986 as an advancement of the scanning tunnelling microscope (Binnig and Quate, 1986) the atomic force microscope (AFM) has become one of the major tools for imaging, measuring and manipulating matter on nanoscale.

Fig. 3.6(b) shows a schematic drawing of an AFM (driven in tapping mode). It basically consists of a sharp tip that is scanning the sample. This tip is mounted on the so called cantilever. Once the tip is close to the surface, it experiences several forces and gets deflected according to Hook's law $(F = -k\Delta x)$[4]. Depending on the scanning mode used (see below), those forces include mechanical contact-, van der Waals-, capillary forces, etc. As can be seen in the picture, the deflection is measured by a photodetector which collects the reflection of a laser spot from the top surface of the cantilever (Vilalat-Clemente, 2008).

Depending on the interaction between tip and sample, three different modes can be applied:

- **Contact mode:** High resolution method (up to atomic scale) via direct contact of tip and sample surface. The deflection of the cantilever is proportional to the force acting on the tip $\Delta x \propto F_{tip}$. There are basically two ways to operate, namely constant-height, and more common, constant-force imaging where the latter is used to prevent damage of the tip and cantilever i.e. to get stuck on the sample surface.

- **Non-contact mode:** Operation in the regime of attractive forces. The sample is not influenced at all and therefore not damaged.

- **Tapping mode:** Cantilever and tip are oscillating at resonant frequency whilst moving across the sample surface. Due to less interaction with the surface, it is known to be non-destructive as well. Furthermore tapping allows a simultaneous collection of different data (see below).

For our purposes, the AFM was driven in tapping mode only. It allows to capture three different kind of images in a single scan:

1. Height/Topographic Image: Observed by monitoring the vertical position of the tip along the z-axis when scanning across the surface. Due to the periodical tipping, the scan speed needs to be rather slow in order to increase resolution. Fig. 3.6(b) illustrates a common height image of a C8-BTBT film.

2. Phase Image: Monitors the change in phase difference between the input drive signal and the measured phase of the oscillating cantilever. The offset is initially set to zero when the cantilever is freely oscillating in air. The phase offset

---

[4]$\Delta x$ represents the deflection, k the spring constant of the cantilever

observed is then related to the elastic properties of the sample surface due to different damping experienced while scanning the sample. This often allows to distinguish between different materials easily. E.g. the difference between C8-BTBT and the substrate can nicely be seen in fig. 3.6(c).

3. Amplitude Image: Captured by monitoring the amplitudes of the cantilever. These images usually show edges very well.
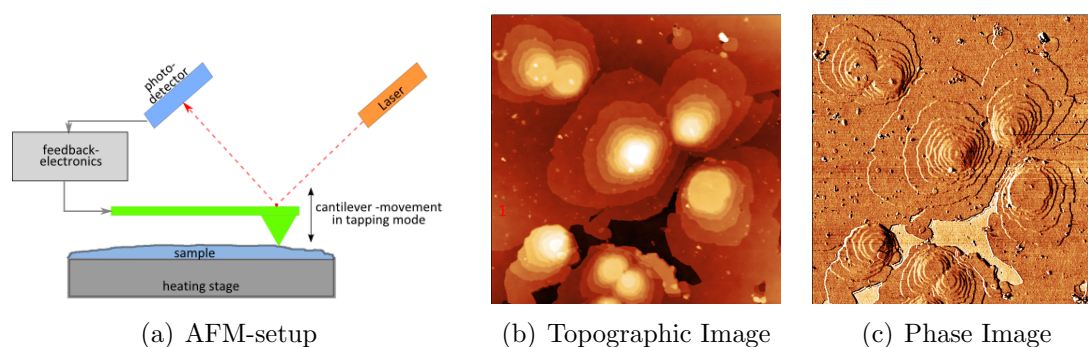


(a) AFM-setup (b) Topographic Image (c) Phase Image

**Figure 3.6.:** a) Schematic drawing of an AFM-setup driven in tapping mode b) Topographic image of a C8-BTBT thick-film showing an island c) Phase image of the same island indicating the substrate (bright area).

## 3.3. Polarizing light microscopy

Next to differential scanning calorimetry and x-ray investigations, polarizing light microscopy has become the most important method when it comes to characterize the mesophases (see sec. 1.2) of thermotropic liquid crystals. This is mainly due to the fact that those phases often exhibit optical anisotropy. It allows determination of phase transition temperatures as well as evaluation of the structure.

Whilst the refractive index of isotropic liquid is independent on the orientation and direction of the incident light beam, most LC's phases exhibit some kind of anisotropy which introduces a dependence of the refractive index on light propagation. Speaking about C8-BTBT and the SmA-phase, we may note that the refractive index parallel to the optical axis $\mathbf{n}_\parallel$(i.e. the long molecular axis) is larger than the normal component $\mathbf{n}_\perp$. Materials which fulfil the criteria $\Delta\mathbf{n} = \mathbf{n}_\parallel - \mathbf{n}_\perp > 0$ are called optically positive, a behaviour shared by most liquid crystal phases.

Once a LC is hit by an light beam, this incident beam gets split into two components. One following Snells law:

$$n_1 \sin\theta_1 = n_2 \sin\theta_2 \tag{3.21}$$

the so called ordinary ray and an extraordinary ray which is polarized perpendicular to the ordinary ray. As an effect, those waves travel with different speed as they experience different indices of refraction $\mathbf{n_o}$ and $\mathbf{n_e}$. This ends up in a phase difference

$$\delta = \frac{2\pi}{\lambda}(\mathbf{n_e} - \mathbf{n_o})\mathbf{d} \tag{3.22}$$

where d marks the distance travelled within the medium and $\lambda$ the vacuum wavelength. Getting back to the SmA phase, it is possible to relate the indices mentioned above via

$$\mathbf{n_o} = \mathbf{n_\perp} \tag{3.23}$$

$$\mathbf{n_e} = \frac{\mathbf{n_\parallel}\mathbf{n_\perp}}{\sqrt{\mathbf{n_\parallel}^2 \cos^2\phi + \mathbf{n_\perp}^2 \sin^2\phi}} \tag{3.24}$$

where $\phi$ marks the angle between optical axis $\mathbf{n_\parallel}$ and light direction. To sum up, the initially linearly polarized light becomes elliptically polarized with one component being able to pass through the medium and thus, the sample appears bright with an intensity $I$, depending on the position of the polarisers:

$$I = I_0 \sin^2 2\psi \sin^2 \frac{\delta}{2} \tag{3.25}$$

whereas the second term is in fact responsible for the colors that can be observed for several liquid crystals, often called *Schlieren-* or *fan-shaped*-texture (see fig. 3.7). $\psi$ marks the azimuthal angle between the analyser and the projection of the optic axis into the sample plane (Dierking, 2004). It might be noted that the determination
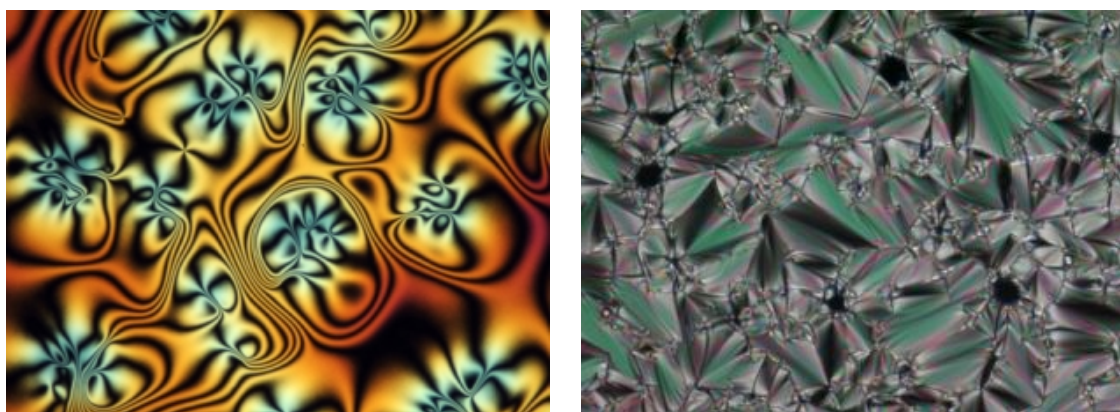


(a) Nematic Schlieren texture        (b) fan-shaped SmA -texture

**Figure 3.7.:** Polarizing light pictures of a) a nematic and b) a SmA liquid crystal according to Starkulla et al. (2009) and microscopy.com-website (2012).

whether a LC is optically postitive or not is done by a slight different approach of optical microcsopy, namely conoscopy (Van Horn and Winter, 2001) (Madsen et al., 2004).

For our purposes, polarizing light microscopy was driven in reflective mode rather than transmission mode. Still, the SmA and crystalline phase can be distinguished by rotation of the polarisers.

# 4. Experimental Setup

## 4.1. PANalytical-Empyrean

Because of the good collimation of the primary beam at low incident angles $\alpha_i$, the PANalytical Empyrean System provides an excellent setup to perform x-ray reflectivity experiments. Basically it is a common 2 circle diffractometer consisting of the following components:

- **Primary side:** CuK$_\alpha$ copper x-ray tube emitting a wavelength of $\lambda_{CuK_\alpha}$=0.154179 nm. The divergent beam is collimated by a multilayer mirror which is located directly in front of the tube (divergence = 0.04°). Two slots allow to define beam width and height. For XRR, a 1/32°divergence slit and a 4 mm beam mask has been used. Finally, a programmable attenuator must be mounted in order to prevent radiation damage of the detector.

- **Sample stage:** The 3-axis cradle allows to move the stage in 1 direction (z) and to rotate the sample along a horizontal axis $\chi$ and a vertical axis $\phi$. Therefore it is possible to e.g. perform preferred orientation (texture) and residual stress analysis using the $\chi$-tilt method.

- **Secondary side:** The diffracted beam is detected by the PIXcel$^{3D}$-detector, that can be operated in different modes (0D, 1D and 2D) and is driven in a so called 1D-receiving slit mode for x-ray reflectivity measurements. Additionally a horizontal 0.1 mm slit is fixed in front of the detector. This slit allows to define the $\theta$-resolution. With a vertical soller slit it is possible to decrease the amount of diffuse or air scattering detected.

PANalytical provides several software packages for collecting, manipulating and analysing the measured data:

- **Data Collector:** Central control module for all XRD measuring routines.

- **Data Viewer:** Software for XRD data inspection, conversion and reporting.

- **X'Pert Reflectivity (v1.3):** The main software for simulating and fitting reflectivity data. It is based on the Parrat-formalism regarding reflectivity(see sec. 3.1.2). Roughness is estimated via the approach of Croce and Névot (1976),(Dane et al., 1998).

Fig. 4.1 shows a picture of the components mentioned above. As can be seen, the primary and secondary side are moved up simultaneously in order to keep the specular condition throughout the whole XRR-measurement. The sample stage is not tilted at any time and therefore allows to investigate liquid materials. Next to XRR in a low angular range of $2\theta$ from 0° to 10°, its possible to perform specular x-ray diffraction (XRD)-scans due to the fact, that the scattering vector **q** is always oriented perpendicular to the surface.
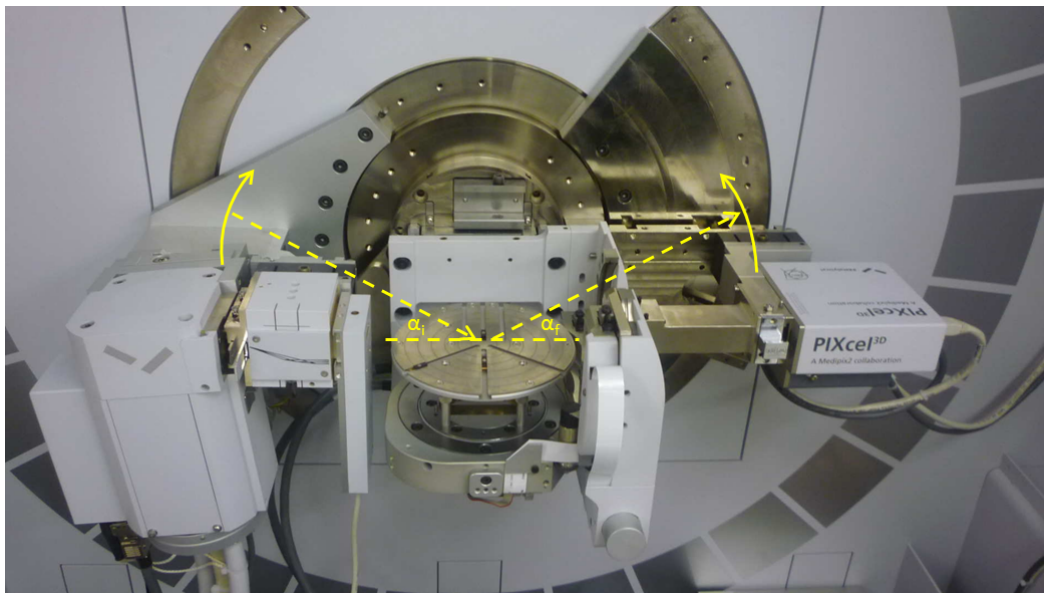


**Figure 4.1.:** Picture of the Panalytical Empyrean setup. The yellow arrows indicate the movement of the components whilst performing a x-ray reflectivity measurement.

## 4.2. Bruker D8 Discover

Due to the usual low intensities that have to be dealt in grazing incidence x-ray measurements, most of experiments are performed at a synchrotron. However, according to Neuschitzer et al. (2012), a GIXD setup using laboratory equipment has been established, proving a possibility to pre-characterize in-plane structure of thin films which in return allows to optimize measurements at a synchrotron where beam time is usually expensive and thus, limited.

The setup is realised on a 4-circle diffractometer called BRUKER D8 Discover. The commercial version has been upgraded with the so called Ultra-GID addon, that allows rotation of the primary side, i.e. the x-ray tube, and consists of the following components:

- **Primary side:** 2.2 kW copper x-ray tube emitting a wavelength of $\lambda_{CuK_\alpha}$=0.154179 nm. A 60 mm long multilayer mirror, located directly in front of the tube col-

limates and monochromizes the convergent x-ray beam. The reachable out-of-plane divergence is 0.025°and CuK$\beta$ is limited to less than 1% of CuK$\alpha$. With a final Soller-slit, the in-plane divergence is tuned to 0.35°whilst beam height can be adjusted with a vertical slit (1.1 mm in our experimental setup).

- **Sample stage:** The 6-axis eulerian cradle allows to rotate in 2 directions $\phi, \chi$, translation in x,y,z-direction as well as tilting in $\xi$ and $\zeta$ on top. These multitude of alignment parameters is mandatory to align the sample for GID-measurements, which is one of the most challenging procedures of this method.

- **Secondary side:** Next to Soller slits for adjusting the acceptance rate, the diffracted beam is detected with a Vantec-1, 1D PSD detector (Khazins et al., 2004). The resolution is in the range of $\Delta\alpha_f = 0.007°$. In the setup used, the detector was capable of covering an out-of-plane range ($\alpha_f$) of 7.3°in one single shot.

As stated in chapter 3.1.1, the incidence angle $\alpha_i$ used for GID-measurements is in the range of the critical angle $\alpha_c$ of the investigated film. $\alpha_i$ is adjusted by rotating the primary side.

Due to the low diffracted intensities, integration times must be rather long. Neuschitzer et al. (2012) estimated the difference of the integration time needed to gain qualitatively equal results to synchrotron measurements and stated of number of 1:50[1].

Following software packages have been used for data collection and processing:

- **XRD Commander:** Central control module for all XRD measuring and alignment procedures of the BRUKER D8 discover. (provided by Bruker).

- **PyGID:** Python based software package developed by A.Moser (2011). It provides compatible interfaces for several different measurement-file formats (*.raw files from BRUKER, HASYLAB-files,...). Its provides numerous feature to visualize and and analyse reciprocal spacemaps. Indeed, all spacemaps within this thesis have been created with PyGID.

Fig. 4.2 shows a picture of the GID-setup including a schematic representation of a measurement where the secondary side is moved around the sample in order to record the reciprocal spacemap.

---

[1]Evaluated by comparing results of pentacene thin films
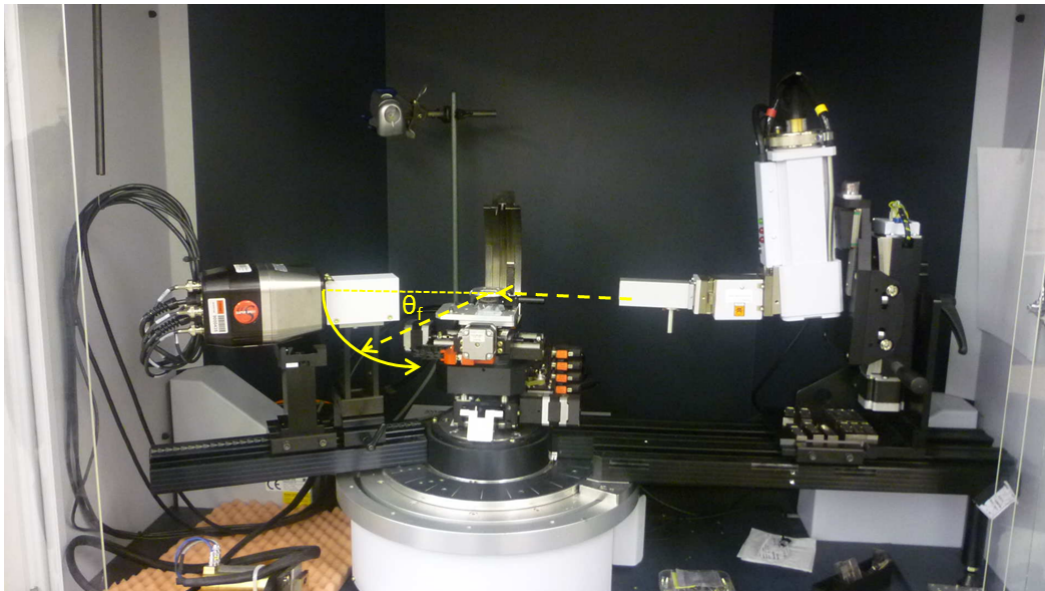
**Figure 4.2.:** Picture of the BRUKER D8 setup for grazing incidence diffraction. The yellow arrows indicate the x-ray beam and movement of the components whilst measuring a reciprocal spacemap.

## 4.3. HASYLAB- Beamline W1

The beamline W1 is one out of 38 instruments for photon research at the HASY-LAB in Hamburg, Germany. Located at the DORIS III storage ring, it allows x-ray diffraction and scattering experiments at an energy range of 4-11 keV. Energies can be adjusted by a double crystal Si(111) monochromator (HASYLAB-website, 2012).

For our purposes, specular and grazing incidence experiments have been performed on the heavy-load 6+2 circle diffractometer. The beam size can be tuned by vertical and horizontal mountable slits on the primary side of the setup. Samples are placed on an Eulerian cradle that allows to install different stages including a *DHS 900* heating stage for temperature dependent, in-situ measurements (see sec 4.4). On the secondary side, the beam passes through an evacuated flight tube before it is detected by a 1D-Mython position sensitive detector (PSD). Next to the reduction of air-scattering, the adjustable size of the fly-tube's entry slit allows to set resolution. Fig. 4.3(a) illustrates the setup of the beamline W1.
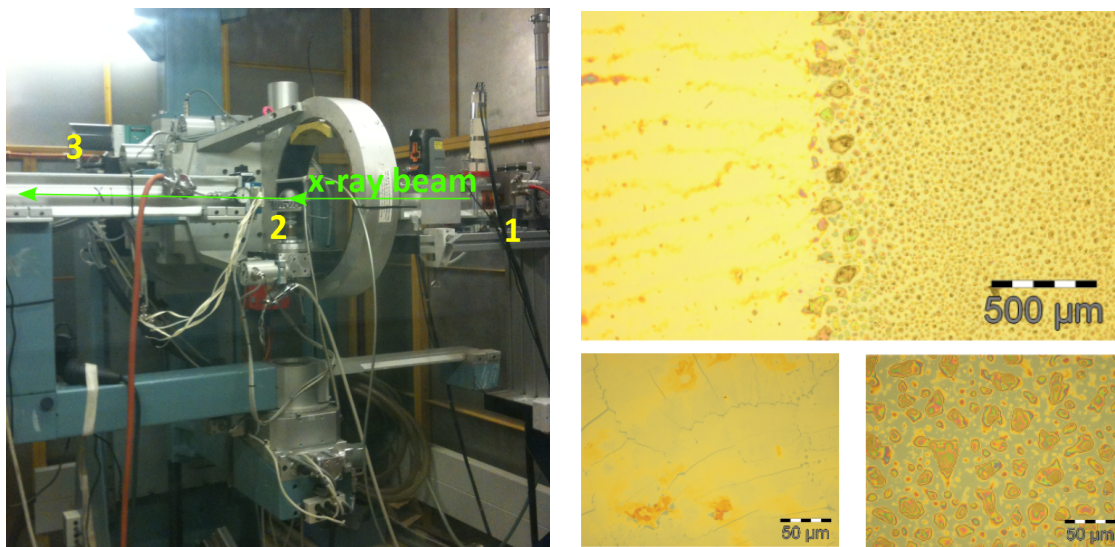


(a) 1) Beam entrance and slit-system 2) sample (b) Thick film after synchrotron experiments. stage with DHS mounted 3) fly-tube and detector Left: out of-beam, right: in-beam morphology

**Figure 4.3.:** a) Picture of the W1-beamline at HASYLAB and b) optical microscopy demonstrating the influence of the radiation on the film morphology

### 4.3.1. Radiation damage

Due to the high energy densities gained at a synchrotron, beam damage is an important and non-negligible factor when it comes to investigate organic thin films (Neuhold A., 2011). As can be seen in fig. 4.3(b), there is a huge difference in the morphology of the thin film between areas that have been hit/not hit by the x-ray

beam. It seems as if the energy placed results in dewetting of the thin film. This is equal to the placement of thermal energy during our heating experiments (see chapters 6 and 5).

## 4.4. DHS 900 Heating stage

The DHS 900 heating stage allows to perform high temperature in-situ x-ray studies of thin films. It can be mounted on most eulerian cradles and XYZ stages and therefore be operated on synchrotrons as well as commercial x-ray diffractometers.
A temperature range from 25-900°C is covered and can be controlled with an accuracy of 1°C. Next to this, the x-ray transparent plastic dome (PEEK) allows to establish low vacuum, nitrogen or inert atmosphere (Anton Paar GmbH - website, 2012),(Resel et al., 2003).

## 4.5. Atomic Force Microscope

Atomic force microscopy was performed on an *AsylumResearch MFP-3D$^{TM}$ Stand Alone AFM* at the Montan University in Leoben. In order to observe high temperature phases, the *AsylumResearch PolyHeater$^{TM}$* heating stage, a metal stage embedded in ceramic and high performance plastic, was used. It is capable of heating up to 300°C by providing a special high-temperature cantilever holder (PEEK$^{TM}$) for measurements above 205°C. According to the manufacturer, the sample temperature can be maintained to better than 0.2°C precision with accuracy to 0.5°C (AsylumResearch Homepage,2012).
Following software packages have been used for data collection and processing (including visualization, masking and height analysis):

- **ARgyle:** OpenGL 3D rendering technology provided by AsylumResearch. Among other features, it allows to generate, display and visualize 3D images whilst scanning as well as off-line processing. All common file types are supported.

- **Gwyddion 2.26:** Modular open-source scanning probe microscope data visualization and analysis tool (Necas and Klapetek, 2012).To minimize lateral forces between tip and surface and to consequently avoid sample damage, tapping mode was used.
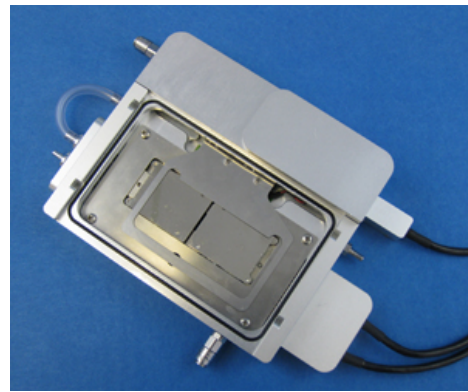
## 4.6. Optical Microscope

Temperature dependent optical microscopy was performed on a *Nikon Eclipse 80i*-microcscope with a *Linkam GS 350* heating stage. It consists of two separate heating elements that can be controlled from -196°C (active liquid nitrogen cooling system) to 350°C with an accuracy of 0.1°C. This e.g. allows to set up temperature gradients. Furthermore, it is possible to control the position and the speed of sample movement

between the two elements with a step motor. In return, this enables to e.g. determine speed of crystal growth or to observe the crystallization front by keeping it in the observed area (LinKam-website, 2012). Fig. 4.4(b) shows a picture of the stage and its components.

At the Graz University of Technology (TUGraz), polarizing light microscopy has been performed on an *Olympus BX 51* microscope that allows measurements in reflection as well as transmission geometry.
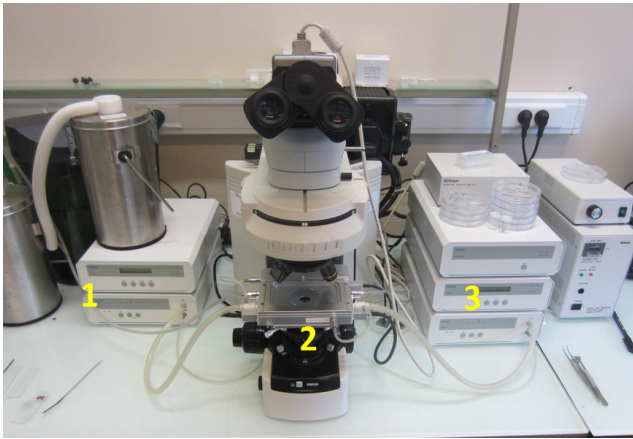


(a) Nikon Eclipse 80i with heating stage mounted      (b) GS 350 heating stage

**Figure 4.4.:** a) Picture of the setup for optical microscopy in Brussels (1,3)-heat control for left and right heating unit (2) Nikon Eclipse 801 with heating stage mounted b) GS 350 heating stage showing the two separately controllable heating units.

# 5. Thin film as $f(T)$

Thin films of semiconducting materials are the key elements in organic devices. Due to the fact that physical properties and therefore device performance is highly dependent on the crystallographic structure and morphology, thin films consisting of a nominal monolayer have been produced by spin-coating a 0.33 mg/ml solution.(see sec. 2). Subsequent investigations have been performed by the means of x-ray-diffraction as well as atomic force- and optical microscopy.
Starting with the morphology and structure after fabrication, the films have been annealed up to 115°C. This chapter provides a walk-through of the temperature dependent behaviour and effects observed during the thermal treatment of the samples.

## 5.1. Initial state

Due to the GID-measurements performed on the thin film, we basically expected the structure (see fig. 1.8) to be equal to the single crystal structure (SCS) published by Takafumi Izawa (2008). However, AFM as well as XRR measurements performed immediately after preparation show that the layer thickness is less than the 2.9 nm, as would be expected from the SCS. According to the AFM pictures captured, the thickness is actually found to be in the range of $d_{initial}$= 2.1 - 2.5 nm (see fig. 5.1).

Searching for an explanation for this decreased layer thickness, we may note two possible reasons:

1. It is likely that the lower alkyl chains are underlying hydrophobic interactions with the also hydrophobic substrate surface. This leads to a repulsive reaction of the alkyl chain. Thus, it is likely that the lower alkyl chains are pointing away from the substrate (see fig. 5.2(b).

2. The differences observed could also be pointed to the fabrication process. As stated in sec. 2.3, spin-coating is a process far off equilibrium leading to disorder after film fabrication.

By applying a respective disordered fitting-model, we found good agreement by the means of XRR (fig. 5.2). Due to this result, it can be assumed that the layer is probably disordered. Basically, it should be possible to confirm this by performing grazing incidence diffraction. However, the immediate formation of a dendritic structure competes with the time needed for GID-measurements, especially for aligning the sample. As we will see later, this unstable disordered state after spin-coating is the only structure observed, that is not equal to the **SCS**.
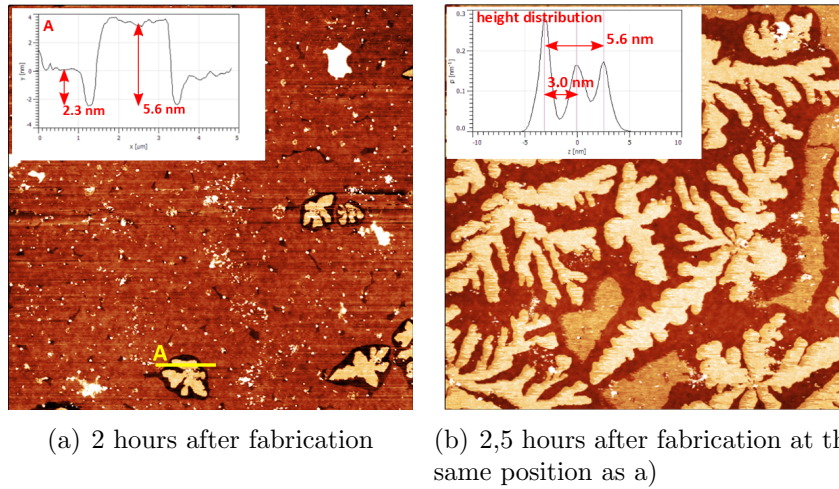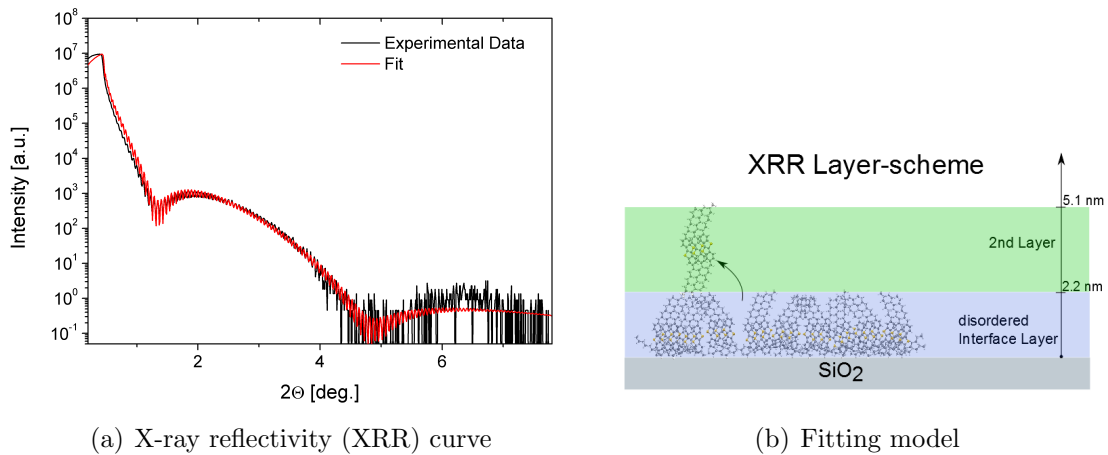
(a) 2 hours after fabrication

(b) 2,5 hours after fabrication at the same position as a)

**Figure 5.1.:** Atomic force microscope image of the thin film a)2 hours and b) 3 hours after fabrication. Next to the disordered $d \approx 2,3nm$ thick layer, the onset of dendritic bi-layer growth can be seen.



(a) X-ray reflectivity (XRR) curve

(b) Fitting model

| Layer | $d$ / $nm$ | $\rho$ / $g/cm^3$ | $\sigma$ / $nm$ |
|---|---|---|---|
| **Disordered interface layer** | | | |
| lower alkyl chain | 0.600 | 0.60 | 0.5 |
| molecule core | 0.875 | 1.86 | 1 - 1.5 |
| upper alkyl chain | 1.010 | 1.00 | 0.5 |

(c) Fit parameters

**Figure 5.2.:** X-ray reflectivity (XRR) of the thick film at room temperature after spin-coating. a) Reflectivity curve compared with fitted data b) Schematic drawing of the fitting model consisting of a disordered layer in agreement with AFM-data (see fig. 5.1) c) Fitting parameters (d = thickness, $\rho$ = density, $\sigma$ = roughness).

## 5.2. Formation of a dendritic bilayer - Dewetting

As shown in the previous chapter, the disordered thin film morphology after fabrication is governed by a dewetting process leading to a rapid formation of dendritic islands covering 50-60% of the sample surface within 3-5 hours (see fig.5.3(b)).

By performing AFM experiments, the thickness of the dendrites was found to be $d_{bilayer}$=5.6 nm (see fig.5.3(a)). This would actually be a bi-layer structure with both layers obtaining **SCS**. To confirm this result, XRR has been carried out and fitted with a two-layer model as can be seen in fig. 5.4. There is very good agreement of the fitted data with the experimental curve. It turns out, that this structure is very stable at room temperature as there are only slight changes in the morphology when storing samples in ambient atmosphere for months. Still, there is a slight ongoing dewetting process, leading to small crystallites with a height of 3 layers over long periods of time (see appendix B).

Dendritic shapes are often an indicator for the underlying process to be ruled by diffusion limited aggregation (DLA). This means that the molecules move freely along the substrate but get stuck once they get in touch with an aggregate consisting of several molecules. However, due to the nature of DLA, in most cases, like pentacene, the dendritic shape appears in each layer (Meyer zu Heringdorf et al., 2001). In case of C8-BTBT, the dendritic structure seems to be a property of the "bi-layer" only (see appendix A ).
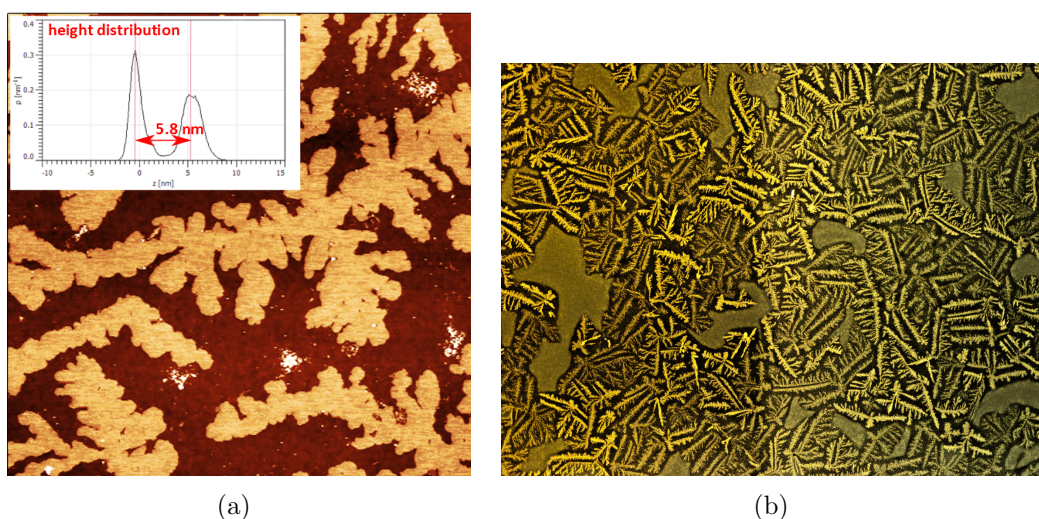


(a)          (b)

**Figure 5.3.:** Thin film investigated more than 5 hours after fabrication. The dendritic structure can nicely be observed with both a) atomic force microscopy and b) optical microscopy (partially the disordered monolayer can still be seen in between).
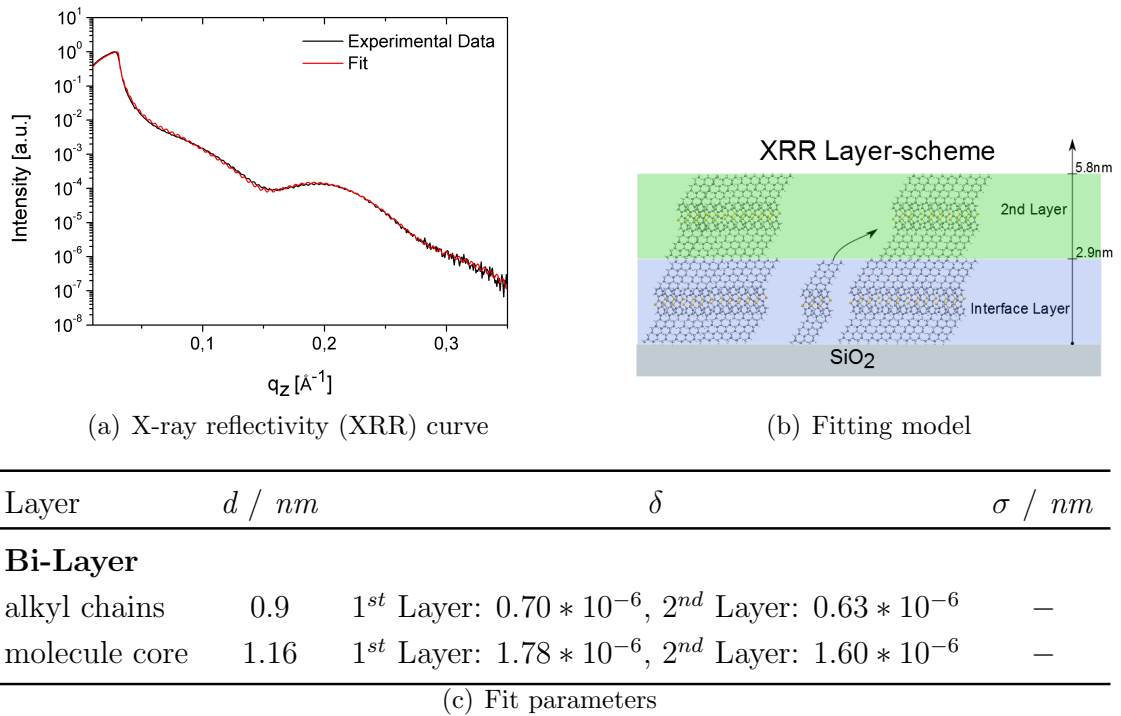
(a) X-ray reflectivity (XRR) curve



(b) Fitting model

| Layer | $d$ / $nm$ | $\delta$ | $\sigma$ / $nm$ |
|---|---|---|---|
| **Bi-Layer** | | | |
| alkyl chains | 0.9 | $1^{st}$ Layer: $0.70 * 10^{-6}$, $2^{nd}$ Layer: $0.63 * 10^{-6}$ | – |
| molecule core | 1.16 | $1^{st}$ Layer: $1.78 * 10^{-6}$, $2^{nd}$ Layer: $1.60 * 10^{-6}$ | – |

(c) Fit parameters

**Figure 5.4.:** X-ray reflectivity (XRR) of the thick film at room temperature 4 hours after spin-coating, stored at ambient atmosphere. a) Reflectivity curve compared with fitted data b) Schematic drawing of the fitting model consisting of two ordered layers in agreement with AFM data (see fig. 5.3(a)) c) Fitting parameters (d = thickness, $\rho$ = density, $\sigma$ = roughness). Whilst fitting, the upper and lower alkyl chains have been set to be equal according to the SCS.

## 5.3. Annealing effects

Starting with the bi-layer structure described in the previous chapter, annealing experiments have been performed. The sample was heated up to 115°C and therefore into the smectic phase of C8-BTBT.
The effects observed can be separated into two different regimes:

1. RT - 90°C: **Dewetting** leading to formation of crystallites.

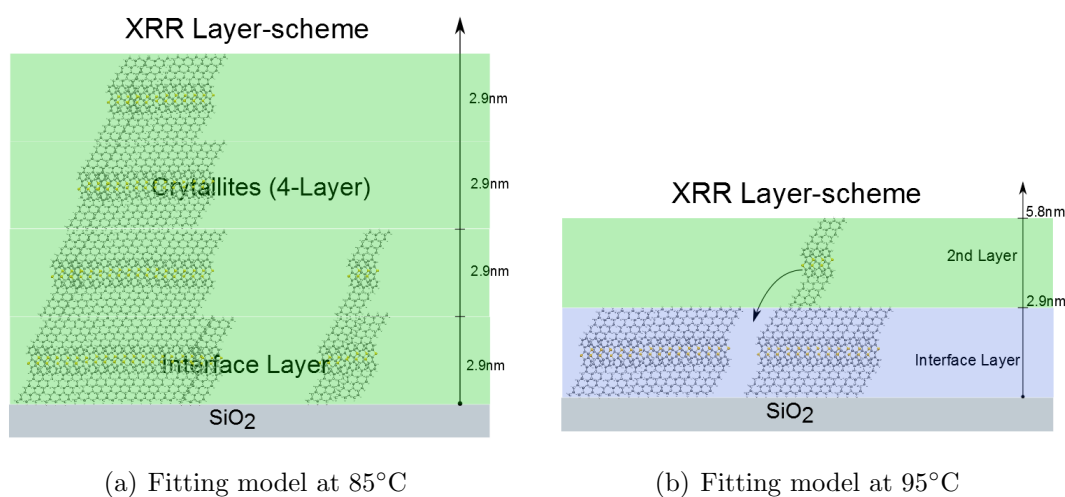2. >90°C: **Wetting** leading to re-formation of a monolayer.



(a) Fitting model at 85°C

(b) Fitting model at 95°C

**Figure 5.5.:** Schematic drawing of the film structure/ fitting model at a) 85°C and b) 95°C.

Starting with the regime dominated by the formation of crystallites, optical microscopy reveals that the responsible dewetting process is, as expected, accelerated by the deposition of thermal energy. Comparing fig. 5.12(a) - 5.12(b) the dependence on the heating rate applied. It turns out that whilst heating up to 90°C the process is rather slow but crystallite formation is quick keeping the temperature at 90°C for a couple of minutes. XRR has been performed at 85°C. Due to the time needed to perform a measurement and the time-scales observed by optical microscopy, we assume that crystallite formation is completed once alignment is finished. Fig. 5.6 illustrates the fitting model applied. The result can be seen in fig 5.6 showing good agreement with the experimental data. The decreasing density with crystal height is represented by the decreasing $\delta$-values in fig. 5.6(b).

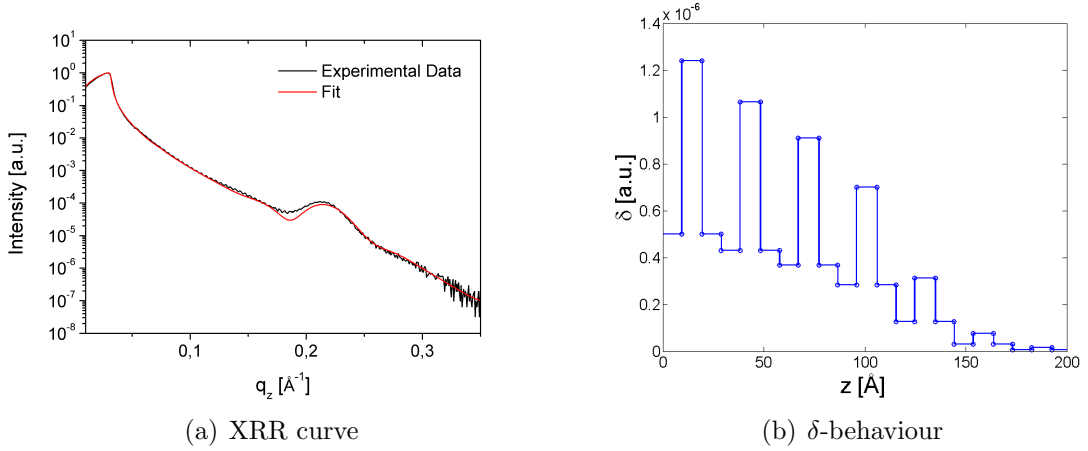Increasing the temperature above 90°C, we enter the regime dominated by a wetting

(a) XRR curve  (b) $\delta$-behaviour

**Figure 5.6.:** X-ray reflectivity (XRR) of the thick film at 85°C. a) Reflectivity curve compared with fitted data b) $\delta$-behaviour along the z-direction indicating a decreasing density as the crystallite grows.

effect that leads to melting of the newly formed crystallites and formation of a closed layer on the surface (fig. 5.12(d) and 5.12(e)). Once exceeding 100°C, the crystallites are no longer observable by the means of optical microscopy. XRR performed at 95°C confirms the interpretation of the wetting process. Using a fitting model, consisting of a nearly filled layer on the substrate surface with small crystallites still present, good agreement with the experimental is achieved (see fig.5.7). The "*filled*" layer's electron density is reflected by $\delta_{alkyl} = 1.1 * 10^{-6}$ and $\delta_{core} = 2.5 * 10^{-6}$. Comparing fig. 5.6(b) and 5.7(b) we can see the difference between the $\delta$-values representing the melting crystallites.

Interestingly, the moment where wetting occurs is equal to the moment where in-plane order is no longer observable by GID-measurements. This indicates that the wetting process is actually happening in the smectic phase of the thin film. The transition temperature seems to be lower than the phase transition temperature $T_{trans}$=110°C of the bulk as shown in chapter 1.3.1. Probably this is due to the fact that the DSC has been performed on the bulk and it is known that transition temperatures are different depending on the amount of material available or presence of interfaces nearby. Therefore, we can ascribe the crossover from dewetting to wetting to a difference in surface tension of the crystalline and the smectic state (Benichou et al., 2003). The dewetting process has also been investigated by the group of Liu et al. (2010). Their primary goal was to investigate the ability to grow C8-BTBT single crystals by solvent vapour annealing (SVA). We may note that our results are in good agreement with their findings.

Next to the dewetting/wetting process, thermal expansion of the unit cell as well as the phase transition from the crystalline to the smectic SmA-phase has been analysed by grazing incidence diffraction. For comparison with the more bulk like thick film, the results are listed in chapter 6.3 and 6.4.
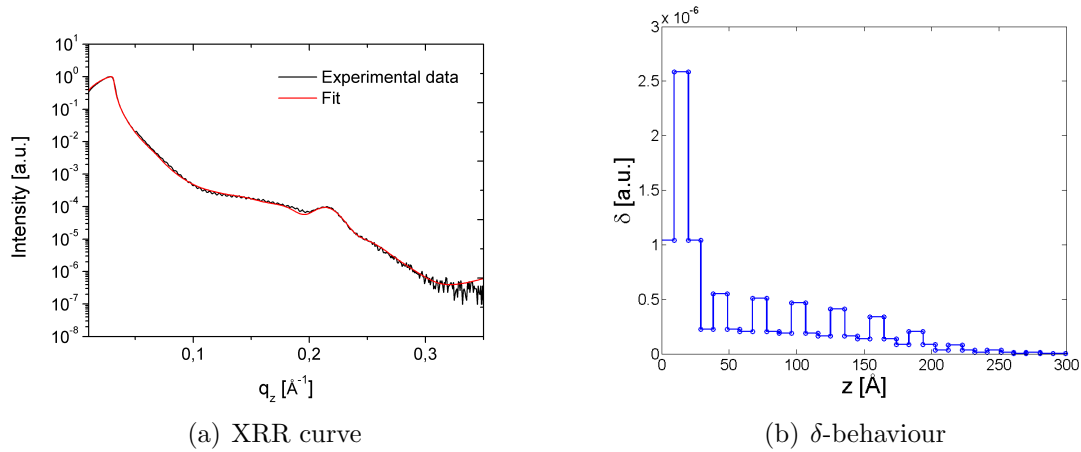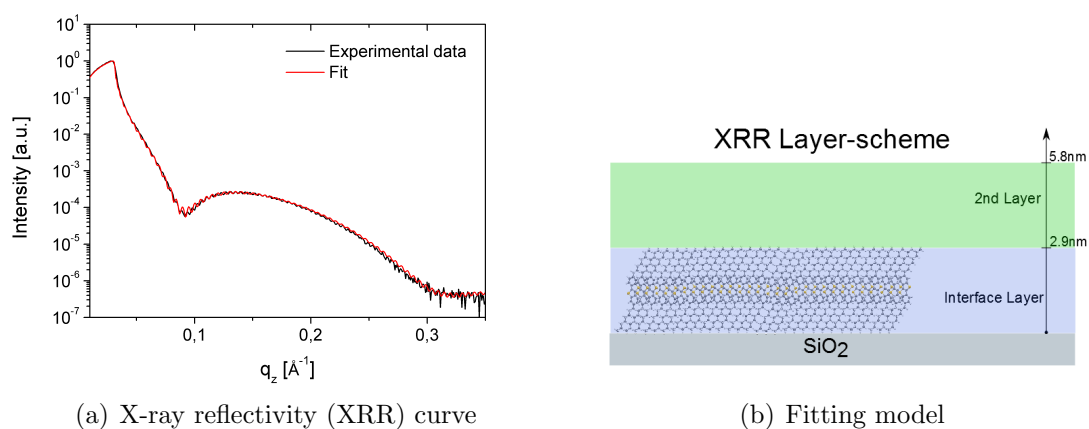


(a) XRR curve

(b) $\delta$-behaviour

**Figure 5.7.:** X-ray reflectivity (XRR) of the thick film at 95°C. a) Reflectivity curve compared with fitted data b) $\delta$-behaviour along the z-direction indicating formation of a filled layer at the interface and slightly decreasing density as the crystallite grows.

## 5.4. Post-Annealing

In order to investigate the film structure that has been established after cooling from the liquid crystalline phase, the annealed samples have been cooled to room temperature at natural cooling rate. Applying a fit model consisting of a single monolayer with **SCS** shows very good agreement with the measured XRR-curve (see fig. 5.8). For confirmation, AFM and optical microscopy has been performed. Whilst fig. 5.12(f) approves the XRR results, partial re-occurrence of the dendritic bi-layer structure was found when performing AFM-measurements (see 5.9). As mentioned in chapter 5.2, there is a slow dewetting process present at room temperature. Therefore the re-occurring bilayer is probably an AFM measurement artefact resulting from the placement of thermal energy by the laser that is hitting the cantilever. To investigate the stability of the monolayer, XRR measurements have been performed at different times after cooling the sample. The result can be seen in fig. 5.10. The decreasing minima represent the layer getting less filled due to the dewetting process mentioned above. Still, in contrast to the disordered monolayer observed after spin-coating, the newly formed monolayer shows increased stability and does not undergo the spontaneous dewetting to the dendritic structure at room temperature.



(a) X-ray reflectivity (XRR) curve

(b) Fitting model

| Layer | $d$ / $nm$ | $\delta$ | $\sigma$ / $nm$ |
|---|---|---|---|
| **Re-established monolayer** | | | |
| alkyl chains | 0.76 | $1.32 * 10^{-6}$ | – |
| molecule core | 1.40 | $3,36 * 10^{-6}$ | – |

(c) Fit parameters

**Figure 5.8.:** X-ray reflectivity (XRR) of the thick film at room temperature after annealing to 115°C. a) Reflectivity curve compared with fitted data b) Schematic drawing of the fitting model consisting of a single ordered layer c) Fitting parameters (d = thickness, $\rho$ = density, $\sigma$ = roughness)
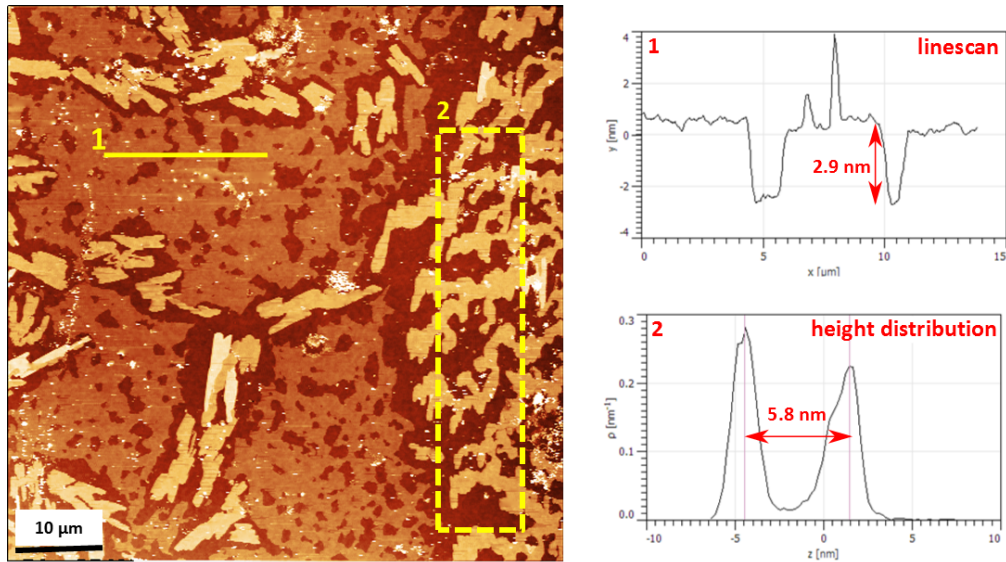
**Figure 5.9.:** AFM image of the thin film 1 hour after annealing showing both 1) a monolayer and 2) re-occurence of the bilayer state
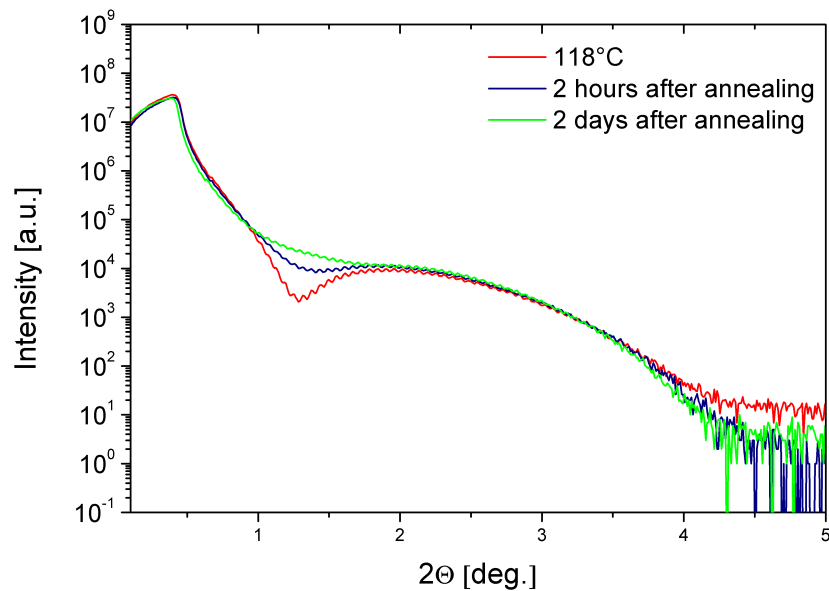


**Figure 5.10.:** X-ray reflectivity curve of the thin film after cooling from the smectic phase at different times indicating the increased stability of the newly formed monolayer.

## 5.5. Conclusion

To sum up, fig 5.11 shows the behaviour of the *C8-BTBT* thin film as a function of temperature investigated by the means of x-ray-reflectivity. Starting from a dendritic bi-layer that is formed by a dewetting process at room temperature, it can be seen, that up to 90°C, crystallite formation leads to the raise of the (001)-Bragg-reflex at $\mathbf{q_z} \approx 0,21$. This indicates the amplifying influence of temperature on the dewetting behaviour. Exceeding 90°C, material transport is reverted, and a monolayer obtaining SCS is established. Final microscope and XRR measurements reveal that the layer formed in the smectic phase is stable at room temperature for several days and does not undergo immediate dewetting again.
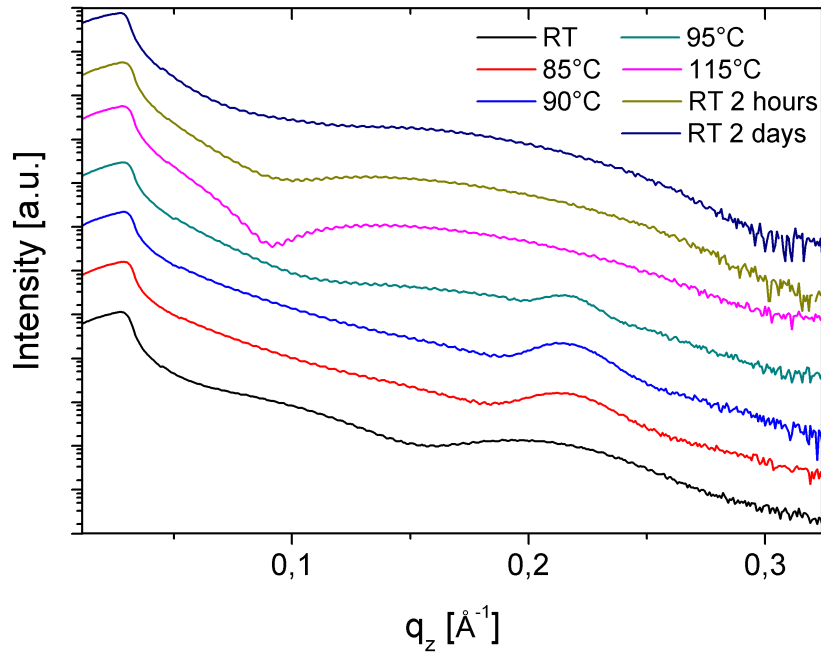


**Figure 5.11.:** Temperature behaviour of the thin film, investigated by x-ray-reflectivity.

Thermal expansion of the thin-film unit cell as well as phase transition of the thin film are explained in chapter 6.3 and 6.4.
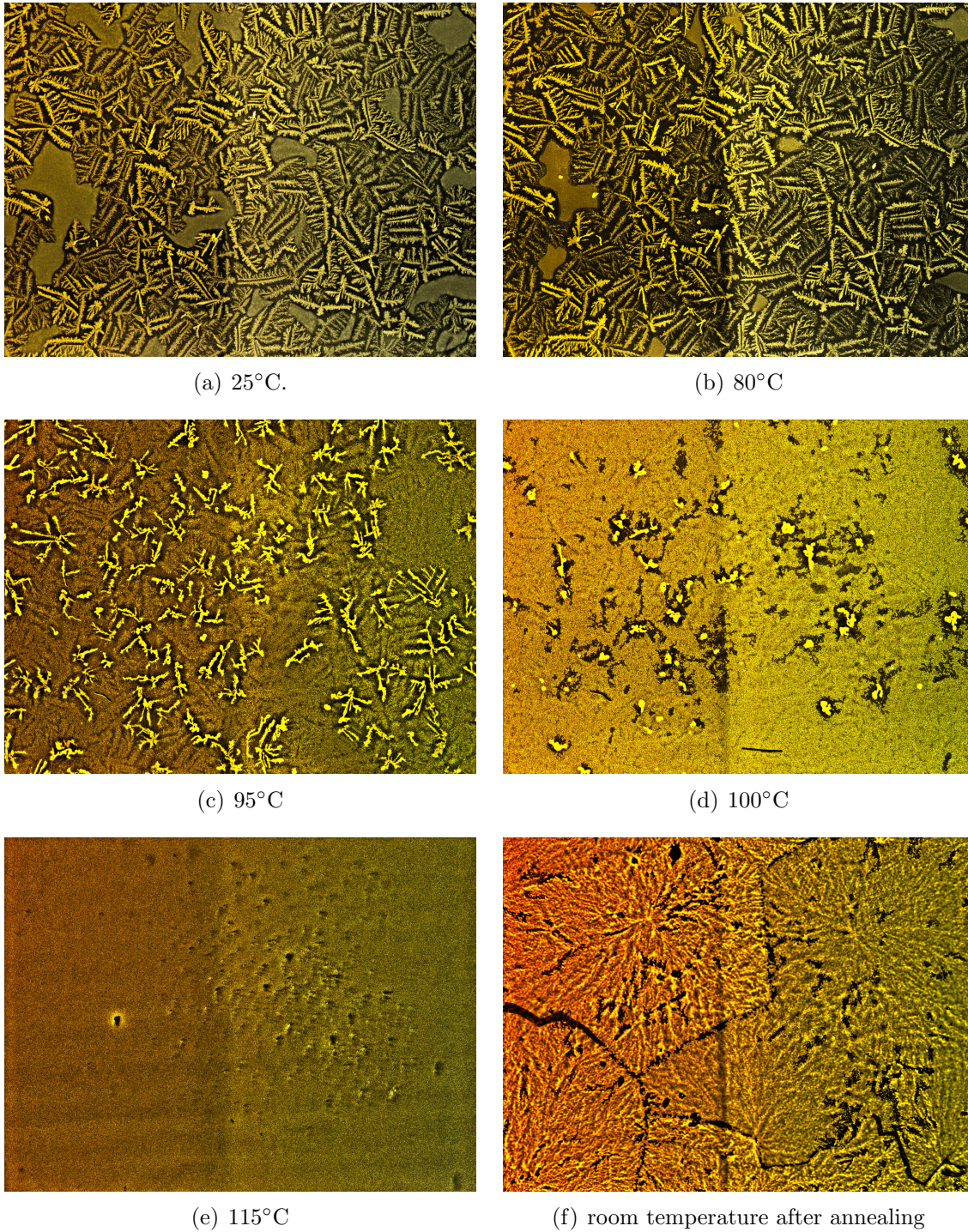
(a) 25°C.

(b) 80°C

(c) 95°C

(d) 100°C

(e) 115°C

(f) room temperature after annealing

**Figure 5.12.:** Surface morphology of the thin film at different temperatures observed by optical microscopy. The pictures have been digitally modified for illustration purposes.

# 6. Thick film as $f(T)$

In the previous chapter, the temperature dependent behaviour of ultra-thin films of C8-BTBT was shown. In order to investigate the more bulk-like properties, films with a nominal thickness of up to $d_{thickfilm}$=100 nm have been produced by drop-casting or spin-coating a 10.4 mg/ml solution on silicon oxide wafers (see chapter 2).
Within the next chapters, a detailed analysis of the thick film and the observed effects is presented. Starting at room temperature, the samples were heated up to the isotropic phase at 130°C, crossing the smectic phase in the temperature range between 110°C and 125°C.

To give a brief overview, the phenomenons observed and analyzed are:

- **Dewetting/Wetting** and formation of crystallites

- **Thermal expansion** of the unit cell during heating up to the smectic phase

- **Phase transition** from Crystalline via Smectic to the Isotropic state and vice versa

- **Smectic layering**: Defined layer-by-layer formation once reaching the smectic phase

- **Quenching/cooling effects**

As for the thin film, XRR and GID-results have been verified by the means of atomic force- and optical microsocopy. For comparison, chapter 6.3 (thermal expansion) and chapter 6.4 (phase transition) contain results for both, the thick and the ultra thin film.

## 6.1. Initial state

According to the grazing incidence x-ray diffraction (GIXD) measurements on drop-casted and spin-coated thick films (see fig. 1.8), the thick film consists of multiple layers with single crystal structure (scs) (Takafumi Izawa, 2008). AFM images taken by the group of C. Teichert at the Montan University of Leoben reveal that immediately after spin-coating, islands with en exponential decay of the layer area, marked by the green dashed line in fig.6.3(a), are formed. The formation of terraced growth mounds often indicates the presence of an energy barrier at the step edges of the islands leading to a repulsive force on the molecule once trying to cross the step edge. Thus, the molecule gets reflected when attempting to fill the layer and therefore participates in the nucleation of the second layer way before the initial layer closes. This repulsive barrier is called Ehrlich-Schwoebel barrier(ESB). As a prominent example we could mention para-sexiphenly (6P), another small molecule. The growth dynamic and formation of islands has been well explained by taking the ESB into account in this system(Hlawacek et al., 2008).



(a) X-ray reflectivity (XRR) curve

(b) Fitting model
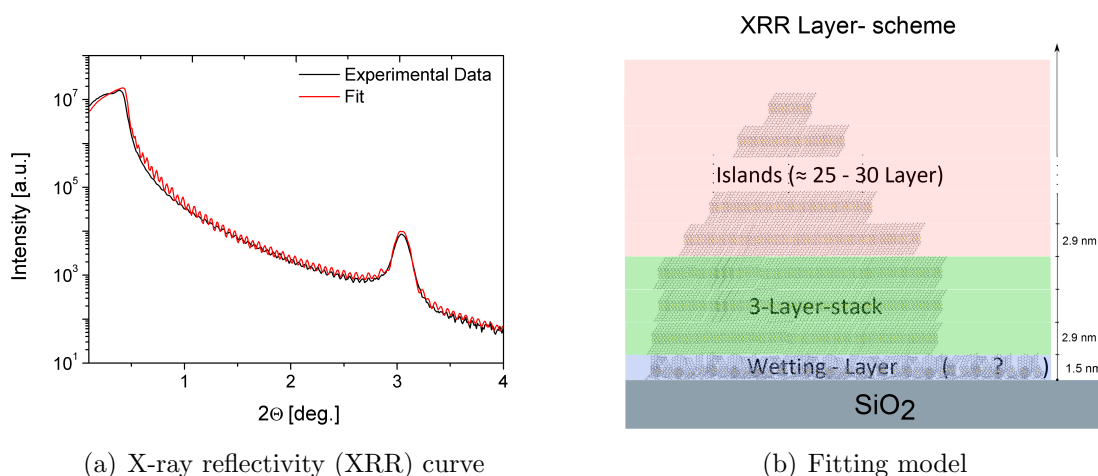
| Layer | $d$ / $nm$ | $\rho$ / $g/cm^3$ | $\sigma$ / $nm$ |
|---|---|---|---|
| **Interface Layer** | 0.79 | 0.46 | 0.46 |
| **Islands consisting of 25 layers** | | | |
| molecule core | 0.8750 | $1.186 - 0.1$ (bottom-top $\rho$-fluctuation) | 0 |
| alkyl chains | 1.0125 | $0.800 - 0.1$ (bottom-top $\rho$-fluctuation) | upper: 0.75 |

(c) Fit parameters

**Figure 6.1.:** X-ray reflectivity (XRR) of the thick film at room temperature. a) Reflectivity curve compared with fitted data b) Schematic drawing of the fitting model consisting of islands in agreement with AFM-data (see fig. 6.3(a)) c) Fitting parameters (d = thickness, $\rho$ = density, $\sigma$ = roughness).

By performing XRR, it was found that the islands consist of 25 layers with a total thickness of $d_{thick} \approx 72.5$ nm. The Fitting model and fit - parameters can be seen in fig. 6.1. The fitting model used is based on the AFM results from fig. 6.3(a), consisting of 25 layers with decreasing density to simulate the islands.

### 6.1.1. Wetting Layer

As can be seen in the fitting parameters, an "**interface layer**" was used at the interface between the islands and the substrate. Although it is not really known why this layer is created and what it consists of, some information can be gained of X-ray diffraction experiments:

- The layer is probably disordered as there is no feature appearing in the reciprocal spacemaps indicating an order other than the bulk phase[1].

- Probably, the layer is formed because of the hydrophobic interactions between the alkyl chains and the substrate surface. One possibility would be BTBT-molecules with the molecule core touching the substrate and alkyl chains pointing away because of those repulsive hydrophobic forces (see fig.6.2).

- The layer was experimentally confirmed by XPS/UPS measurements for dihexyl-terthiophene (DH3T), another comparable organic small molecule (Wedl et al., 2012).

- According the XRR fit algorithm, the layer shows a thickness between $d_{Interfacelayer}$= 1 - 1.5 nm. With a density of $\rho = 0.4 - 0.7 g/cm^3$ it is likely that the layer is not covering the whole surface and the molecules within the layer are indeed attending the dewetting process when islands or crystallites are formed[2].

It must be noted, that the layer was mandatory in order to fit XRR-measurements at each temperature for the thick film. Therefore, this layer was introduced with respect to the facts listed above.
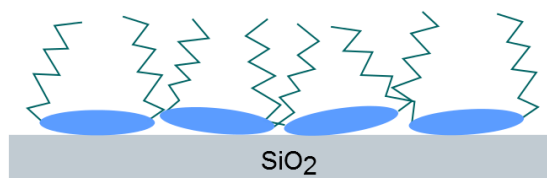


**Figure 6.2.:** Possible formation of the wetting layer: The hydrophobic alkyl chains are pointing away from the hydrophobic substrate surface whilst the molecule core is bound.

---

[1]Due to the interface layer thickness ranging from 0.75 nm up to 1.3 nm, the structure must be different to the bulk structure

[2]In agreement with the results for the thin film, where XRR-measurements could be explained without the need of a wetting layer

## 6.2. Annealing Effects

Starting with the morphology consisting of islands after preparation, the samples have been heated up to the liquid crystal phase. The structure of the film has been investigated by GIXD and XRR at certain temperatures ($\Delta T = 10 - 20°C$). As for the thin film, the effect observed can be divided into two temperature regions.

Up to 100°C, the behaviour of the thick film is actually equal to the thin film. The regime is governed by a dewetting process that leads to a formation of rather huge crystallites with a height up to $\approx$150 nm, representing a system consisting of about 50-70 layers, depending on the time the sample is kept at the high temperatures. Fig.6.4 shows the XRR-curve taken at 90°C and the fitting model applied. As mentioned in the previous chapter, a wetting layer was mandatory to get accurate fitting results. Due to the size of the crystallites and according roughness, it was not possible to perform AFM experiments on the thick film. Instead, an intermediate film, with a nominal thickness of $d_{intermediate}$ =15-20 nm, was used. As can be seen in fig. 6.3(b), dewetting converts the islands into rather huge crystallites. As for the thin film (see chapter 5.3), optical microscopy revealed that the process is rather slow below 80-90°C but once a certain temperature is reached, large crystallites are formed out of smaller ones within a short period of time (see figures 6.21(a) - 6.21(d)).
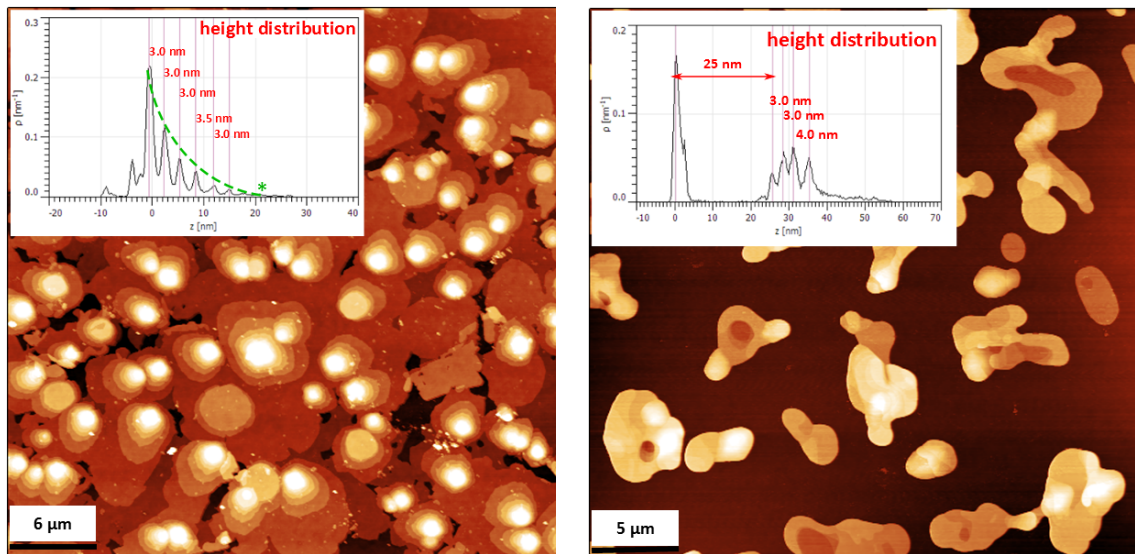


(a) Island morphology at Room temperature          (b) Crystallites at 90°C

**Figure 6.3.:** AFM images of the intermediate film at a) RT after fabrication showing layer-by-layer island growth(green dashed line) and b) at 90°C showing the formation of crystallites.

Exceeding 105°C, we finally get to the regime where material transport is reverted and wetting leads to a formation of uniform, filled layers. In contrast to the thin film, where there is limited amount of material available, we see additional features for the thick film:

- Smectic layering: The wetting process turns out to be a very defined layer-by-layer growth. (see chapter 6.5)

- The onset of layering happens at a temperature of T=105°C. This is 15°C higher than for the thin film, where the layering process already starts at T=90°C (see chapter 5.3). Later on, we will see that the temperature is probably equal to the phase transition temperature $T_{trans}$ from the crystalline to the smectic phase. This indicates that $T_{trans}$ heavily depends on the film thickness. The 100 nm film gets rather close to the bulk-transition temperature of T=110°C.

Before getting to this interesting layering effect, we will focus on the thermal expansion of the unit cell as well as the phase transition and how they can be investigated by the means of x-ray reflectivity and grazing incidence diffraction.



(a) X-ray reflectivity (XRR) curve
(b) Fitting model
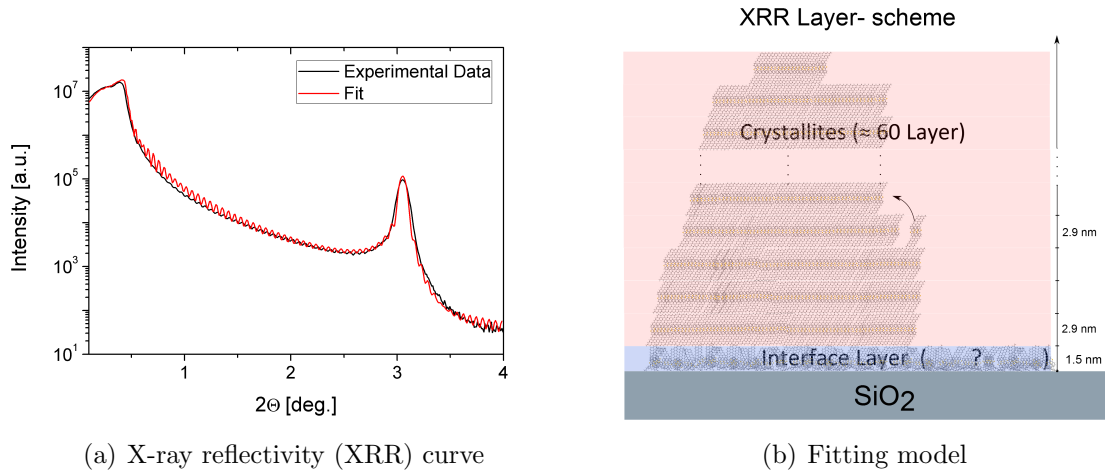
| Layer | $d$ / $nm$ | $\rho$ / $g/cm^3$ | $\sigma$ / $nm$ |
|---|---|---|---|
| **Interface Layer** | 1.3 | 0.58 | 0.1 |
| **Crystallites consisting of 50 layers** | | | |
| molecule core | 0.8750 | $1.58 - 0.30$ (bottom-top $\rho$-fluctuation) | 0 |
| alkyl chains | 1.0125 | $0.70 - 0.32$ (bottom-top $\rho$-fluctuation) | upper: 2.1 |

(c) Fit parameters

**Figure 6.4.:** X-ray reflectivity (XRR) of the thick film at 90°C. a) Reflectivity curve compared with fitted data b) Schematic drawing of the fitting model consisting of islands in agreement with AFM-data (see fig. 6.3(b)) c) Fitting parameters (d = thickness, $\rho$ = density, $\sigma$ = roughness).

## 6.3. Thermal Expansion

As usual, thermal expansion can be observed once an object is heated. In this chapter we will investigate the influence of the temperature on the C8-BTBT unit cell (see chapter 1.3.2). For this purpose, grazing incidence diffraction as well as specular scans have been performed at temperature steps of $\Delta T$=10°C at the beamline W1 at HASYLAB.

The next chapter will give a mathematical introduction and explanation about how to determine the unit cell out of the reciprocal spacemaps. The formulas derived are than applied onto our measurements and finally the results are listed in chapter 6.3.2.

### 6.3.1. Unit cell determination

As described in chapter 3.1.1, we can get the position of $\mathbf{q_{hkl}}$-vectors representing diffractions of certain interlayer distances $d_{hkl}$ out of the reciprocal spacemaps captured by GID-experiments.

The first thing to do is to derive some formula that allow us to evaluate all lattice parameters out of those $\mathbf{q_{hkl}}$ values (Moser, 2012).

By squaring $\mathbf{q}$ we get:

$$\boldsymbol{q_{hkl}}^2 = h^2 a^{*2} + k^2 b^{*2} + l^2 c^{*2} + 2hk a^* b^* \cos\gamma^* + 2hl a^* c^* \cos\beta^* + 2kl b^* c^* \cos\alpha^* \quad (6.1)$$

Building the difference between two squared $\boldsymbol{q}$ vectors gives (6.2)

$$(\boldsymbol{q}^2_{h_2 k_2 l_2} - \mathbf{q}^2_{h_1 k_1 l_1}) = (h_2^2 - h_1^2)a^{*2} + (k_2^2 - k_1^2)b^{*2} + (l_2^2 - l_1^2)c^{*2} + 2(h_2 k_2 - h_1 k_1)a^* b^* \cos\gamma^*$$
$$+2(h_2 l_2 - h_1 l_1)a^* c^* \cos\beta^* + 2(k_2 l_2 - k_1 l_1)b^* c^* \cos\alpha^*$$
$$(6.2)$$

For the unidirectional lattice planes (h00),(0k0) and(00l), (6.1) simply gives:

$$a^* = |\frac{q_{h00}}{h}| \quad (6.3)$$

$$b^* = |\frac{q_{0k0}}{k}| \quad (6.4)$$

$$c^* = |\frac{q_{00l}}{l}| \quad (6.5)$$

Basically, all 6 unit-cell parameters $(a^*,b^*,c^*,\alpha^*,\beta^*,\gamma^*)$ can be calculated based on (6.1) and (6.2) by applying the recipe listed below:

1. $\underline{\alpha^*}$:According to the packing structure (see 1.3.2) and furthermore due to the missing out-of-plane $\boldsymbol{q}_z$ - component of the (0-20)-peak, $\alpha^*$ can be assumed to be $90°$.

2. $\underline{b^*}$: Using (6.4), we can calculate $b^*$ from the position of the (0-20)-peak.

3. $\underline{c^*}$: Using (6.5), we can calculate $c^*$ from the position of the specular peaks.

4. $\underline{a^*}$: By calculating $(\boldsymbol{q}^2_{1-10} - \boldsymbol{q}^2_{1-20})$ , $(\boldsymbol{q}^2_{0-20} - \boldsymbol{q}^2_{1-10})$ and building the difference, we end up with:

$$a^* = (\boldsymbol{q}^2_{1-10} - \boldsymbol{q}^2_{1-20}) - (\boldsymbol{q}^2_{0-20} - \boldsymbol{q}^2_{1-10}) + 6b^{*2} \tag{6.6}$$

5. $\underline{\gamma^*}$: $\gamma^*$ can now be calculated by inserting the results (a-d) into $(\boldsymbol{q}^2_{1-10} - \boldsymbol{q}^2_{1-20})$:

$$\gamma^* = \arccos \frac{(\boldsymbol{q}^2_{1-10} - \boldsymbol{q}^2_{1-20}) + 3b^*}{2a^*b^*} \tag{6.7}$$

6. $\underline{\beta^*}$: Knowing all other parameters, we can simply calculate $\beta^*$ by using $\boldsymbol{q}^2_{1-11}$:

$$\beta^* = \arccos \frac{\mathbf{q}^2_{1-11} - a^{*2} - b^{*2} - c^{*2} + 2b^*(a^* \cos \gamma^* + c^* \cos \alpha^*)}{2a^*c^*} \tag{6.8}$$

As shown above, all unit cell parameters can be determined from the position of the following peaks:

- 1-10, 1-11

- 0-20

- 1-20

This is not by accident. The reason for this is that next to their appearance in each reciprocal spacemap that has been measured on C8-BTBT thin and thick films, the diffraction spots of those **q**-values are partially linear independent (see fig. 6.5). Generally, one would have to search for suitable diffraction spots that allow to gain formulas for determining all six unit cell parameters.

For C8-BTBT, $\boldsymbol{q_p}$ and $\boldsymbol{q_z}$ has been evaluated by performing linescans within the spacemaps and fitting them as well as the regarding specular scans with gaussians at each temperature. Table 6.1 shows all extracted **q**-values.
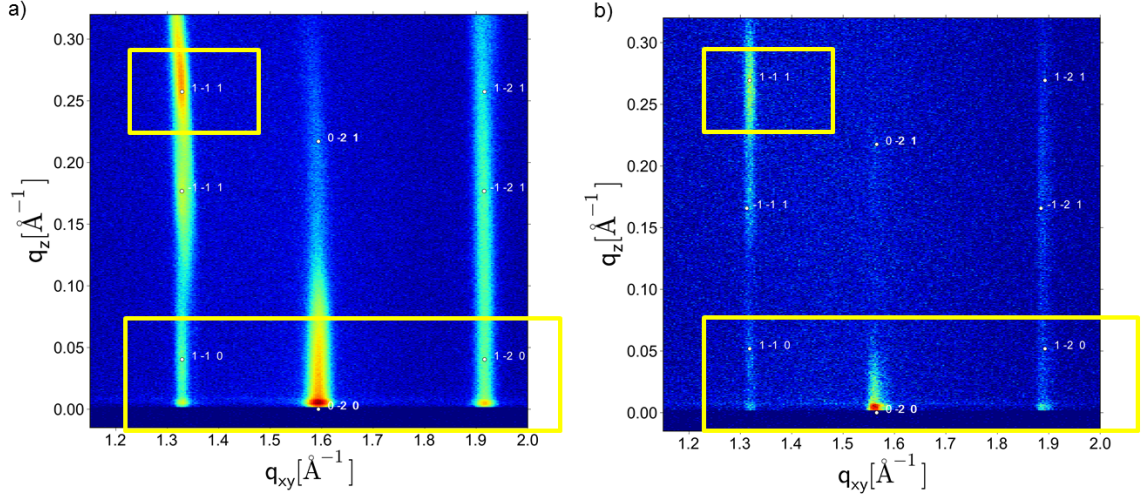
**Figure 6.5.:** Reciprocal spacemap indices of a) thick film and b) thin film at 25°C. The yellow marker shows the peaks that have been used for unit-cell determination.

| T | $q_{1-10}$ | $q_{0-20}$ | $q_{1-20}$ | $q_{1-11} - z$ | $q_{1-11} - p$ | $q_{001}$ |
|---|---|---|---|---|---|---|
| **Thick film** | | | | | | |
| 25 | 1.3296 | 1.5938 | 1.9167 | 0.2724 | 1.326 | 0.2171 |
| 50 | 1.3234 | 1.5888 | 1.9075 | 0.2632 | 1.322 | 0.2172 |
| 70 | 1.3185 | 1.5637 | 1.8891 | 0.2473 | 1.315 | 0.2172 |
| 85 | 1.3141 | 1.5489 | 1.8773 | 0.2313 | 1.311 | 0.2172 |
| 100 | 1.3097 | 1.5330 | 1.8639 | 0.2228 | 1.307 | 0.2174 |
| 30 *p.A.* | 1.3225 | 1.5749 | 1.8995 | 0.2646 | 1.319 | 0.2175 |
| **Thin film (double layer)** | | | | | | |
| 25 | 1.3192 | 1.5651 | 1.8933 | 0.2653 | 1.319 | 0.2175 |
| 70 | 1.3172 | 1.5572 | 1.8839 | 0.2400 | 1.316 | 0.2183 |
| 85 | 1.3141 | 1.5465 | 1.8765 | 0.2300 | 1.313 | 0.2183 |
| 30 *p.A.* | 1.3144 | 1.5531 | 1.8785 | 0.268 | 1.314 | 0(0.2165) |

**Table 6.1.:** Unit cell parameters of the thick- and thin film: Values of the 4 diffraction peaks. **Info**: Due to a missing specular scan, the $\mathbf{q}_{001}$-value of the thin film at 85°C was set to the same value as the 70°C -scan. the 25°C and 75°values have been evaluated by the $2^{nd}$ and $3^{rd}$ order peaks.

## 6.3.2. Result

Based on the **q**-values from table 6.1, unit cell parameters have been calculated based on the formulas derived in the previous chapter. Table 6.2 provides an overview of the unit-cell dimensions of the thin and thick film at certain temperatures. A graphical

| T °C | a | b | c | $\alpha$ | $\beta$ | $\gamma$ | V / Å |
|------|------|------|------|------|------|------|------|
| **Thick film** | | | | | | | |
| 25 | 5.9097 | 7.8845 | 28.9596 | 90.0010 | 92.1708 | 89.9745 | 1349.3671 |
| 50 | 5.9250 | 7.9094 | 28.9512 | 89.9918 | 92.2867 | 90.2056 | 1356.7479 |
| 70 | 5.9091 | 8.0363 | 28.9296 | 89.9987 | 90.5909 | 90.1245 | 1373.7842 |
| 85 | 5.9134 | 8.1131 | 28.9283 | 90.0003 | 89.7748 | 90.0669 | 1387.8585 |
| 100 | 5.9070 | 8.1973 | 28.9030 | 90.0013 | 89.4192 | 90.1320 | 1399.5166 |
| 30 *p.A.* | 5.9131 | 7.97920 | 28.9005 | 89.9989 | 91.6682 | 90.0390 | 1363.5580 |
| **Thin film (double layer)** | | | | | | | |
| 25 | 5.9422 | 8.0292 | 28.9229 | 90.0121 | 92.8068 | 89.7527 | 1379.9468 |
| 70 | 5.9025 | 8.0699 | 28.7854 | 89.9977 | 90.8364 | 90.1587 | 1371.1279 |
| 85 | 5.9153 | 8.1257 | 28.7827 | 90.0001 | 90.2910 | 89.9774 | 1383.4568 |
| 30 *p.A.* | 5.9114 | 8.0912 | 28.8582 | 89.9861 | 92.8720 | 90.2768 | 1380.3165 |

**Table 6.2.:** Calculated unit cell parameters of the thick and thin film.

interpretation of the results can be found in fig.6.6, which displays the absolute values of the parameters and the volume against temperature. In order to get a better understanding of how the unit cell is transformed whilst heating, fig. 6.7 presents the unit cell parameters normalized to the room-temperature structure.
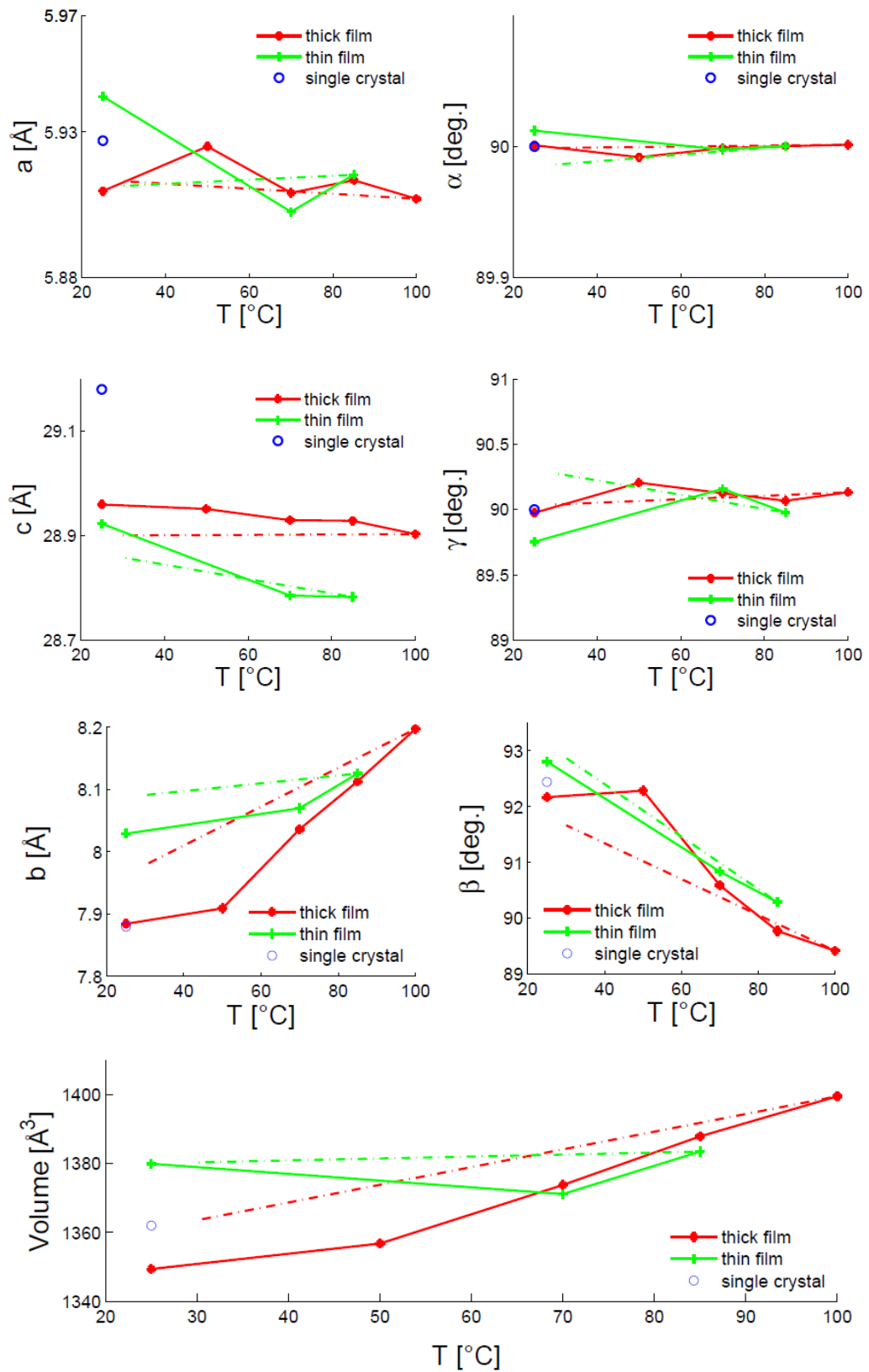
**Figure 6.6.:** Thermal expansion of the unit cell parameters for the thick and thin film in absolute values.

Summing up the results listed above:

- $a, c, \alpha$ and $\gamma$ are rather constant. There is even a slight decrease in $c$ and therefore the long molecule axis direction.

- The main change is due to the increase of the $b$-value, which means an in-plane expansion of the unit cell. Due to this result it is likely that the **tilt angle of the molecules** changes as the temperature raises.

- Next to the expansion, the **unit cell is becoming less tilted** as the temperature increases. This is reflected by the decreasing $\beta$-value.

- Thick and thin film show the same tendencies. However, it must be noted that according to the volume in fig. 6.6, the unit cell of the thin film is less dense packed at room temperature. Whilst heating, the two structures come close together and are finally nearly equal at 85°C. Interestingly, when cooling down, both structures get back into their initial state. A possible explanation would be the lack of material in the environment around the thin film preventing a more dense packing within the herringbone arrangement.

In order to confirm the results gained by our calculations, the calculated unit cells have been applied to their corresponding reciprocal spacemaps. The results can be seen in fig. 6.8. The position of the (hkl)-rods at room-temperature is marked by the white dashed line. It nicely shows the shift of the rods due to the increase of the $b$-value. Furthermore, it can be seen how the (-1-11) and (1-11)-peak get closer as the temperature increases. This is indeed the effect of the $\beta$ value converging against 90°and therefore because of the unit cell becoming upright standing.
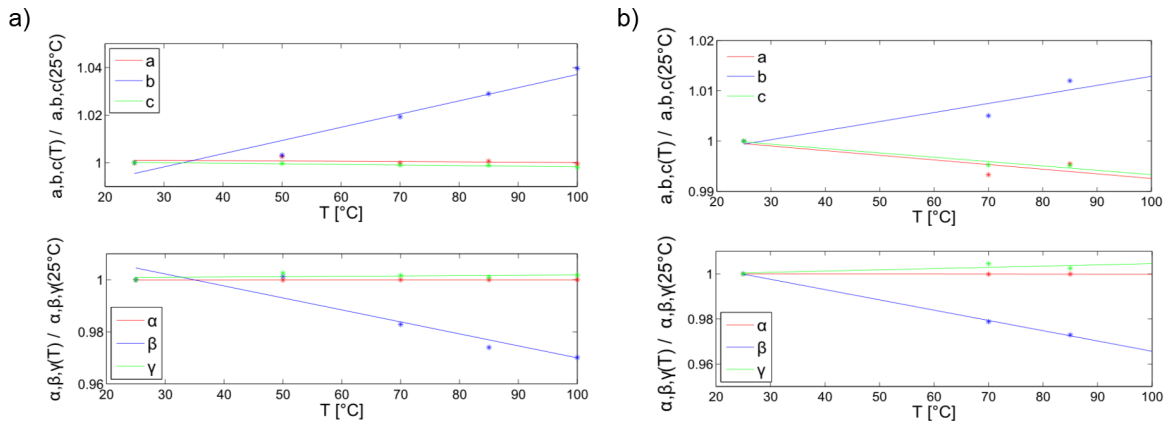


**Figure 6.7.:** Expansion of unit cell parameters compared to room temperature values for a) thick and b) thin film
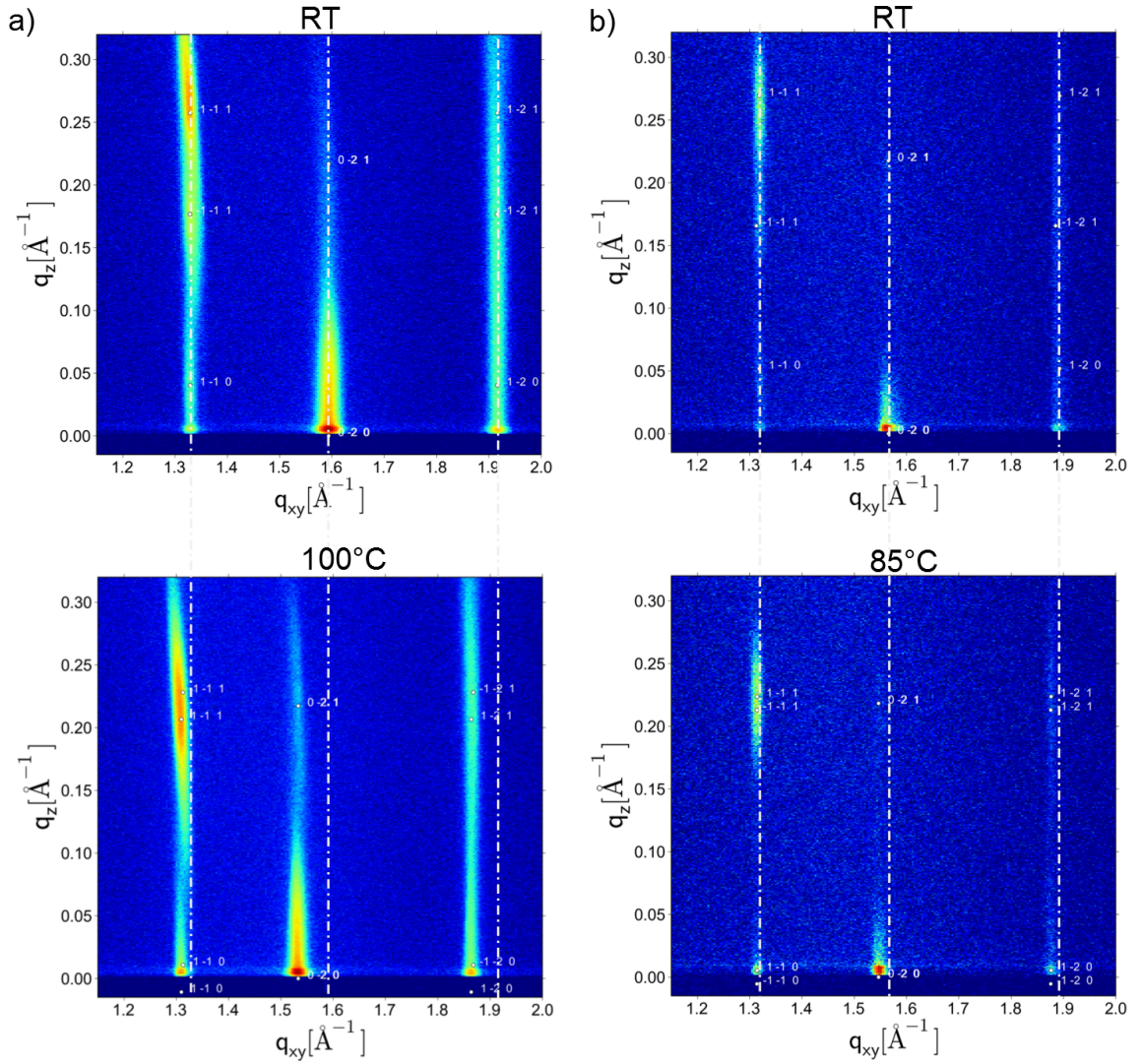
**Figure 6.8.:** Reciprocal spacemaps of a) thick film and b) thin film at room temperature and at high temperature. The spacemaps are indexed with the unit cell parameters listed in 6.2. For demonstration purposes, the dashed line marks the position of the (11L),(02L) and (12L)-rods at room temperature.

# 6.4. Phase transition

We will now focus on the phases and phase transitions of BTBT and show how they can be observed by the means of x-ray diffraction, i.e. grazing incidence diffraction (GIXD) and x-ray reflectivity (XRR).

According to the DSC (see chapter 1.3.1), a phase transition from the crystalline to the liquid crystalline smectic A (SmA) phase is expected to occur in the range of 110°C for the bulk material. Fig 6.9 gives a schematic representation of the two different states.



(a) crystalline          (b) smectic A
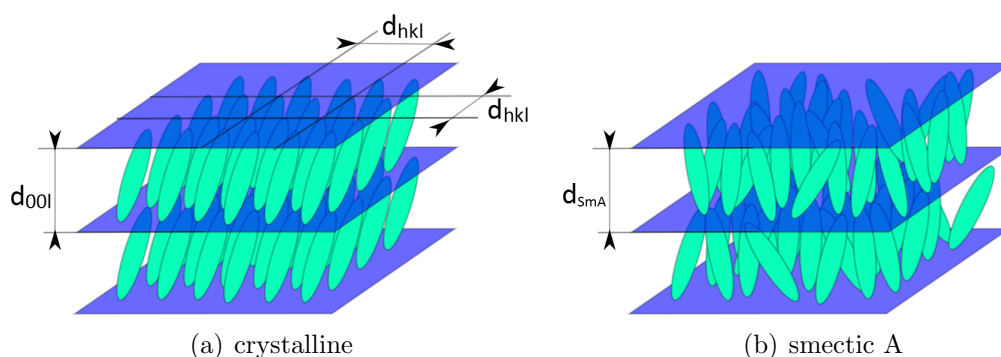
**Figure 6.9.:** Schematic presentation of the a) crystalline and b) smectic A phase obtained by $C_8$-BTBT

As explained in chapter 1.2, smectic states are characterised by the order of the molecules. They are maintaining the general orientational order of nematics, but also tend to align themselves in layers or planes. Depending on the degree of ordering, given by the order parameter $\sigma$, several smectic phases are possible. The SmA phase represents a structure quite near to the nematic and isotropic state, where all kind of in-plane order gets lost whilst there is still orientational and out-of-plane positional order of the molecules left (see fig. 6.9(b)). Thus, the out of plane ordering is observable via x-ray diffraction experiments by detecting the according Bragg peaks.

In-plane GIXD measurements of the two states can be seen in 6.10. Next to the out-of-plane periodicity represented by the (00l)-diffraction in specular scans, a broad range of in-plane reflections can be observed due to the in-plane ordering of the molecule in the herringbone-like pattern for the crystalline state (see fig. 6.10(a) and chapter 1.3.2). In contrast, a broad smectic peak raising from disordered in-plane alignment of the molecules can be observed when reaching the SmA-phase as can be seen in fig 6.10(b). To point out the huge difference, fig 6.11 shows a line scan along the sample-horizon at $\alpha_f$=0°. Due to the molecule length of $C8$-BTBT, the characteristic in-plane-shapes (crystalline herringbone and broad smectic peak) appear in the same range as the broad peak rising from the amorphous silicon oxide. Therefore, the $SiO_2$ peak has been added do demonstrate that it can clearly be distinguished from the

liquid crystalline smectic peak for the thick film. Unfortunately this is not possible for the thin film, preventing the observation of the smectic peak for systems consisting of less than 2-3 layers[3].
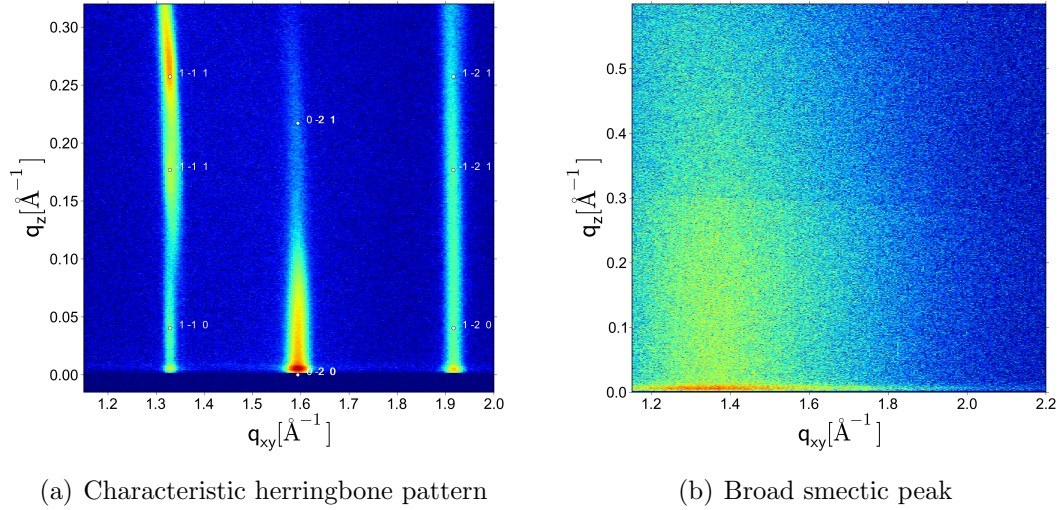


(a) Characteristic herringbone pattern



(b) Broad smectic peak

**Figure 6.10.:** Reciprocal spacemaps of the thick film in the a) crystalline state and b) smectic state.

Next to in-plane measurements and observation of in-plane-ordering, a shift of the (00l)-peak can be observed in XRR experiments once the phase transition occours. In the case of C8-BTBT, the peak moves to the left and therefore the interlayer distance of the smectic phase is larger then the crystalline distance ($\mathbf{d_{crystal}} < \mathbf{d_{smectic}}$). Speaking in numbers, the interlayer distance increases from $\mathbf{d_{Crystal}} = 29.01\mathring{A}$ to $\mathbf{d_{SmA}} = 29.35\mathring{A}$. This is quite expected due to the elevated mobility of the molecules through thermal energy. Interestingly, the peak does not shift between these two positions when keeping the temperature at exactly 110°C. Fig. 6.12(a) shows the shift of the peaks once the transition temperature to the smectic phase is exceeded. Keeping the temperature at 110°C for more than one hour both, the crystalline and the smectic phase can be observed over a long period of time (see fig. 6.12(b)).

Possible reasons for this behaviour are:

1. Inhomogeneous temperature on heating stage that partially leaves $T_{stage} < T_{trans}$.

2. Temperature gradient in crystallites leading to parts of the high crystallites staying crystalline across $T_{trans}$. An experimental proof can be found in fig. 6.21(f), where both states have been observed by optical microscopy at 113°C.

---

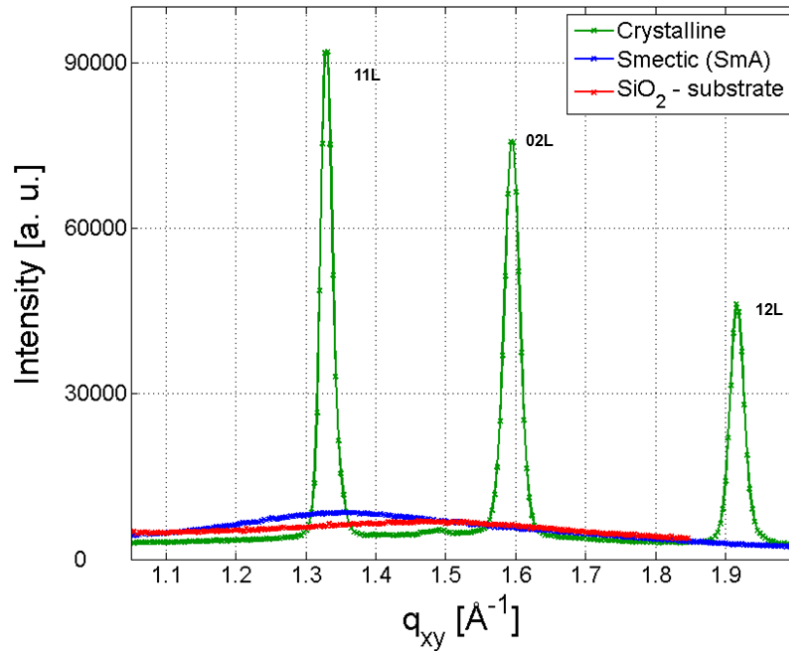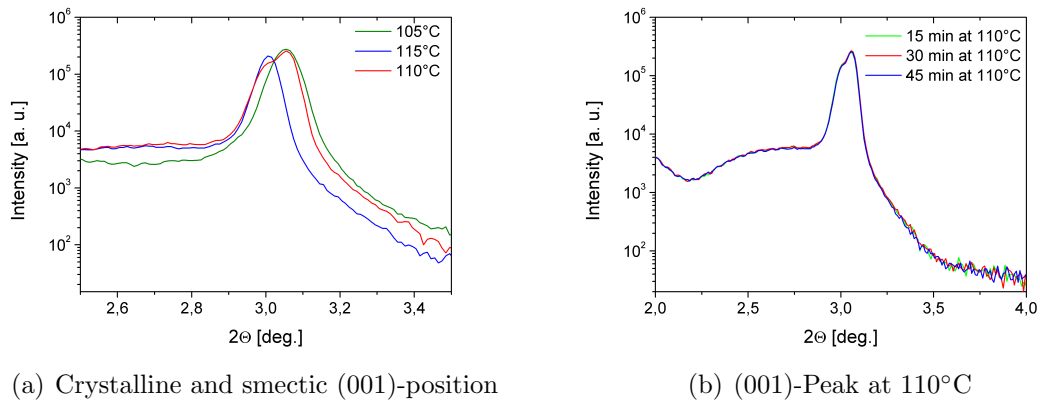[3]To overcome this issue, an alternative substrate like $AlO_2$ could be used.

**Figure 6.11.:** Linescan of the reciprocal spacemap along the horizon of the sample indicating the crysalline(green), the smectic(blue) phase and the amorphous peak from the $SiO_2$ substrate(red).



(a) Crystalline and smectic (001)-position

(b) (001)-Peak at 110°C

**Figure 6.12.:** a)Shift of the (001)-peak at the phase transition observed by x-ray reflectivity. b) Time-behaviour of the (001)-Peak at the $T_{trans} = 110°C$

77

In order to investigate how the crystalline phase evolves from the isotropic state, the sample was heated up to the isotropic phase at 130°C and cooled down to room temperature stepwise. Reciprocal spacemaps have been measured at temperature steps of $\Delta T$=5°. Fig 6.13a shows how the broad smectic peak develops from the isotropic peak when cooling down to the bulk transition temperature of 110°C. We have to keep in mind that, as mentioned in the chapters 6.2 and 5.3, the transition temperature is highly dependent on the film thickness and on the cooling rate applied. Therefore, we cannot see a crystalline ordering at 110°C. Cooling further, we can finally see how the herringbone evolves from the semectic state at 105°C and how it becomes very well defined at 85°C. Fig. 6.13b also shows the temperature shift due to thermal contraction as reverse effect of the thermal expansion we investigated in chapter 6.3.
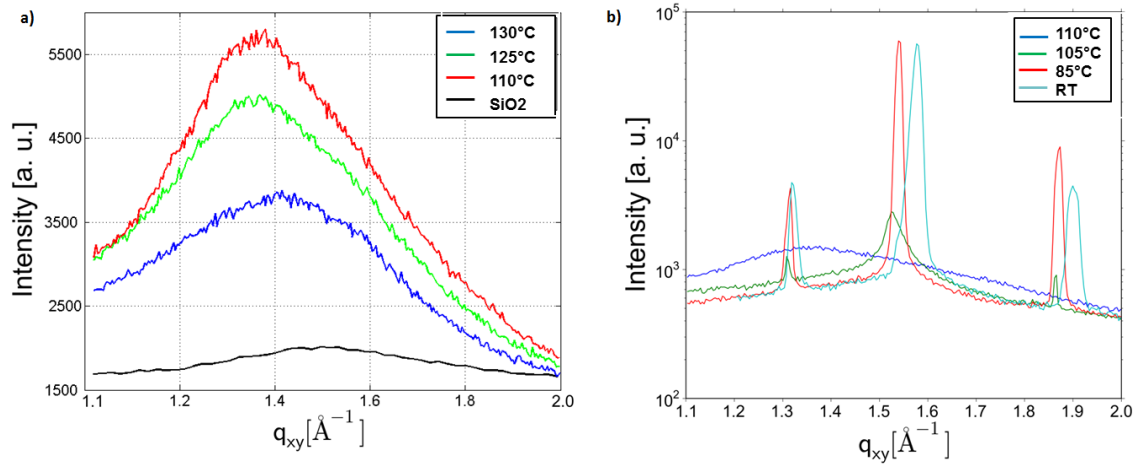


**Figure 6.13.:** Linescan of reciprocal spacemaps at certain temperatures indicating a) the isotropic to smectic A and b) smectic A to crystalline phase transition

## 6.5. Smectic Layer growth

Whereas the previous chapter focused on the crystallographic properties of the different C8-BTBT phases, we will now pay attention on morphological effects of the phase transition from the crystalline to the smectic state.

Remembering the thin-film results, it was found that at a certain temperature, the regime dominated by dewetting and crystallite formation stops and wetting leads to establishment of a uniform filled layer on the surface (see chapter 5.3). Furtheron, there are indications implying that this temperature is actually equal to the phase transition temperature $T_{trans}$. Getting to the thick film, one would expect some kind of similar effect. However, above 100°C an interesting effect comes into place. Indeed, as for the thin film dewetting stops and a wetting process leads to formation of a closed layer on the surface. Interestingly, the layering process turns out to be a very defined and temperature dependent behaviour. By increasing the temperature stepwise, a phenomenon known as "*Smectic Layer Growth*", can be observed.

In literature, this effect is often noted as *Layer-by-Layer surface freezing* or *Quantized layer growth*. The effect was extensively studied with cyano-biphenyl (CB) derivates (8CB,10CB and 12CB) in the 80's and 90's of the last century. In contrast to our findings, where layer growth occurred at the solid-smectic transition, defined layer-growth was found at the isotropic-nematic and nematic-smectic interface. It could be directly related to a change in surface tension and roughness (Ocko et al., 1986),(Pawlowska et al., 1987). This is actually in good agreement with our experimental results. As reported for the thin film in sec. 5, the transition from wetting to dewetting is directly related to the difference in surface tensions leading to wetting once the smectic phase is reached. According to (Zhang et al, 2008), the quantization could than be an effect of the surface becoming smoother as the number of layers covering the substrate increases [4]. Thus, each additional layer introduces a difference of the surface tension leading to a temperature range that has to be exceeded unless the next layer can be formed.

Fig 6.14 illustrates the effect observed by the means of x-ray reflectivty on the C8-BTBT thick film:

- **1 filled layer**(fig. 6.14(a)): The first layer is formed at a temperature of 105°C. It turns out that this layer is equal to the monolayer that is formed above 90°C for the thin film.

- **2 filled layers**(fig. 6.14(c)): The second layer appears on top of the first layer once exceeding a temperature of 107.5°C, possessing a layer thickness of d=2.9 nm. This indicates that the 2nd layer is formed with in a single crystal structure like manner too.

---

[4]It should be noted that the $SiO_2$ wafers we used are rather smooth as described in chapter 2.1.

- **3 filled layers**(fig. 6.14(e)): A third layer can be observed at 115°C. Again, a layer thickness of 2.9 nm is found.

- **Unstable layers above 118°C**: Even 4 and 5-layer states can be observed but it turns out that they are not stable over a longer period of time.

The fitting parameters used can be seen in table 6.3. As stated in the figure caption, all parameters were kept constant except the number of filled layers. In addition, the effect was observable with temperature dependent optical microscopy confirming our XRR results. Fig. 6.21(e) impressivly shows the formation of a new layer at a temperature of 111°C.

Also, AFM experiments have been performed at high temperatures. Whilst the first layer could nicely be seen at 100°C already[5](see fig.6.15(a)), it was hardly possible to proceed experiments within the smectic phase. Although successful AFM measurements within the SmA phase have been reported by several groups(Harth et al., 2011), it was not possible to deal the thermal oscillations of the cantilever and accomplish adequate measurements once exceeding the bulk phase transition temperature of 110°C. Fig.6.15(b) shows the results of a 110°measurement. The yellow dashed line indicates a possible step-edge of the 2nd layer.

| Layer | $d$ / $nm$ | $\rho$ / $g/cm^3$ | $\sigma$ / $nm$ |
|---|---|---|---|
| **Interface Layer** | 1.3 | 0.35 | 0.7 |
| **Filled layer** | | | |
| molecule core | $d_{Crystal} = 0.875, d_{SmA} = 0.900$ | 1.45 | 0 |
| alkyl chains | $d_{Crystal} = 1.013, d_{SmA} = 1.025$ | 0.80 | 0 |
| **Crystallites** | | | |
| molecule core | 0.90 | $0.70 - 0.60$ ($\rho$-fluctuation) | 0.3 |
| alkyl chains | 1.02 | $0.40 - 0.15$ ($\rho$-fluctuation) | 0 |

**Table 6.3.:** X-ray reflectivity fitting parameters. For the measurements at T = 105°C,107.5°C and 115°C, all fitting parameters except the number of filled layers was kept constant. Once exceeding the transition temperature the length of the molecule has been altered from **$d_{Crystal}$** to **$d_{SmA}$**.

Finally, it should be noted that as for the thin film, all kind of in-plane information gets lost once the onset of smectic layer growth is reached. So, in agreement with the wetting observed on the thin film, this implies that layering is directly related to the loss of crystallinity and thus can be directly related to the smectic state.
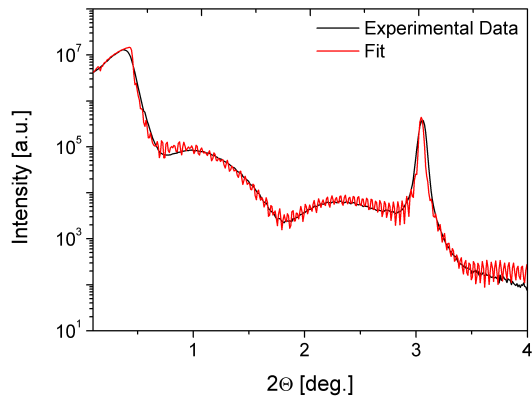
---

[5]This could be an effect of the additional energy placed by the laser that is aligning the cantilever of the AFM
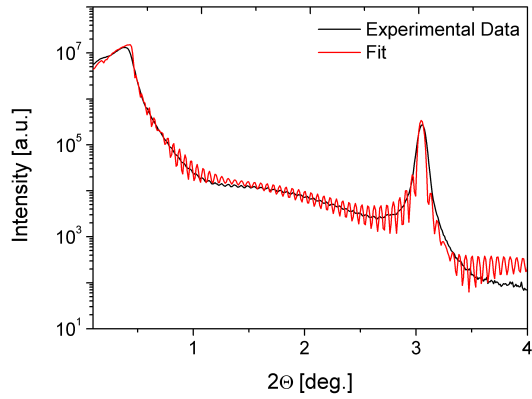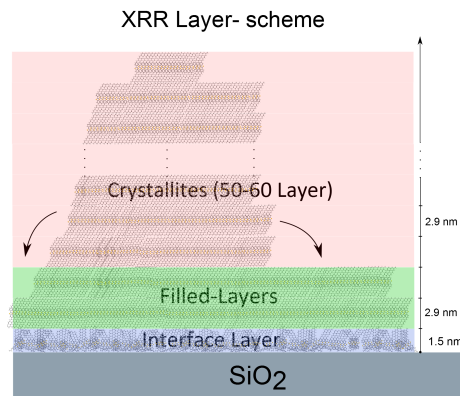
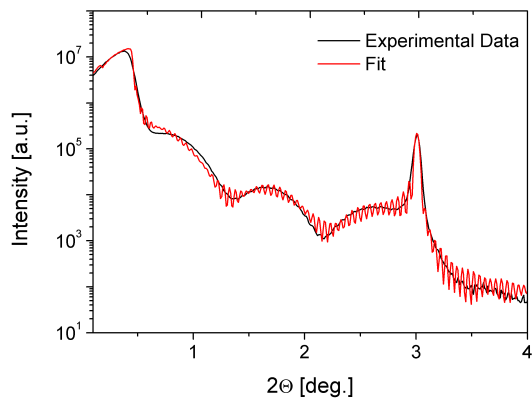(a) X-ray reflectivity of the thick film at 105°C.
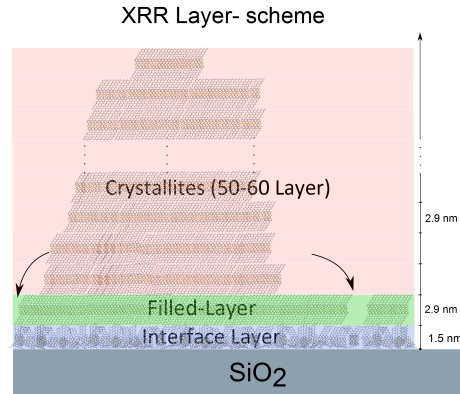
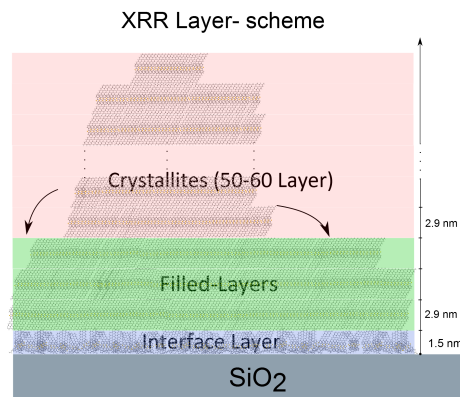(b) Fit-model for the 105°C-measurement.



(c) X-ray reflectivity of the thick film at 107.5°C.

(d) Fit-model for the 107.5°C-measurement.



(e) X-ray reflectivity of the thick film at 115°C.

(f) Fit-model for the 115°C-measurement.

**Figure 6.14.:** *Layer-by-Layer growth* observed by x-ray reflectivity.
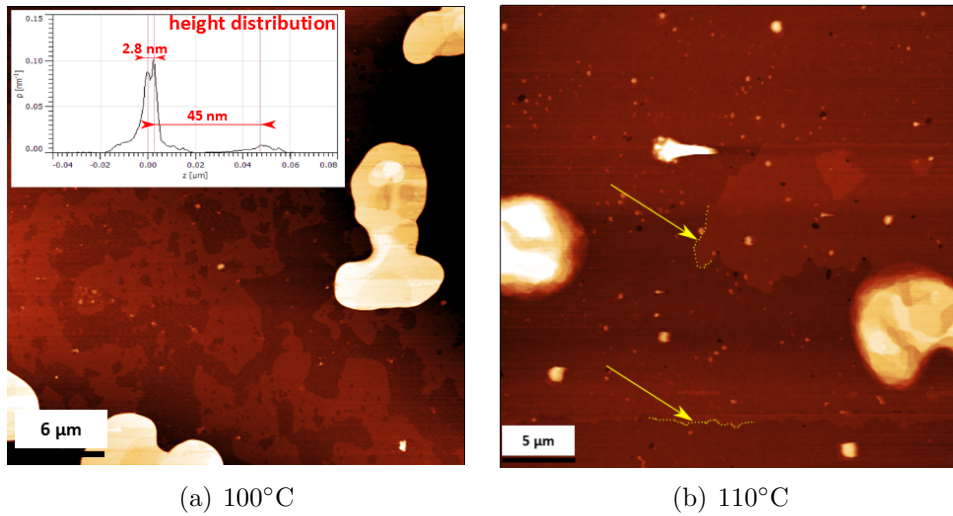
(a) 100°C

(b) 110°C

**Figure 6.15.:** AFM images of the thick film at a) 100°C (a first layer is established between the crystallites) and b) 110°C indicating creation of further layers

## 6.5.1. Thermal stability

Optical microscopy revealed, that the layer formation happens instantaneously once a certain threshold layering-temperature $T_{th}$ is reached. Once exceeded, material flow seems to stop unless enough energy to form the next layer has been introduced to the system. For the first layer, this temperature was found to be $T_{th}$=105°C, 107.5°C for the second and 115°C for the third layer as stated in the last section. Fig. 6.17 represents the stability of a layer when keeping the temperature constant in an *x layer state*. It can be seen that the layer gets more defined but does neither get back to a *(x-1) layer state*, nor proceed wetting to a *(x+1) layer state* for more than 2 hours at the same temperature.

This is not true for the 4 and 5-layer states that have been observed too. Getting closer to the phase transition from smectic to isotropic at 125°C, material starts to permanently flow. As a result, at e.g. 120°C an initial 4-layer state turns out to consist of 5 layers when performing XRR 30 minutes after the initial measurement.
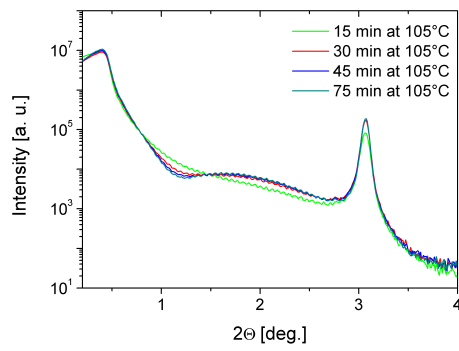
(a) 105°C (monolayer-state)
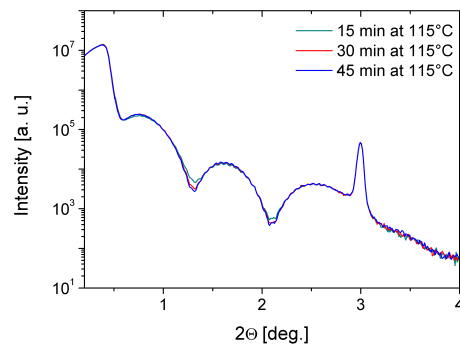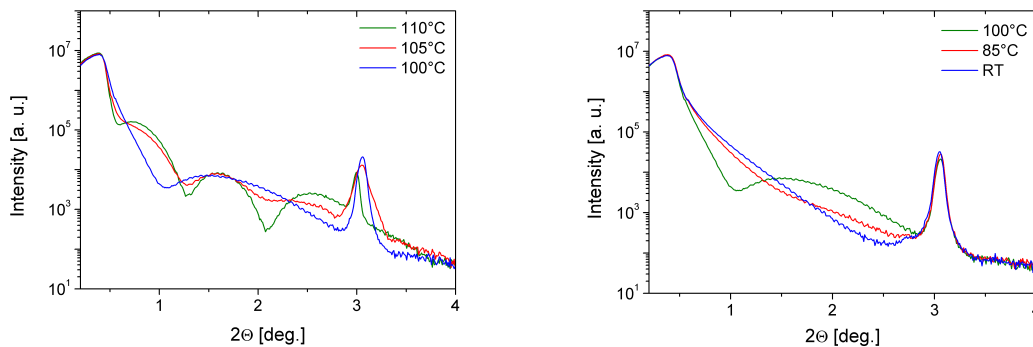
(b) 115°C (3-layer-state)

**Figure 6.16.:** X-ray reflectivity performed at specific temperatures indicating the stability of the layers formed by "*Smectic Layer Growth*".

## 6.6. Cooling behaviour

Due to the interesting effects we observed in the previous chapters, the cooling behaviour of the thin films has been investigated by heating to a certain temperature and applying different cooling rates whilst performing GIXD, XRR and optical microscopy in temperature intervals of $\Delta T$=5-10°C.

### 6.6.1. Slow Cooling

Starting from a "3-layer state" at 115°C, it can be seen that the upper two layers are vanishing in the range of 105°C (fig. 6.17(a)). Interestingly, the layer most close to the substrate remains. This indicates that the first layer is bound more strongly to the substrate due to thin film-substrate interactions than the subsequent layers. Further cooling finally leads to dewetting of this layer in the range of 85°C (fig. 6.17(b)). Due to this dewetting process, the room temperature morphology consists of huge crystallites only. Concluding this observations, it can be stated that dewetting is the dominating effect at low cooling rates.



(a) Transition from 3-layer to monolayer-state when cooling to 100°C

(b) Vanishing monolayer at 85°C

**Figure 6.17.:** X-ray-reflectivity of the thick film whilst cooling from 110°C to room temperature indicating the disappearance of filled layers and enhanced crystallite growth due to dewetting.

### 6.6.2. Fast Cooling

By applying higher cooling rates, it was found that the dewetting process could be overcome. Thus, it was possible to "*quench*" the morphology we obtained by heating our sample to high temperatures (i.e. a defined 1,2 or 3 layer state). Fig. 6.19(a) shows the XRR curve obtained when cooled from 120°C. It was possible to fit the curve with the same model we used for the heating in chapter 6.5 with some minor

modifications (adding a partially filled layer) to the fitting model (see fig.6.19(b)). Basically, all characteristic features:

- sharp Bragg-peak from the high crystallites (50-70 layer)

- broad Bragg-peak from the 4 filled layers

- Kiessig-fringes from the 4 filled layers

can be explained well by this method. To confirm these results, optical microscopy has been conducted. Fig. 6.18 shows the morphology of the thick film after cooling down from 120°C at a) slow and b) high cooling rates. In agreement with XRR-data, the quenched layer between the crystallites in fig. 6.18(b) turns out to be the proposed 4-layer state.
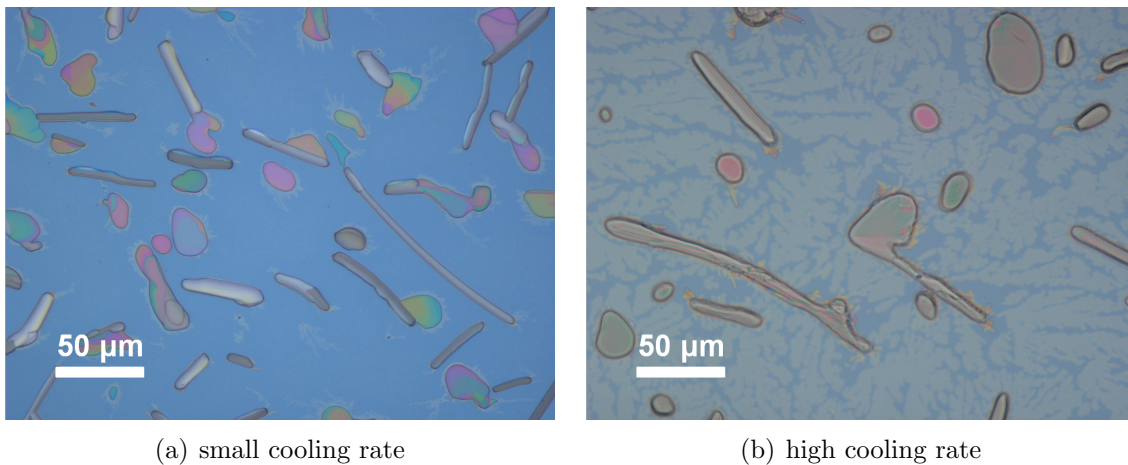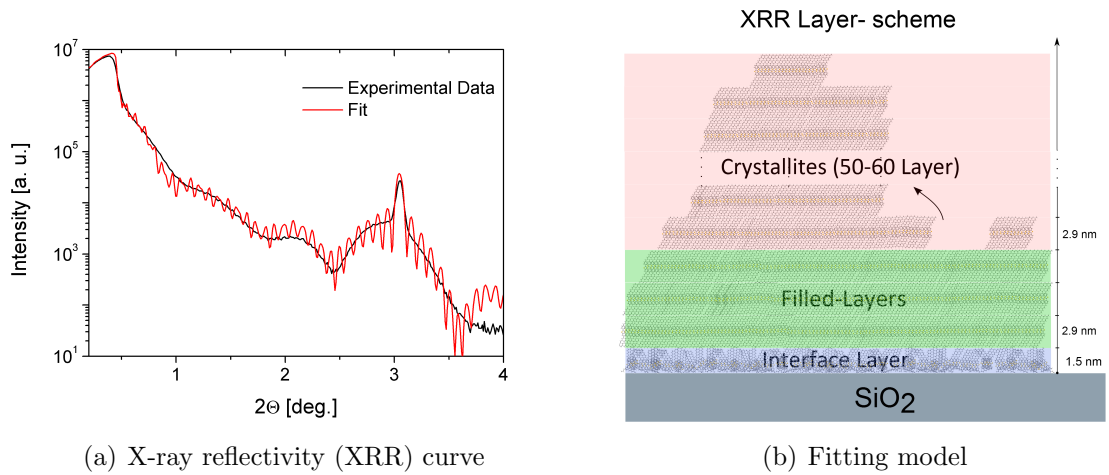


(a) small cooling rate          (b) high cooling rate

**Figure 6.18.:** Pictures of the thick film at room temperature after applying different cooling rates

(a) X-ray reflectivity (XRR) curve

(b) Fitting model

| Layer | $d$ / $nm$ | $\rho$ / $g/cm^3$ | $\sigma$ / $nm$ |
|---|---|---|---|
| **Interface Layer** | 0.9700 | 0.30 | 1.80 |
| **4 filled layers** | | | |
| molecule core | 0.8750 | 1.50 | 0 |
| alkyl chains | 1.0125 | 0.78 | 0 |
| **Partially filled layer** | | | |
| molecule core | 0.8750 | 0.73 | 1.35 |
| alkyl chains | 1.0125 | lower: 0.71, upper: 0.78 | lower: 0.70, upper: 1.35 |
| **Crystallites consisting of 35 layers** | | | |
| molecule core | 0.8750 | $0.71 - 0.30$ ($\rho$-fluctuation) | 0 |
| alkyl chains | 1.0125 | $0.15 - 0.05$ ($\rho$-fluctuation) | upper: 0.50 |

(c) Fit parameters

**Figure 6.19.:** X-ray reflectivity of the thick film after rapid cooling from the smectic phase. a) Reflectivity curve compared with fitted data b) Schematic drawing of the fitting model consisting of filled layers between the crystallites c) Fitting parameters (d = thickness, $\rho$ = density, $\sigma$ = roughness).

## 6.7. Conclusion

Giving a final ovierview, the behaviour of the thick and thin C8-BTBT film are pretty equal in terms of morphology, expansion and structure.

Fig 6.20 shows the temperature behaviour of a *C8-BTBT* thick film investigated by the means of XRR. Starting from the room temperature structure, consisting of islands with height up to 100 nm, it can be seen that up to 105°C crystallite formation leads to the raise of the (001)-Bragg-reflex at $\mathbf{q_z}$. Exceeding 105°C, material transport is reverted and reversible smectic layer growth takes place. On cooling, dewetting can be bypassed by applying high cooling rates providing the chance to create filled and thermally stable layer-structures at room temperature.

All results are in very good agreement with temperature dependent optical microscopy. Fig. 6.21 shows the history of the film from islands to crystallites, the layer formation and the quenched state after cooling down from the liquid crystal state.
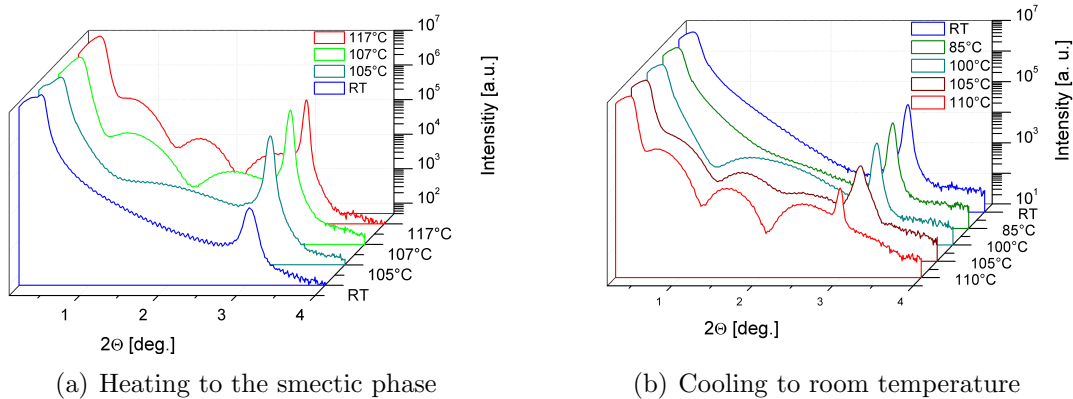


(a) Heating to the smectic phase

(b) Cooling to room temperature

**Figure 6.20.:** Temperature behaviour of the C8-BTBT thick film, investigated by x-ray-reflectivity.

(a) 25°C.

(b) 110°C

(c) 110.5°C

(d) 30 minutes at 111.5°C

(e) Layer growth at 111°C. The newly formed layer closes within a few seconds.
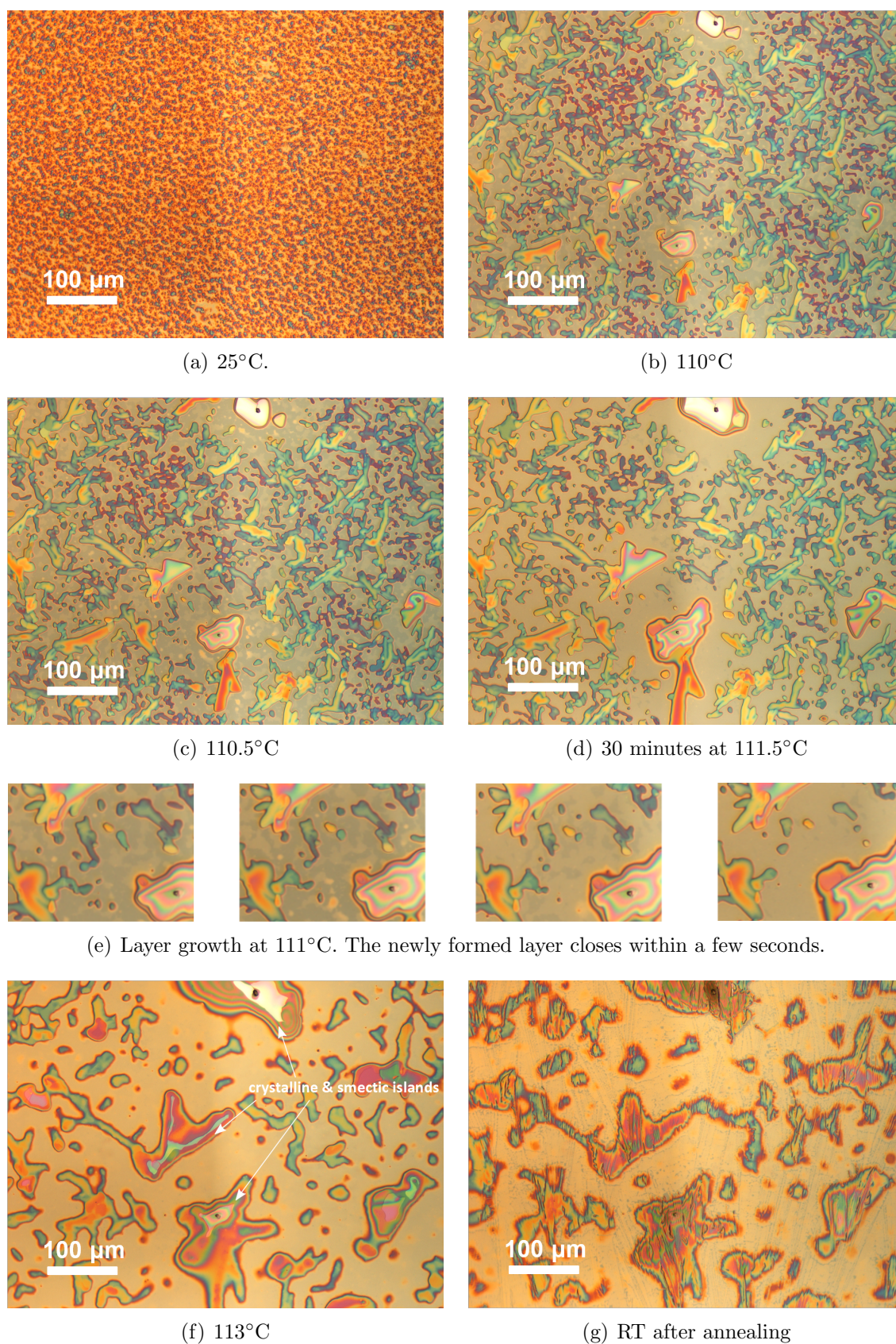
(f) 113°C

(g) RT after annealing

**Figure 6.21.:** Surface morphology of the thick film at different temperatures observed by optical microscopy.

# Appendix

# A. Intermediate film

Next to an ultra-thin film (monolayer) listed in chapter 5 and the thick film in chapter 6, investigations have been performed on different intermediate films. Due to the high roughness of the 100 nm film, it was not possible to e.g. perform temperature dependent AFM. However, it was of high interest to observe the dewetting process, crystallite formation and smectic layering of a system other than the monolayer by microscopy. Within this chapter, some results of a nominal 20 nm thick film will be presented.

## A.1. Atomic force microscopy

Temperature dependent AFM was performed during heat treatment up to the smectic phase. Fig. A.1 shows the morphology of the 20 nm film at room temperature. Interestingly the island formation does not start at the substrate surface directly. As can be seen, there is a $\approx 9.1$ nm base layer with a sharp edge underneath the islands. This is in good agreement with AFM-measurements performed on the ultra-thin film where the dendritic shape disappears once the layer thickness exceeds 5.7 nm, i.e. the two layer state (see chapter 5 and appendix B).
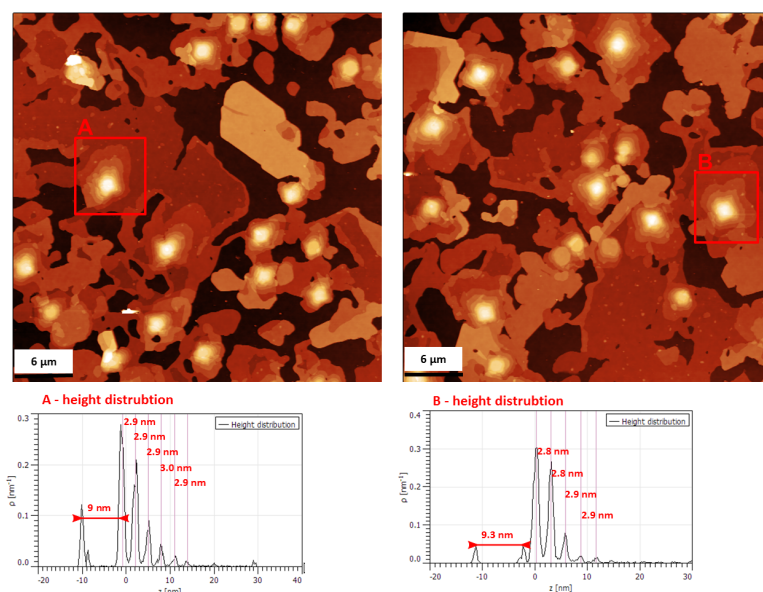


**Figure A.1.:** AFM picutre of the intermediate film after fabrication showing islands on a well defined base consisting of 3 C8-BTBT-layers.
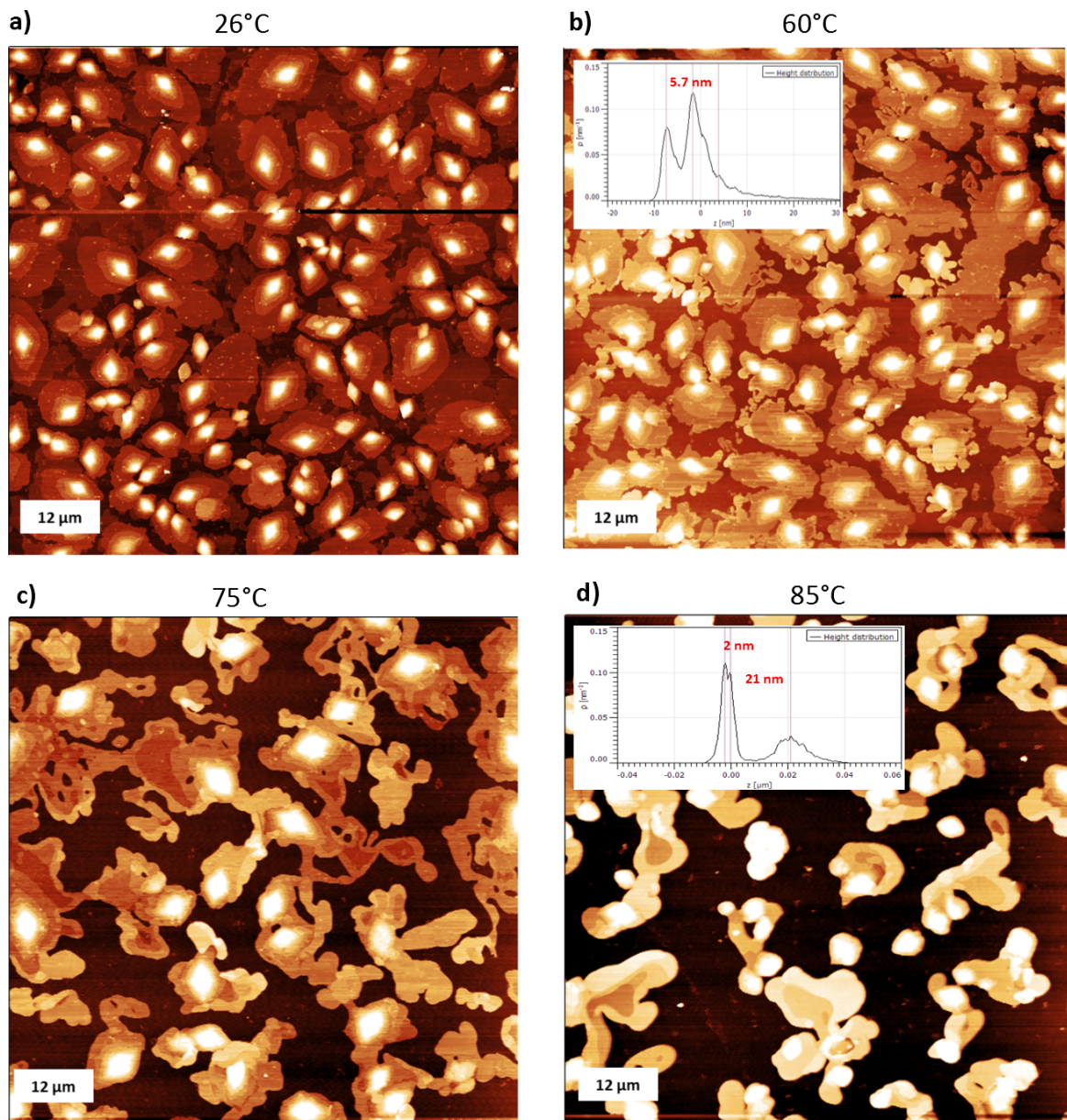
**Figure A.2.:** Dewetting of the intermediate film observed by AFM. a) At 40°C the morphology is governed by huge islands b) Up to 60°C, dewetting and therefore crystallite formation is rather slow. A bilayer structure is formed underneath the islands c) At 75°C, huge crystallites above the still observable base-layer can be observed next to regions with bare substrate. d) Finally, the base layer is participating in crystallite formation and we end up with huge crystallites with a height between 20 and 47 nm upon the bare substrate.

## A.2. Optical Microscopy

The intermediate film has been observed by optical microscopy during heating up to 120°C in order to investigate the smectic layering effect described in chapter 6.5.

Bascially all characteristic features of the monolayer as well as 100 nm thick film:

- **Dewetting**: Up to $\approx 110$°C, dewettting leads to a formation of crystallites with a height up to 20-50 nm (see fig. A.2).

- **Smectic layer growth**: Fig. A.5 displays the layering process. As can be seen, a layer nucleates at a certain temperature and gets closed within a few seconds once nucleated. After that, it takes a certain amount of thermal energy unless nucleation of the next layer occurs.

- **Cooling**: As for the thick film, the quantized layer structure at high temperatures can be quenched down to room temperature by fast cooling. Fig. A.4(b) shows the dendritic shape that seems to be a characteristic feature of the 2-layer state. For comparison, a quenched 3-layer state is depicted in fig. A.4(a).
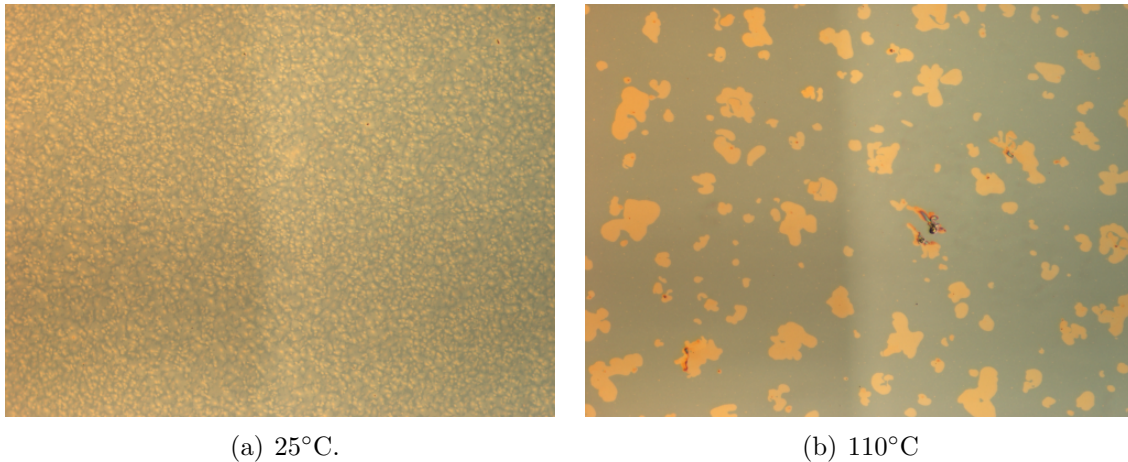


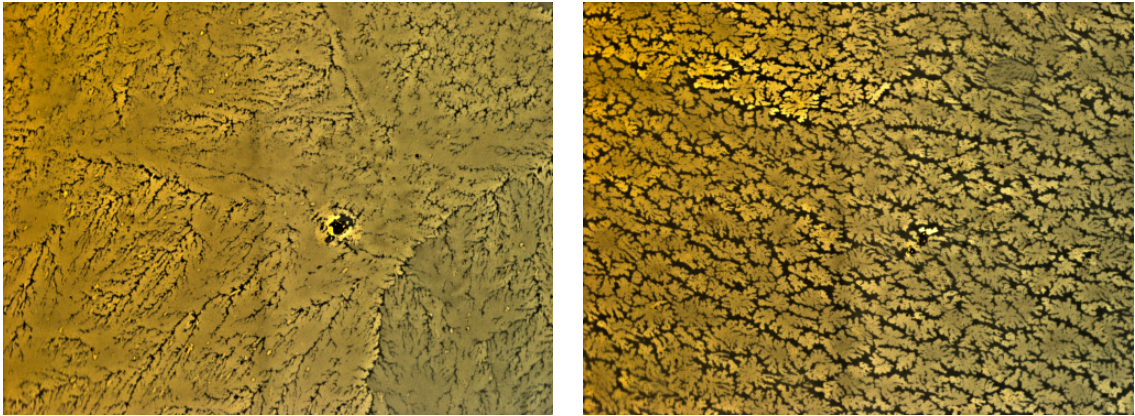(a) 25°C.                    (b) 110°C

**Figure A.3.:** Dewetting of the intermediate film observed by optical microscopy. The behaviour is equal to the dewetting effects observed for the thin and thick film. The island-governed structure is transformed into rather large crystallites upon cooling up to 105°C.

(a) Cooled from state consisting of 3 nearly filled layers

(b) Cooled from state consisting of 2 filled layers and a few small crystallites left

**Figure A.4.:** Cooling behaviour of the thin film observed by optical microscopy. As can be seen, the dendritic structure discussed in chapter 5.2 seems to be a property of a system consisting of two BTBT-layers. The pictures have been digitally modified for demonstration purposes.

(a) 110.5°C.

(b) 111°C

(c) 111.5°C

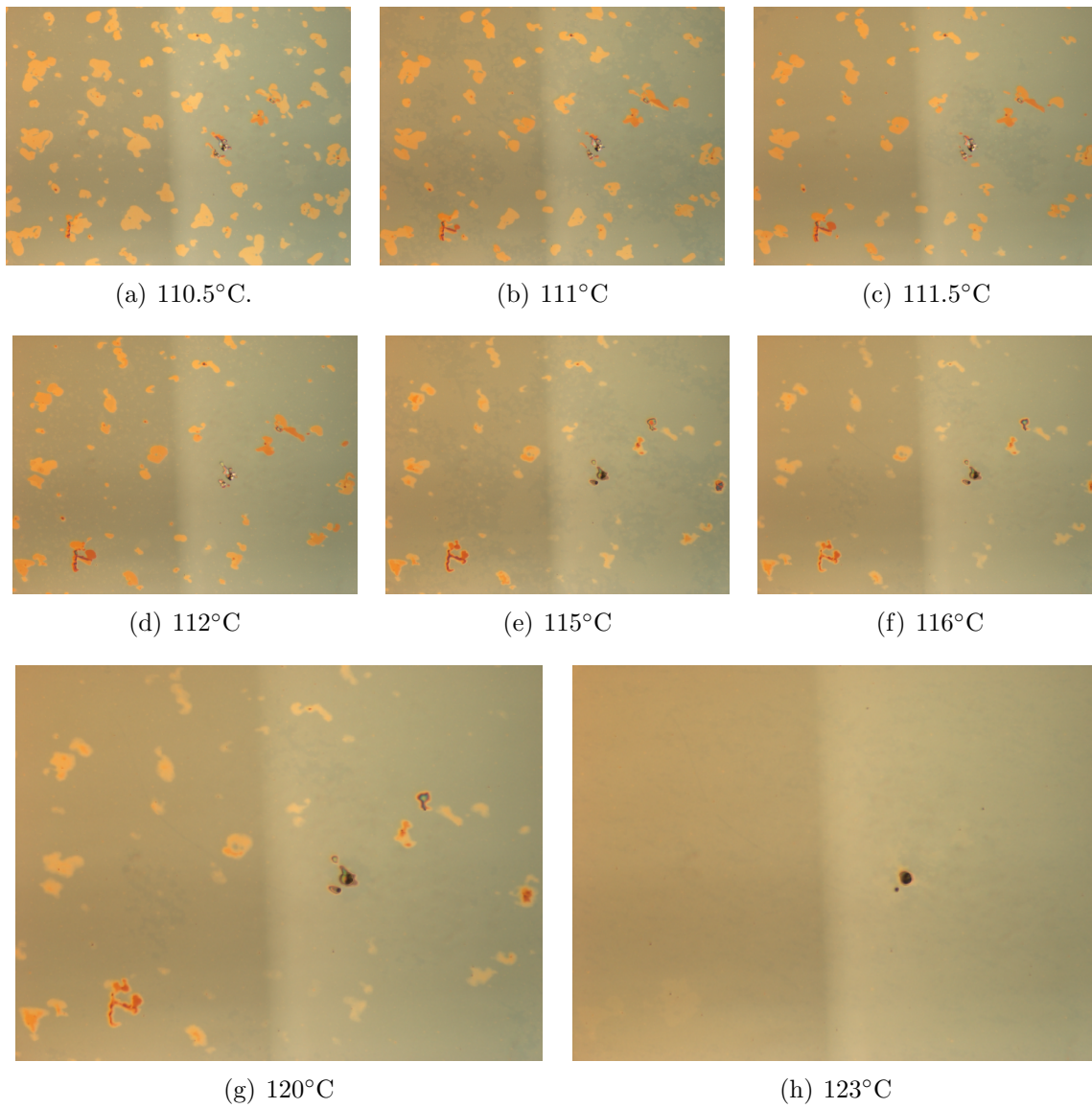(d) 112°C

(e) 115°C

(f) 116°C

(g) 120°C

(h) 123°C

**Figure A.5.:** Smectic layering of the intermediate film observed by temperature dependent optical microscopy. It can clearly be seen how (a-c) how the first, (d-f) the second and(e-g) a third layer nucleates and evolves when increasing the temperature.

(a) 110°C.

(b) 110.5°C

(c) 111°C

(d) 111°C, 10 seconds after A.6(c)
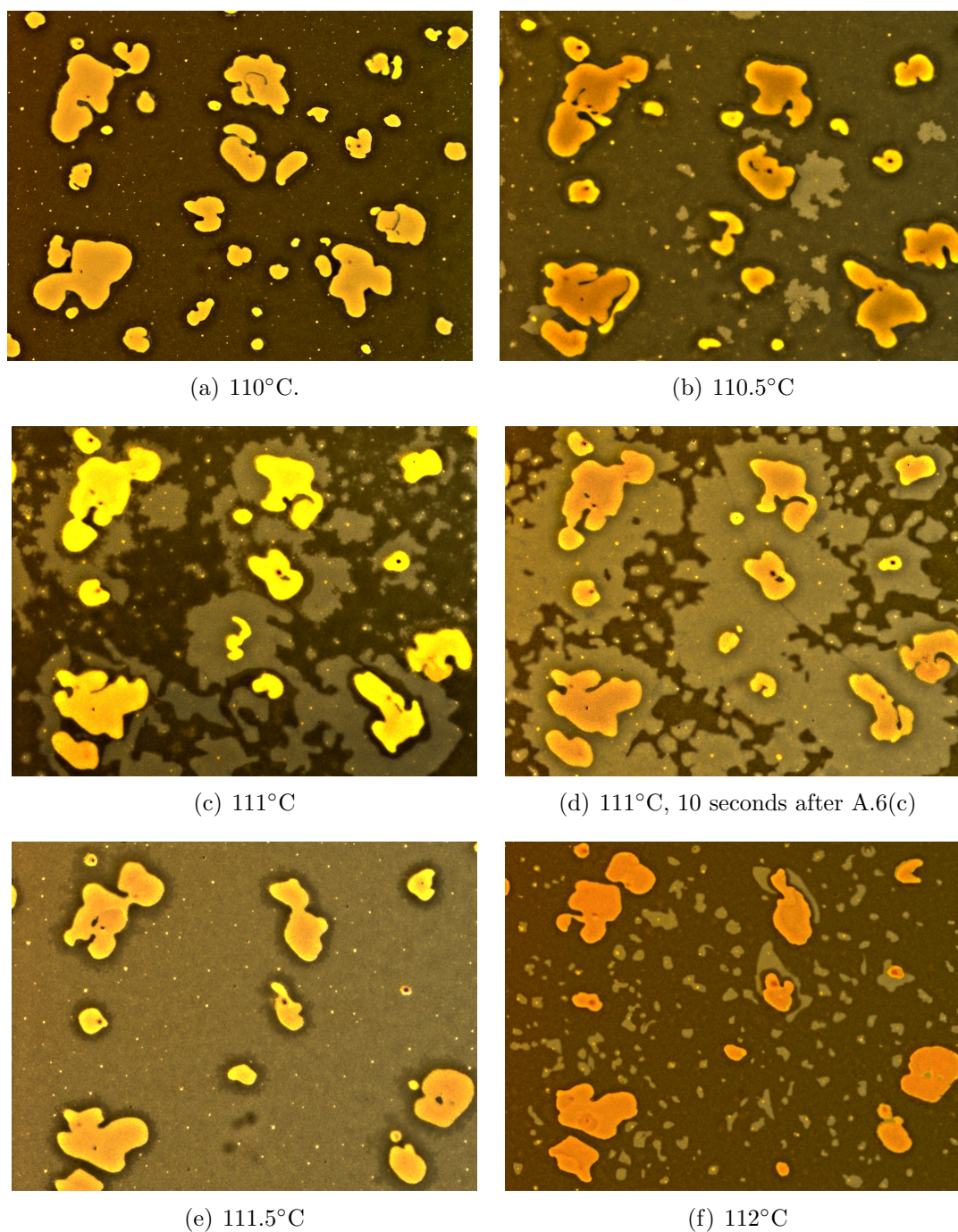
(e) 111.5°C

(f) 112°C

**Figure A.6.:** Digitally modified pictures of the smectic layering observed by temperature dependent optical microscopy. (a-d) Nucleation and layer formation of the first layer. (e-f) Nucleation and start of layer formation of the second layer.

# B. Thin film - Supplemental information

## B.1. Atomic force microscopy

Next to the dendritic shape discussed in chapter 5.2, a second morphology can be observed once a third layer is created above the dendritic structure (see fig. B.1). These observation is in good agreement with our findings for the thin film:

1. There is still a slight dewetting process at room temperature once the quite stable dendritic structure is established.

2. The dendritic shape is turned into a more sharp-edged crystalline shape once the film consists of more than two layer (see fig. B.1(b) and A.4).
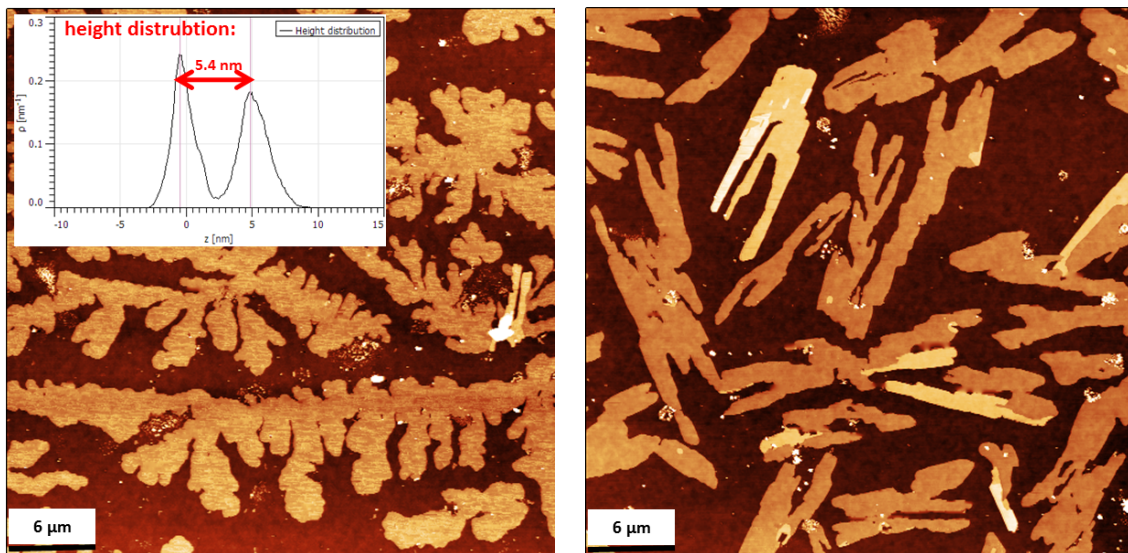


(a) Crystal-like shape appearing on top of dendritic structure once a third layer is formed.



(b) Compound of dendritic and more sharp-edged crystlline shapes in a 2-3 layer system

**Figure B.1.:** Dewetting of the intermediate film observed by optical microscopy. The behaviour is equal to the dewetting effects observed for the thin and thick film. The island-governed structure is transformed into rather large crystallites upon cooling up to 105°C.

# C. Thick film - Supplemental information

## C.1. Specular Scan, Williamson Hall analysis

Several investigations have been performed on a drop-casted film with a thickness in the range of 200 nm. Due to the high level of crystallinity, Bragg-reflexes up to the 20th order can be observed in specular scans (see fig. C.1).

As shown by Williamson and Hall in 1952, the peak broadening of those Bragg reflections allows to analyse crystallite size as well as micro strains within the material according to the following formula (Williamson and Hall, 1953):

$$\beta \cos \theta = 2\epsilon \sin \theta + \frac{\lambda}{D} \tag{C.1}$$

where $\beta$ denotes the peak-broadening, D the crystallite size and $\epsilon = \frac{\Delta d}{d}$ the microstrain. Before performing a Williamson - Hall analysis it is of high importance to remove the influence of $K\alpha_2 radiation$ on peak broadening. In our case the recursive method introduced by Rachinger was used (Rachinger, 1948):

$$I(2\theta) = I_{measured}(2\theta) - R_{21}I_{measured}\left\{2\theta - 2\arcsin \frac{\lambda_{\alpha_2}}{\lambda_{\alpha_1}}\sin \theta\right\} \tag{C.2}$$

$R_{21}$ denotes the intensity ratio ($\approx 0.51$) and $I_{measured}$ the detected intensity.

The results can be seen in fig. C.2. As can be seen the slope is approaching zero once $K_{\alpha_2}$ is removed. This indicates that in our experiment we are measuring out of the resolution limit of our setup rather than the real line-broadening.

This is also reflected by quite uneven results. When using (C.1) to determine the crystallite size D, depending on the diffractometer used, following values were gained:

- Siemens diffractometer (uncorrected): D = 112 nm

- Panalytical Empyrean System (uncorrected): D = 89 nm

- Siemens diffractometer ($K_{\alpha_2}$ corrected): D = 174 nm
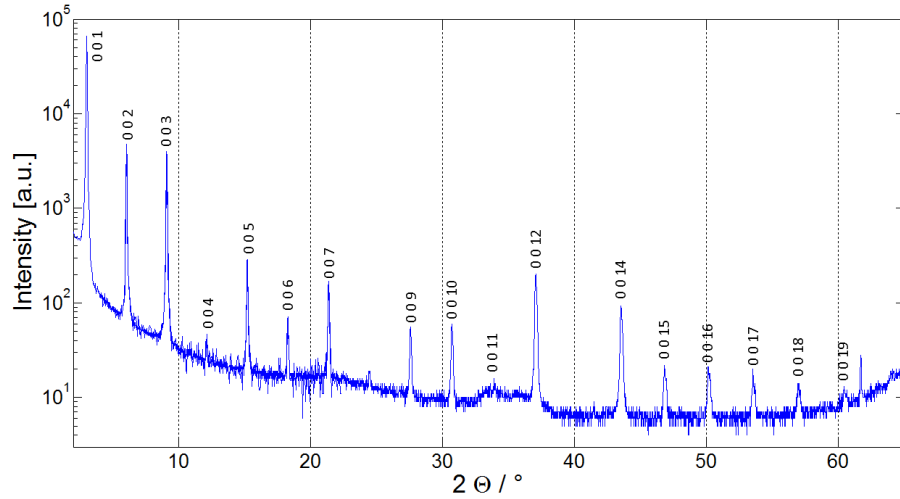
**Figure C.1.:** Specular scan of a drop-casted thick film (thickness ≈ 200 nm). The high number of observable orders of the (00l)-peaks (up to the 19th order) indicates the rather high cristallinity of the system.



**Figure C.2.:** Williamson Hall plot of a drop-casted thick film. A $K\alpha_2$ correction has been performed (green line). As can be seen, the slope is approaching zero and thus it is likely that the measurements are done in the resolution limit of the experimental setup.

# Bibliography

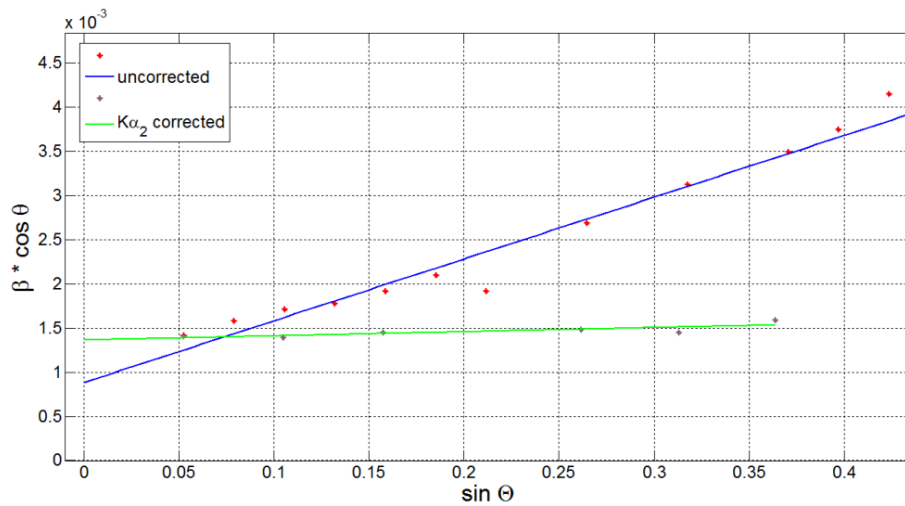[A. Gibaud 2000]   A. GIBAUD, S.Hazra:  X-ray reflectivity and diffuse scattering. In: *Current Science* 78 (2000), June, No. 12, S. 1467–1477

[Als-Nielsen and McMorrow 2001]   ALS-NIELSEN, J ; MCMORROW, Des: *Elements of modern X-ray physics.* 2001. –  ISBN 0471498572 9780471498575 0471498580 9780471498582

[Anton Paar GmbH - website 2012]   ANTON PAAR GMBH - WEBSITE: *Domed Hot Stage for Four-Circle Goniometers: DHS 900.* June 2012. –  URL `http://www.anton-paar.com/Domed-Hot-Stage-for-Four-Circle-Goniometers-DHS-900/XRD/60_Corporate_en?product_id=132`

[Baron and Stepto 2002]   BARON, M. ; STEPTO, R. F. T.: Definitions of basic terms relating to polymer liquid crystals(IUPAC Recommendations 2001). In: *Pure and Applied Chemistry* 74 (2002), No. 3, S. 493–509. – ISSN 0033-4545, 1365-3075

[Beiglboeck 2009]   BEIGLBOECK, Wolf: *X-ray and Neutron Reflectivity Principles and Applications.* Springer, 2009

[Benichou et al. 2003]   BENICHOU, O ; CACHILE, M ; CAZABAT, A.M ; POULARD, C ; VALIGNAT, M.P ; VANDENBROUCK, F ; VAN EFFENTERRE, D:  Thin films in wetting and spreading. In: *Advances in Colloid and Interface Science* 100-102 (2003), February, S. 381–398. – ISSN 00018686

[Binnig and Quate 1986]   BINNIG, G. ; QUATE, C. F.:  Atomic Force Microscope. In: *Physical Review Letters* 56 (1986), No. 9, S. 930–933. – ISSN 0031-9007

[Björck and Andersson 2007]   BJÖRCK, Matts ; ANDERSSON, Gabriella: GenX : an extensible X-ray reflectivity refinement program utilizing differential evolution. In: *Journal of Applied Crystallography* 40 (2007), November, No. 6, S. 1174. – ISSN 0021-8898

[Croce and Névot 1976]   CROCE, P. ; NÉVOT, L.:  Étude des couches minces et des surfaces par réflexion rasante, spéculaire ou diffuse, de rayons X. In: *Revue de Physique Appliquée* 11 (1976), No. 1, S. 113–125. – ISSN 0035-1687

[Dane et al. 1998]   DANE, A.D. ; VELDHUIS, A. ; BOER, D.K.G.de ; LEENAERS, A.J.G. ; BUYDENS, L.M.C.: Application of genetic algorithms for characterization of thin layered materials by glancing incidence X-ray reflectometry. In: *Physica B: Condensed Matter* 253 (1998), October, No. 3-4, S. 254–268. – ISSN 09214526

BIBLIOGRAPHY

[Demus 1999]    DEMUS, Dietrich: *Physical properties of liquid crystals.* Weinheim; New York : Wiley-VCH, 1999. – ISBN 3527297472 9783527297474

[Dierking 2004]    DIERKING, Ingo: *Textures of liquid crystals.* Weinheim : Wiley-VCH, 2004. – ISBN 3527307257 9783527307258 3527602054 9783527602056

[Dietrich 1998]    DIETRICH, Demus: *Handbook of liquid crystals 1, Fundamentals.* Weinheim : Wiley-VCH, 1998. – ISBN 3527292705 9783527292707

[Dosch 1992]    DOSCH, Helmut: *Critical phenomena at surfaces and interfaces : evanscent x-ray and neutron scattering.* Berlin [etc.] : Springer-Verlag, 1992. – ISBN 3540545344 9783540545347 0387545344 9780387545349

[Ebata et al. 2007]    EBATA, Hideaki ; IZAWA, Takafumi ; MIYAZAKI, Eigo ; TAKIMIYA, Kazuo ; IKEDA, Masaaki ; KUWABARA, Hirokazu ; YUI, Tatsuto: Highly Soluble [1]Benzothieno[3,2- b ]benzothiophene (BTBT) Derivatives for High-Performance, Solution-Processed Organic Field-EffectTransistors. In: *Journal of the American Chemical Society* 129 (2007), December, No. 51, S. 15732–15733. – ISSN 0002-7863, 1520-5126

[Erb et al. 2005]    ERB, T. ; ZHOKHAVETS, U. ; GOBSCH, G. ; RALEVA, S. ; STUEHN, B. ; SCHILINSKY, P. ; WALDAUF, C. ; BRABEC, C. J.: Correlation Between Structural and Optical Properties of Composite Polymer/Fullerene Films for Organic Solar Cells. In: *Advanced Functional Materials* 15 (2005), July, No. 7, S. 1193–1196. – ISSN 1616-301X, 1616-3028

[Gustafsson et al. 1992]    GUSTAFSSON, G. ; CAO, Y. ; TREACY, G. M. ; KLAVETTER, F. ; COLANERI, N. ; HEEGER, A. J.: Flexible light-emitting diodes made from soluble conducting polymers. In: *Nature* 357 (1992), June, No. 6378, S. 477–479. – ISSN 0028-0836

[Harth et al. 2011]    HARTH, Kirsten ; SCHULZ, Benjamin ; BAHR, Christian ; STANNARIUS, Ralf: Atomic force microscopy of menisci of free-standing smectic films. In: *Soft Matter* 7 (2011), No. 15, S. 7103. – ISSN 1744-683X, 1744-6848

[HASYLAB-website 2012]    HASYLAB-WEBSITE: *Beamline W1.1 (ROEWI).* June 2012. – URL `http://hasylab.desy.de/facilities/doris_iii/beamlines/w1_roewi/index_eng.html`

[Hlawacek et al. 2008]    HLAWACEK, Gregor ; PUSCHNIG, Peter ; FRANK, Paul ; WINKLER, Adolf ; AMBROSCH-DRAXL, Claudia ; TEICHERT, Christian: Characterization of step-edge barriers in organic thin-film growth. In: *Science* 321 (2008), Jul, No. 5885, S. 108–111

[Huynh 2002]    HUYNH, W. U.: Hybrid Nanorod-Polymer Solar Cells. In: *Science* 295 (2002), March, No. 5564, S. 2425–2427. – ISSN 00368075, 10959203

[Iino and Hanna 2006]  Iino, Hiroaki ; Hanna, Jun-ichi:  Availability of Liquid Crystalline Molecules for Polycrystalline Organic Semiconductor Thin Films. In: *Japanese Journal of Applied Physics* 45 (2006), August, No. No. 33, S. L867–L870. – ISSN 0021-4922

[Khazins et al. 2004]  Khazins, D.M. ; Becker, B.L. ; Diawara, Y. ; Durst, R.D. ; He, B.B. ; Medved, S.A. ; Sedov, V. ; Thorson, T.A.:  A parallel-plate resistive-anode gaseous detector for X-ray imaging. In: *IEEE Transactions on Nuclear Science* 51 (2004), June, No. 3, S. 943–947. – ISSN 0018-9499

[Kiessig 1931]  Kiessig, Heinz:  Interferenz von Röntgenstrahlen an dünnen Schichten. In: *Annalen der Physik* 402 (1931), No. 7, S. 769–788. – ISSN 00033804, 15213889

[Lengyel et al. 2006]  Lengyel, O. ; Hardeman, W.M. ; Wondergem, H. J. ; Leeuw, D. M. de ; Breemen, A.J.J.M. van ; Resel, R.: Solution-Processed Thin Films of Thiophene Mesogens with Single-Crystalline Alignment. In: *Advanced Materials* 18 (2006), April, No. 7, S. 896–899. – ISSN 0935-9648, 1521-4095

[LinKam-website 2012]  LinKam-website:  *GS350-Heating stage.* June 2012. – URL http://www.linkam.co.uk/gs350-features/

[Liu et al. 2010]  Liu, Chuan ; Minari, Takeo ; Lu, Xubing ; Kumatani, Akichika ; Takimiya, Kazuo ; Tsukagoshi, Kazuhito: Solution-Processable Organic Single Crystals with Bandlike Transport in Field-Effect Transistors. In: *Adv Mater* (2010), Nov

[Madsen et al. 2004]  Madsen, L. A. ; Dingemans, T. J. ; Nakata, M. ; Samulski, E. T.: Thermotropic Biaxial Nematic Liquid Crystals. In: *Physical Review Letters* 92 (2004), April, No. 14. – ISSN 0031-9007, 1079-7114

[Mattheus et al. 2001]  Mattheus, Christine C. ; Dros, Anne B. ; Baas, Jacob ; Meetsma, Auke ; Boer, Jan L. d. ; Palstra, Thomas T. M.: Polymorphism in pentacene. In: *Acta Crystallographica Section C* 57 (2001), Aug, No. 8, S. 939–941

[McMillan 1971]  McMillan, W.: Simple Molecular Model for the Smectic A Phase of Liquid Crystals. In: *Physical Review A* 4 (1971), September, No. 3, S. 1238–1246. – ISSN 0556-2791

[Meyer zu Heringdorf et al. 2001]  Meyer zu Heringdorf, F. J. ; Reuter, M. C. ; Tromp, R. M.: Growth dynamics of pentacene thin films. In: *Nature* 412 (2001), Aug, No. 6846, S. 517–520

[microscopy.com-website 2012]  microscopy.com-website: *www.microscopy.com.* June 2012. – URL http://www.microscopy.com/

[Moser 2012]  Moser, Armin: *Crystal Structure Solution Based on Grazing Incidence X-ray Diffraction*, Graz University of Technology, PhD Thesis, 2012

[Necas and Klapetek 2012]    NECAS, David ; KLAPETEK, Petr: Gwyddion: an open-source software for SPM data analysis. In: *Central European Journal of Physics* 10 (2012), S. 181–188. – 10.2478/s11534-011-0096-2. – ISSN 1895-1082

[Neuhold 2012]    NEUHOLD, A: *Private communication.* June 2012

[Neuhold A. 2011]    NEUHOLD A., Moser A.:  X-ray radiation damage of organic semiconductor thin films during grazing incidence diffraction experiments. In: *Elsevier* (2011)

[Neuschitzer 2012]    NEUSCHITZER, M.: *Grazing incidence in-plane X-ray diffraction on ultra-thin organic films using standard laboratory equipment*, TU Graz, Master thesis, 2012

[Neuschitzer et al. 2012]    NEUSCHITZER, Markus ; MOSER, Armin ; NEUHOLD, Alfred ; KRAXNER, Johanna ; STADLOBER, Barbara ; OEHZELT, Martin ; SALZMANN, Ingo ; RESEL, Roland ; NOVÁK, Jiri: Grazing-incidence in-plane X-ray diffraction on ultra-thin organic films using standard laboratory equipment. In: *Journal of Applied Crystallography* 45 (2012), February, No. 2, S. 367–370. – ISSN 0021-8898

[Ocko et al. 1986]    OCKO, B. M. ; BRASLAU, A. ; PERSHAN, P. S. ; DEUTSCH, M.: Quantized layer growth at liquid-crystal surfaces. In: *Physical Review Letters* 57 (1986), July, No. 1, S. 94–97. – ISSN 0031-9007

[Parratt 1954]    PARRATT, L.: Surface Studies of Solids by Total Reflection of X-Rays. In: *Physical Review* 95 (1954), July, No. 2, S. 359–369. – ISSN 0031-899X, 1536-6065

[Pawlowska et al. 1987]    PAWLOWSKA, Z. ; KVENTSEL, G. ; SLUCKIN, T.: Theory of smectic wetting and layering. In: *Physical Review A* 36 (1987), July, No. 2, S. 992–995. – ISSN 0556-2791

[Rachinger 1948]    RACHINGER, W A.: A Correction for the alpha1, alpha2 Doublet in the Measurement of Widths of X-ray Diffraction Lines. In: *Journal of Scientific Instruments* 25 (1948), July, No. 7, S. 254–255. – ISSN 0950-7671

[Resel et al. 2003]    RESEL, R. ; TAMAS, E. ; SONDEREGGER, B. ; HOFBAUER, P. ; KECKES, J.: A heating stage up to 1173K for X-ray diffraction studies in the whole orientation space. In: *Journal of Applied Crystallography* 36 (2003), January, No. 1, S. 80–85. – ISSN 0021-8898

[Salzmann 2008]    SALZMANN, I.: *Structural and energetic properties of pentacene derivatives and heterostructures.*, Humboldt-Universität zu Berlin, Mathematisch-Naturwissenschaftliche Fakultät I, PhD Thesis, 2008

[Schmidt-Mende 2001]    SCHMIDT-MENDE, L.: Self-Organized Discotic Liquid Crystals for High-Efficiency Organic Photovoltaics. In: *Science* 293 (2001), August, No. 5532, S. 1119–1122. – ISSN 00368075, 10959203

[Sirringhaus 2000]  SIRRINGHAUS, H.:  High-Resolution Inkjet Printing of All-Polymer Transistor Circuits. In: *Science* 290 (2000), December, No. 5499, S. 2123–2126. – ISSN 00368075, 10959203

[Starkulla et al. 2009]  STARKULLA, Gundula F. ; KAPATSINA, Elisabeth ; BARO, Angelika ; GIESSELMANN, Frank ; TUSSETSCHLÄGER, Stefan ; KALLER, Martin ; LASCHAT, Sabine:  Influence of spacer chain lengths and polar terminal groups on the mesomorphic properties of tethered 5-phenylpyrimidines. In: *Beilstein Journal of Organic Chemistry* 5 (2009), November. – ISSN 1860-5397

[Takafumi Izawa 2008]  TAKAFUMI IZAWA, Kazuo T.:  Molecular Ordering of High-Performance Soluble Molecular Semiconductors and Re-evaluation of Their Field-Effect Transistor Characteristics. In: *Advanced Materials* 20 (2008), S. 3388–3392

[Tolan 1998]  TOLAN, M. ; HÖHLER, G. (Hrsg.): *X-Ray Scattering from Soft-Matter Thin Films.* Bd. 148. Springer, 1998. – ISBN 3-540-65182-9

[Van Horn and Winter 2001]  VAN HORN, Brett L. ; WINTER, H. H.:  Analysis of the Conoscopic Measurement for Uniaxial Liquid-CrystalTilt Angles. In: *Applied Optics* 40 (2001), No. 13, S. 2089. – ISSN 0003-6935, 1539-4522

[Vilalat-Clemente 2008]  VILALAT-CLEMENTE:  Principles of Atomic Force Microscopy. In: *Physics of Advanced Materials Winter School* (2008)

[Vineyard 1982]  VINEYARD, George:  Grazing-incidence diffraction and the distorted-wave approximation for the study of surfaces. In: *Physical Review B* 26 (1982), October, No. 8, S. 4146–4159. – ISSN 0163-1829

[Wedl et al. 2012]  WEDL, Bernhard ; RESEL, Roland ; LEISING, GÃ¼nther ; KUNERT, Birgit ; SALZMANN, Ingo ; OEHZELT, Martin ; KOCH, Norbert ; VOLLMER, Antje ; DUHM, Steffen ; WERZER, Oliver ; GBABODE, Gabin ; SFERRAZZA, Michele ; GEERTS, Yves: Crystallisation kinetics in thin films of dihexyl-terthiophene: the appearance of polymorphic phases. In: *RSC Advances* 2 (2012), No. 10, S. 4404. – ISSN 2046-2069

[Williamson and Hall 1953]  WILLIAMSON, G.K ; HALL, W.H: X-ray line broadening from filed aluminium and wolfram. In: *Acta Metallurgica* 1 (1953), January, No. 1, S. 22–31. – ISSN 00016160

[Yimsiri and Mackley 2006]  YIMSIRI, P. ; MACKLEY, M.R.:  Spin and dip coating of light-emitting polymer solutions: Matching experiment with modelling. In: *Chemical Engineering Science* 61 (2006), No. 11, S. 3496 – 3505. – ISSN 0009-2509